Study of background gas collisions in atomic traps

by

Janelle Van Dongen

A THESIS SUBMITTED IN PARTIAL FULFILMENT OF
THE REQUIREMENTS FOR THE DEGREE OF

Doctor of Philosophy

in

The Faculty of Graduate Studies

(Physics)

The University Of British Columbia

June, 2013

Abstract

This thesis describes an investigation and application of the loss rate constant due to background collisions for trapped atoms. The loss rate constant depends on the density of background gas and the velocity averaged collision cross section for loss due background collisions. The velocity averaged collision cross section can be calculated and its dependence on trap depth was verified using a magneto-optical trap. This verification involved measurements of the loss rate constant for the magneto-optical trap and measurement of the density of Ar background gas using a residual gas analyzer. The second part of the thesis focuses on an application of measurements of the loss rate constant due to background collisions for trapped atoms to measure pressure of the background gas. The experimental progress to date on the atom pressure sensor is provided.

Table of Contents

Appendices

List of Tables

List of Figures

Chapter 1

Introduction

1.1 Thesis overview

Loss of ultracold trapped atoms due to collisions with background (non trapped) particles can be an unwanted feature that reduces the sample size of the trapped atoms to be studied. This thesis, however, shows that the loss rate of trapped atoms due to background gas collisions can be an important and useful experimental observable. The first part of this thesis is the continued investigation (started by Fagnan et al. [1]) of the dependence of the velocity averaged loss collision cross section on trap depth. This quantity is related to the loss rate due to background collisions and is shown to have significant trap depth dependence when comparing trap depths of several mK to several K. This is important to take into account for collision cross section measurements which use loss of trapped atoms due to collisions as their measurement observable [2, 3]. The measured collision cross section based on loss from a trap will be lower than the total cross section. This is because not all collisions impart sufficient kinetic energy to the trapped atoms to cause loss from the trap.

The second, and related, topic covered in this thesis is the progress made towards using the background collision induced loss rate to determine the density of the background gas. Using trapped atoms as a density (pressure) sensor would be a novel approach for primary standards for pressure measurements in the range of 10^{-7} to 10^{-10} Torr. The potential advantages of such a standard are reproducibility from lab to lab and the possibility of externally calibrated gauges not being needed, or needed only seldom.

This chapter provides some fundamental background on the atomic traps used for the experimental work of this thesis. Chapter 2 focuses on the theory of the loss of atoms from a trap due to collisions with background gas. Chapter 3 shows experimental verification of the calculated collision cross section for loss due to background collisions with trapped atoms. ^{87}Rb was used as the trapped atom and ^{40}Ar as the background gas. Chapter 4 describes an experiment currently being built that would use the loss cross section, and measurements of loss rate in a trap whose depth is known, to

determine the density of an introduced background gas. Chapter 4 also gives background information on the commercial pressure gauges installed in our apparatus and existing pressure standards. Chapter 5 gives a description of our experimental apparatus for pressure measurement and details about the assembly of this apparatus to date are provided. Chapter 6 describes characterization performed of the two dimensional magneto-optical trap that is part of the apparatus. Chapter 8 contains conclusions as well as the future outlook for the pressure experiment.

1.2 Atomic traps

The trapping of atoms means to spatially confine them with light, electric fields, or magnetic fields so that the atoms are held in vacuum isolated from the walls of the vacuum chamber. The average temperature, T, of the trapped atoms is defined by the average kinetic energy of the atoms as $k_B T$. Typical temperatures are in the μK to mK range. Every trap has an associated trap depth, $U_{\text{trap}} = \frac{1}{2} m v_{\text{e}}^2$, where v_{e} is the escape speed needed for an atom to leave the trap. Trap depth will depend on the parameters of the confining fields such as light intensity, light frequency, and magnetic field gradient. Depending on what type of trap is being used trap depths can go up to several K. This section will discuss the principle of a 3D magneto-optical trap and a quadrupole magnetic trap. Atom number dynamics in these traps is discussed in the next section.

1.2.1 3D Magneto-Optical Trap

A magneto-optical trap (MOT) provides a means of obtaining a sample of ultracold atoms staring from a vapour or with a beam of atoms [4, 5]. A magneto-optical trap both slows (cools) and traps (confines) atoms. In a 3D MOT (see Fig.1.1) three orthogonal counter-propagating pairs of laser beams with frequency, ω, slightly tuned below an atomic resonance, perform laser cooling [5]. Laser cooling requires the light to be below atomic resonance because of the doppler shift. In the doppler shift an atom travelling with velocity $\vec{v}$ will 'see' light with wavevector $\vec{k}$ and frequency ω as having frequency $\omega' = \omega - \vec{k} \cdot \vec{v}$. When an atom with velocity $\vec{v}$ absorbs a photon with wavevector $\vec{k}$, the momentum of the atom is changed by $\hbar\vec{k}$. The atoms entering the intersection of the orthogonal laser beam pairs will be slowed down by photons with $\vec{k} \cdot \vec{v} < 0$. Photons with $\vec{k} \cdot \vec{v} > 0$ would speed up the atoms. In the second case these photons have their frequency shifted farther away from resonance so that they have a smaller probability of being

absorbed. In this manner the atoms preferentially absorb photons that slow them down. Atoms spontaneously emit the photons in random directions so that, averaging over many absorption and emission events, the momentum gain from emission is zero and the atoms are slowed down.

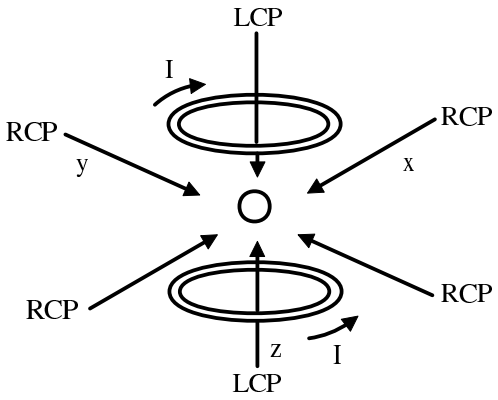

Figure 1.1: A magneto-optical trap (MOT). Three counterpropagating pairs along three perpendicular axes are used along with two magnetic coils in anti-Helmholtz configuration. The laser polarization is right circularly polarized (RCP) for beams travelling along the radial direction where the magnetic field is pointing radially outwards. The laser polarization is left circularly polarized along the axial direction (concentric with the coils) where the B field is pointing towards the center of the MOT. The trapping region is formed at the intersection of the six beams centered on the zero of the magnetic field and a cloud of atoms will be collected there.

Laser cooling alone does not trap the atoms since once they are slow enough that the doppler shifts are small then the atoms will absorb photons from any direction equally likely. The atoms will then diffuse out of the intersection of the laser beams. In other words the slowing force depends on their velocity and not their position. To provide a position dependent force for trapping, a magnetic field is added produced by two concentric coils in an anti-Helmholtz configuration. Anti-helmholtz configuration describes when the coils are parallel and spaced by their own radii. The current through the coils is equal and runs in opposite directions. The direction concentric with the coils' centers is called the axial direction. For the direction of current shown in Fig. 1.2 the magnetic field along a line parallel to, and in between, the two coils starts at zero magnitude at the origin between the two coils and increases linearly outwards pointing away from the center along the radial

direction. Along the axial direction in Fig. 1.2 the magnetic field points toward the center of the MOT and the axial magnetic field gradient, $\frac{d|\vec{B}|}{dz}$ is double the gradient along the radial directions [6].

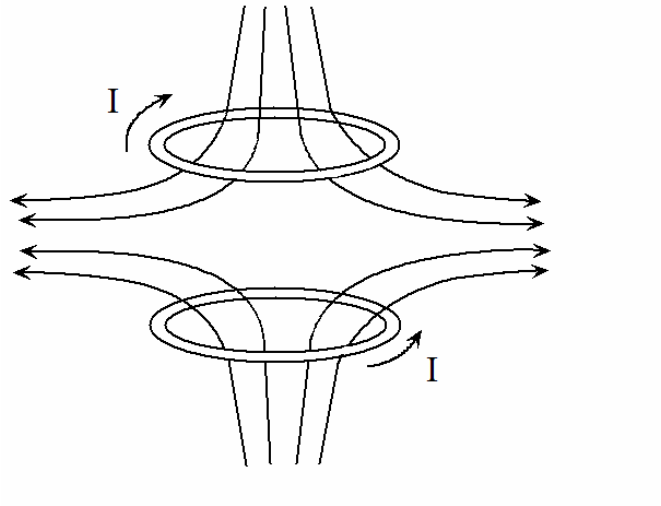

Figure 1.2: The magnetic field lines generated by passing current I in opposite directions through two coils spaced by their radii (known as anti-Helmholtz configuration). The magnetic field is zero at the center between the coils and increases linearly in magnitude pointing away from the center in the radial direction and towards the center in the axial direction.

In a MOT the magnetic field in combination with the appropriate polarization choice of the laser beams adds confinement of the atoms. This is achieved by causing the atoms to preferentially absorb light that pushes them to the magnetic field zero. The trapping region is at the intersection of the laser beams centered on the zero of the magnetic field. Figure 1.3 explains the principle of a MOT. The laser light with energy hf_L is detuned below the $F = 0$ to $F' = 1$ transition, taken as an example. In the presence of the weak magnetic field of magnitude B generated in a MOT, the hyperfine m_F sublevels change according to $\Delta E = m_F g_F \mu_B B$, where g_F is the Landé g-factor and μ_B is the Bohr magneton [7, 8]. For $g_{F'} > 0$ the $m_{F'} = -1$ transition decreases in energy away from the magnetic field zero position.

Right circularly polarized (RCP) light propagating in the same direction as the B-field will drive $\Delta m_F = m_{F'} - m_F = +1$, called σ^+ transitions.

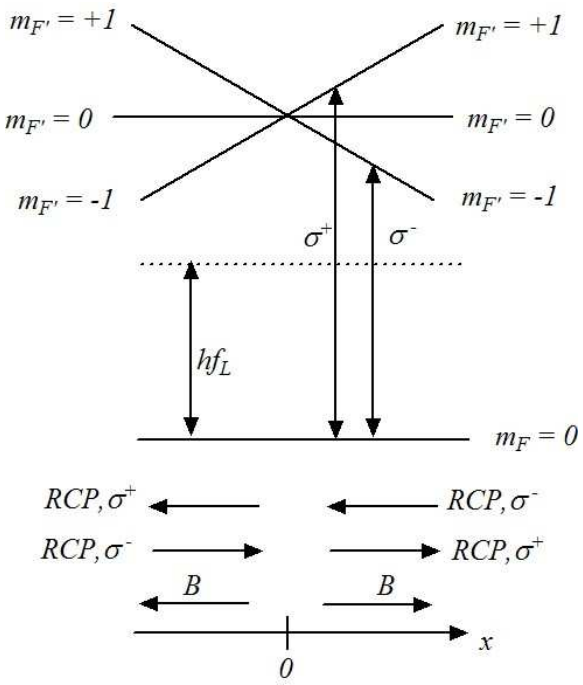

Figure 1.3: Hyperfine sublevels undergoing a continuous energy shift with changing magnetic field in a magneto-optical trap. The vertical axis, not labelled, is energy. The vertical axis, not labelled, is energy. Atoms that move to the right or left of the magnetic field zero have a greater probability of absorbing light that pushes the atoms back towards the magnetic field zero.

Right circularly polarized (RCP) light propagating in the opposite direction to the B-field will drive $\Delta m_F = m_{F'} - m_F = -1$, called σ^- transitions. In Fig. 1.3 the $m_F = 0$ to $m_{F'} = -1$ transition is closest to the laser frequency so the atoms would preferentially absorb the σ^- light. If σ^- light is travelling toward the center on either side of the magnetic field zero then an atom which goes away from the center will be pushed back towards the center. Along the z axis, concentric with the coils, the B field is pointing inwards (as shown in Fig. 1.2). For this case left circularly polarized light must be used along the z axis. Left circularly polarized light travelling in the same direction as the magnetic field will drive $\Delta m_F = m_{F'} - m_F = -1$ transitions and $\Delta m_F = m_{F'} - m_F = +1$ transitions when anti-aligned with the magnetic field.

For the work in this thesis either ^{85}Rb or ^{87}Rb is trapped. The laser light used for the trapping in the MOT is called the pump light. A secondary frequency of light called the repump light is also needed to prevent atoms from pooling in a hyperfine state that cannot be excited by the pump laser. The $5^2S_{1/2}$ to $5^2P_{3/2}$ transition is used for the pump and repump light (see Figs. 1.5 and 1.4). The pump is chosen to be the $F = 2$ to $F' = 3$ transition for ^{87}Rb and $F = 3$ to $F' = 4$ transition for ^{85}Rb. The repump is chosen to be the $F = 1$ to $F' = 2$ transition for ^{87}Rb and $F = 2$ to $F' = 3$ transition for ^{85}Rb. Taking ^{87}Rb as an example, $F = 2$ to $F' = 3$ light can also drive off resonant transitions to the $F' = 2$ or $F' = 1$ hyperfine level. These levels can decay to the $F = 1$ hyperfine state of the $5^2S_{1/2}$ ground state. The atoms will not absorb the pump light once in that state and laser cooling and trapping will not be accomplished. In order to get the atoms out of this 'dark' state, repump light driving the $F = 1$ to $F' = 2$ transition is needed so that there is some probability of atoms decaying back to the $F = 2$ ground state.

1.2.2 Magnetic traps

After cooling and collecting atoms in a MOT they can be transferred to a magnetic trap for further study or cooling. A magnetic trap can be formed using the same coils as used for the MOT. The laser light is shut off and a higher current is run through the coils to produce a higher magnetic field gradient. As mentioned above, the energy of atoms for weak magnetic fields changes according to $\Delta E = g_F m_F \mu_B B$. Atoms in states that have Zeeman shifts resulting in higher energy as magnetic field increases (states with $g_F m_F > 0$) will tend to stay near the zero of the field and are called 'low field seekers'. Atoms that are 'high field seekers' will leave the trap. The initial cooling stage in a MOT is necessary because magnetic traps provide much weaker confinement forces than a MOT and do not provide cooling. The trap depth of the magnetic trap for an atom in state m_F will be $\Delta E = g_F m_F \mu_B (B_{\max} - B_{\min})$ where $B_{\max}(B_{\min})$ is the maximum (minimum) magnetic field a trapped atom can access inside the cell. For quadrupole magnetic fields created by the coils in anti-Helmholtz configuration, $B_{\min} = 0$ and $B_{\max}$ is limited either by the size of the vacuum cell or the roll off of the magnetic field. In our case the size of the cell walls limit the maximum magnetic field the trapped atoms can experience. The cell walls are at room temperature and so when a trapped atom hits the cell wall it gains a large amount of kinetic energy and will not be trapped anymore. The trap depth along the radial direction, ρ, is

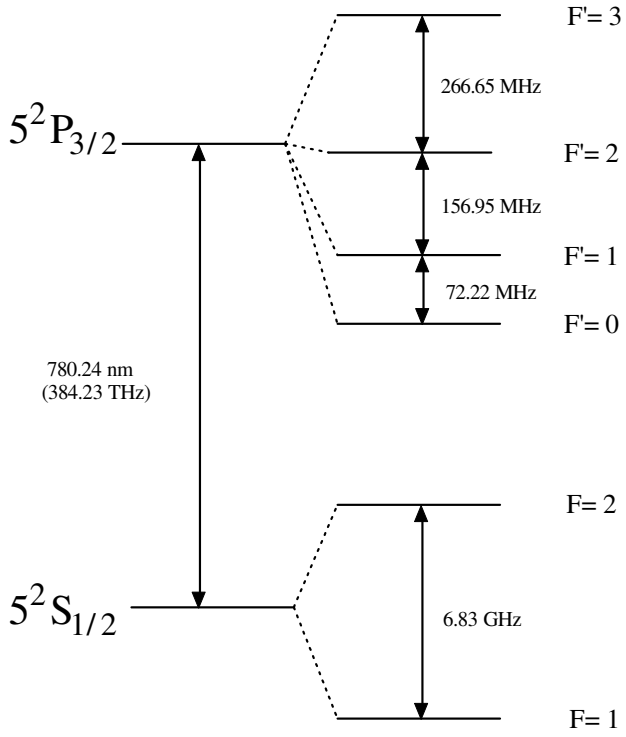

Figure 1.4: The energy levels for the D_2 transition for ^{87}Rb. The $F = 2$ to $F' = 3$ transition is used for the pump light of the magneto-optical trap. The $F = 1$ to $F' = 2$ transition is used for the repump light.

$g_F m_F \mu_B \frac{dB}{d\rho} l$ where l is the horizontal distance from the field zero to the cell walls. The trap depth against gravity along the downward vertical direction is $g_F m_F \mu_B \frac{dB}{dz} z_w - mgz_{\rm w}$ where z_w is the distance from the zero of magnetic field to the cell walls in the vertical direction. For a quadrupole magnetic field the gradient along the axial direction is double that along the radial direction, i.e. $\frac{dB}{dz} = 2\frac{dB}{d\rho}$. An effective trap depth averaged over both the radial and axial directions is assumed unless otherwise noted. Magnetic traps have typical trap depths on the order of a few mK.

A useful way of setting the trap depth of a magnetic trap more precisely so that the trap depth is the same in all directions is with a 'Radio Frequency (RF) knife' [9]. The concept is explained in Fig. 1.6. A RF frequency is introduced while the magnetic trap is on. At a certain magnetic field value the splitting between levels of a trappable state (e.g. $m_F = +1$ in Fig. 1.6) and an untrappable state (e.g. $m_F = 0$ in Fig. 1.6) will correspond to the

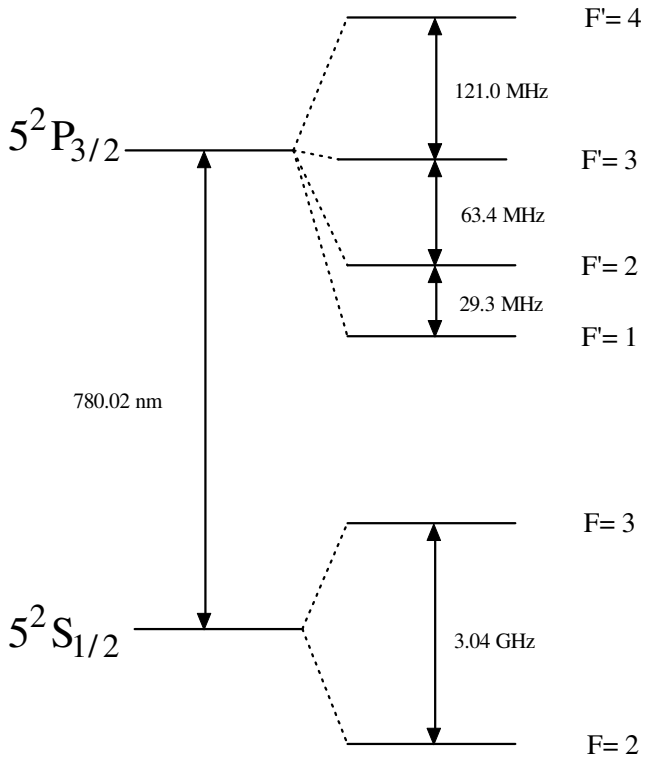

Figure 1.5: The energy levels for the D_2 transition for ^{85}Rb. The $F = 3$ to $F' = 4$ transition is used for the pump light of the magneto-optical trap. The $F = 2$ to $F' = 3$ transition is used for the repump light.

RF frequency. Atoms that are in the trappable state can then transition to an untrappable state when they reach the energy at which the transition occurs. This sets an isotropic trap depth for the magnetic trap. The spatial dimensions of the trap in different directions will be different because the magnetic field gradient is different along the axial and radial directions.

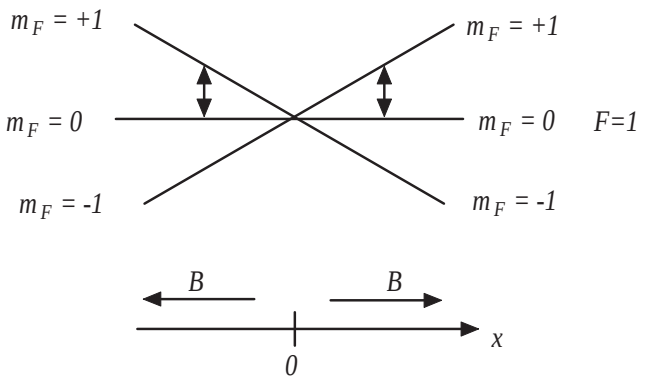

Figure 1.6: Hyperfine sublevels undergoing a continuous energy shift with changing magnetic field in a magnetic trap. The vertical axis, not labelled, is energy. The trappable state shown here is the $m_F = +1$ state (assuming $g_F > 0$ here). A RF frequency can cause transitions to the untrappable $m_F = 0$ state and atoms will be lost from the trap. In this way the trap depth of the magnetic trap is set isotropically and precisely.

1.3 Trap dynamics

1.3.1 Magneto-optical trap dynamics

In a magneto-optical trap the number of atoms in the trap as a function of time, $N(t)$, can be given as [10]

$$\frac{dN}{dt} = R - \Gamma N - \beta \int n^2(\vec{r}, t)\, d^3\vec{r} \tag{1.1}$$

with $t = 0$ being when both the magnetic field and light have been turned on [11]. R is the rate of capture which is the number of atoms per second entering the intersection of the six beams and being slowed down and confined. ΓN is the rate of loss due to collisions of background gas atoms with the trapped atoms. Γ has units of s^{-1} and is called the loss rate constant due to background collisions. $\tau = 1/\Gamma$ is called the lifetime of the trap. Γ has typical values of 0.1 to 2 s^{-1} for the experimental setup described in chapter 3 . The last term of Eq. 1.1 describes losses due to the collision of two trapped atoms, where $n(\vec{r}, t)$ is the density of the trapped atoms at position $\vec{r}$ and time t. The origin is placed at the center of the trap where the atoms collect in a roughly spherical ball. β is the loss rate constant due to

two-body 'intra-trap' collisions. It is on the order of 10^{-11} to $10^{-13}\text{cm}^3\text{s}^{-1}$ and is mediated by radiative escape, fine-structure changing collisions and hyperfine changing collisions [11, 12].

If $\beta \int n^2(\vec{r},t)\, d^3\vec{r}$ is negligible compared to the background loss rate term then the solution to Eq. 1.1 is

$$N(t) = \frac{R}{\Gamma}\left(1 - e^{-\Gamma t}\right). \tag{1.2}$$

The steady state solution in this case is $N(t=\infty) = \frac{N}{\Gamma}$. Typically the steady state number in a MOT is around 10^7 to 10^{10} atoms. An example plot of N(t), given by Eq. 1.2, is shown in Fig. 1.7.

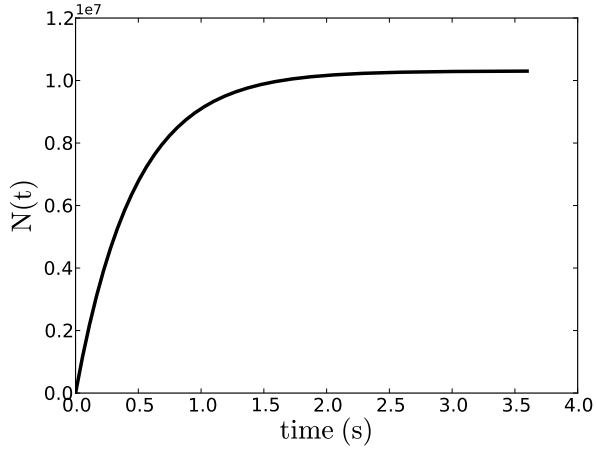

Figure 1.7: A plot of atom number, $N(t)$, versus time, t, from initial MOT loading. The plot uses the model given in Eq. 1.2 with $R = 2.2\times10^7$ atoms/s and $\Gamma = 2.1\ \text{s}^{-1}$. The steady state voltage atom number is $N(\infty) = \frac{R}{\Gamma} = 1.05 \times 10^7$.

Another case to consider is when $\beta \int n^2(\vec{r},t)\, d^3\vec{r}$ is not negligible and the atom number density is less than approximately 10^{10} atoms per cm^3 [13]. In this case the atom cloud in the MOT has a gaussian density profile of $n(\vec{r},t) = n_0(t)e^{-\left(\frac{|\vec{r}|}{w}\right)^2}$, where $n_0(t)$ is the peak density at $|\vec{r}| = 0$, and w is the width of the gaussian distribution which is taken to be time-independent. For this density profile the integral in Eq. 1.1 is $\int n^2(\vec{r},t)\, d^3\vec{r} = [n_0(t)]^2 \left(w\sqrt{\frac{\pi}{2}}\right)^3$. The total number in the trap taken by integrating the density is $N(t) =$

$n_0(t)\left(w\sqrt{\pi}\right)^3$. Using these results Eq. 1.1 simplifies to

$$\frac{dN}{dt} = R - \Gamma N - aN^2 \tag{1.3}$$

where $a = \frac{\beta}{(w\sqrt{2\pi})^3}$. Maple gives the solution to this differential equation as

$$N(t) = \frac{-\Gamma + \tanh\left(\frac{1}{2}t\sqrt{4Ra+\Gamma^2} + \tanh^{-1}\left(\frac{\Gamma}{\sqrt{4Ra+\Gamma^2}}\right)\right)\sqrt{4Ra+\Gamma^2}}{2a} \tag{1.4}$$

Another way of expressing the solution to Eq.1.3 (derived by Dr. James Booth) is

$$N(t) = \frac{\gamma - \Gamma}{2a} \cdot \frac{1 - e^{-\gamma t}}{1 - \left(\frac{\Gamma-\gamma}{\Gamma+\gamma}\right)e^{-\gamma t}} \tag{1.5}$$

where $\gamma = \sqrt{\Gamma^2 + \frac{4\beta R}{(w\sqrt{2\pi})^3}}$. Though the second form of the solution is a bit more compact, the first is easier to extract the values for Γ, R and a directly from fit results. Another form of the solution for the gaussian density case similar to Eq. 1.5 is given in [14] .

When the density of trapped atoms in a MOT is large the probability increases of the trapped atoms absorbing the photons emitted by other atoms in the MOT (called multiple scattering [13]). This results in an outward force on the trapped atoms so that the density profile becomes constant (a top-hat distribution) rather than a gaussian distribution and the volume of the atom cloud grows with atom number. When the density is taken to be a constant, n, Eq. 1.1 becomes

$$\frac{dN}{dt} = R - \Gamma N - \beta n N. \tag{1.6}$$

The solution to this equation can be solved as

$$N(t) = \frac{R}{\Gamma_{\text{eff}}}\left(1 - e^{-\Gamma_{\text{eff}}t}\right) \tag{1.7}$$

where

$$\Gamma_{\text{eff}} = \Gamma + \beta n. \tag{1.8}$$

1.3.2 Magnetic trap dynamics

Magnetic traps are loaded once with an initial number of atoms that then decays due to losses such as background collision induced loss. The loading

rate, R, in Eq. 1.1 is zero for a magnetic trap. If we assume the intra-trap loss term is negligible, then the solution to Eq. 1.1 becomes

$$N(t) = N(0)e^{-\Gamma t} \tag{1.9}$$

where $N(0)$ is the initial number in the magnetic trap.

This thesis will focus on the loss rate constant due to background collisions, Γ. Its dependence on trap depth and density of background gas are the two main topics presented. A novel primary pressure standard based on measurements of Γ is proposed and current experimental progress to that end is described. To start, the next chapter explains the loss rate constant Γ in terms of its dependence on density of background gas and its dependence on the loss collisional cross section.

Chapter 2

Background gas collision induced loss

The situation of interest is that of a background gas atom colliding with a trapped atom elastically. The background gas particle could be residual background gas from the outgassing of vacuum parts, atoms that are of the trapped species that are not trapped, or a purposefully introduced background species such as Ar, N_2 or He.

The loss rate constant due to background gas collisions, Γ, introduced in Eq. 1.1 in the last chapter, can be written as

$$\Gamma = \sum_i n_i \langle \sigma_{\text{loss}} v_i \rangle_{X,i} \tag{2.1}$$

where n_i denotes the density of a particular background species i. The term σ_{loss} is the collisional cross section for loss between a trapped atom of type X and a background species particle of type i [15, 16]. As we will see later in this chapter σ_{loss} is dependent on the relative kinetic energy of the colliding particles. For our case our trapped atoms are assumed to be stationary, in the lab frame, with respect to the background gas atoms. In this case, the relative speed of a trapped atom and a background gas particle is the speed of the background gas particle. The brackets indicate a Maxwell-Boltzmann average over all possible speeds, $v_i = 0$ to $v_i = \infty$, of background species i. Because we are describing loss from a trap, σ_{loss} also depends on the trap depth of the trap. If the trap depth is anisotropic then an average trap depth is taken. The calculation of the velocity averaged collisional loss cross section, $\langle \sigma_{\text{loss}} v_i \rangle_{X,i}$, is described in detail in [1, 17]. This chapter serves as an overview of those works.

2.1 A brief review of necessary scattering theory

To properly describe the meaning and calculation of $\langle \sigma_{\text{loss}} v_i \rangle_{X,i}$, a basic review of quantum scattering theory is needed. The following is based pri-

marily on the honours thesis of David Fagnan [17] who performed the calculation of $\langle \sigma_{\text{loss}} v_i \rangle_{X,i}$ for our group. The calculation was for ^{87}Rb in its ground state as the trapped species and ^{40}Ar in its ground state as the background species. The following quantum textbooks and scattering theory notes are also helpful [18–22].

The hamiltonian describing two interacting particles of mass m_1 and m_2 is

$$H = \frac{|\vec{p}_1|^2}{2m_1} + \frac{|\vec{p}_2|^2}{2m_2} + V(|\vec{r}_1 - \vec{r}_2|) \tag{2.2}$$

where $\vec{r}_1$, $\vec{p}_1 = m_1\vec{v}_1$, $\vec{r}_2$, $\vec{p}_2 = m_2\vec{v}_2$ are the positions and momenta operators of particle 1 and 2 respectively.

The coordinate of the center of mass is

$$\vec{R} = \frac{m_1\vec{r}_1}{M} + \frac{m_2\vec{r}_2}{M} \tag{2.3}$$

and the velocity of the center of mass is

$$\vec{v}_R = \frac{m_1\vec{v}_1}{M} + \frac{m_2\vec{v}_2}{M} \tag{2.4}$$

where $M = m_1 + m_2$ so that $M\vec{v}_R = \vec{p}_1 + \vec{p}_2 = \vec{P}$ where $\vec{P}$ is the total momentum. By conservation of total momentum $\vec{v}_R$ is a constant. In the center of mass frame $\vec{v}_R = 0$ so that the total momentum is zero and the particles have equal and opposite momenta. It is also useful to use the relative coordinate $\vec{r} = \vec{r}_1 - \vec{r}_2$ and the relative velocity $\vec{v}_r = \vec{v}_1 - \vec{v}_2$. The relative velocity vector is the same in the lab and in the center of mass frame. Under conservation of momentum and total kinetic energy the magnitude of the relative velocity, $|\vec{v}_r| = |\vec{v}_1 - \vec{v}_2|$, is a constant before and after collision. This is most easily seen in the center of mass frame where the speeds of particles 1 and 2 are unchanged by an elastic collision. The direction of $\vec{v}_r$ does change before and after collision. Using the center of mass coordinate and the relative coordinate the hamiltonian given in Eq. 2.2 can be expressed equivalently as

$$H = -\frac{\hbar^2}{2M}\nabla_R^2 - \frac{\hbar^2}{2\mu}\nabla_r^2 + V(r) \tag{2.5}$$

where $\mu = \frac{m_1 m_2}{m_1 + m_2}$ is the reduced mass and ∇_R^2 and ∇_r^2 are the laplacians with respect to the center of mass and relative coordinates, respectively. In this form the hamiltonian is composed of a sum of a center of mass part and a relative part.

A time independent approach will be used because a time dependent wavepacket treatment given in [20] gives the same result for the differential

collision cross section that is derived later in this chapter. A solution to the time independent Schrödinger equation, $H\psi = E\psi$, is $\psi = \psi_R\psi_r$ where ψ_R satisfies the equation

$$-\frac{\hbar^2}{2M}\nabla_R^2\psi_R = E_R\psi_R \tag{2.6}$$

and ψ_r satisfies

$$\left[-\frac{\hbar^2}{2\mu}\nabla_r^2 + V(r)\right]\psi_r = E_r\psi_r \tag{2.7}$$

where $E = E_R + E_r$. The equation involving the center of mass coordinate is just that of a free particle of mass M where $E_R = \frac{1}{2}M\dot{R}^2$ so that in the center of mass frame with $\dot{R} = 0$ we have $E_R = 0$ and $E = E_r$. It also suffices to have $\dot{R} = 0$ be a constant so that E_R is a constant. The second equation has the form of a single particle of reduced mass μ that is subject to a spherically symmetric potential $V(r)$. In the center of mass frame

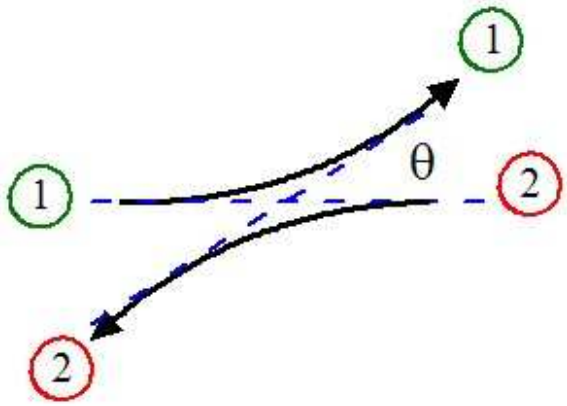

Figure 2.1: In the center of mass frame particles 1 and 2 travel with opposite and equal momenta. After collision they travel along a line that makes an angle θ with respect to the original line of incidence.

a collision of two particles is pictorally shown in Fig. 2.1 where the two particles approach each other with equal and opposite momenta, interact and then recede from each other with equal and opposite momenta. The path of the receding particles makes an angle θ in the center of mass frame with respect to the original line of incidence. Note the angle θ is the angle between the relative velocity vectors before and after collision and is the same in both the lab and center of mass frame.

The assumption is now made that the change in speed (in the lab frame) of the trapped atom due to collision is much greater than the initial speed of the trapped atom before collision. With this assumption the kinetic energy imparted to the trapped atom with mass m_1 in the lab frame is [17]

$$\Delta E \approx \frac{\mu^2}{m_1}|\vec{v}_r|^2(1-\cos(\theta)). \tag{2.8}$$

If ΔE is greater than the trap depth, U_0, then the trapped atom involved in the collision will be lost from the trap. According to Eq. 2.8 this corresponds to collisional angles, θ, greater than

$$\theta_{\min} = \cos^{-1}\left(1 - \frac{U_0 m_1}{\mu^2|\vec{v}_r|^2}\right) \tag{2.9}$$

As discussed above in the center of mass frame the collision between the two particles can be equivalently thought as a single particle of reduced mass μ approaching a radially symmetric potential which goes to zero as $r \to \infty$. The solution ψ_r is expected to have the form

$$\psi_r \sim e^{i\vec{k}\cdot\vec{r}} + f(k,\theta,\phi)\frac{e^{ikr}}{r} \tag{2.10}$$

to describe the particle when it is far from the potential region after collision [22]. The first term describes that the particle is initially a free particle with a plane wave behaviour and there is some probability of it not scattering when passing through the potential region. The wavevector $\vec{k}$ describes the energy in the relative motion (i.e. the energy of the incident reduced mass particle) given by $E_r = \frac{\hbar^2 k^2}{2\mu}$ where $k = \mu|\vec{v}_r|/\hbar$. Note this is the energy for the incident particle approximated as a free particle when it is far away from the potential region. We are interested in the case of after an elastic collision when the particle is again far from the potential region so that the energy E_r is the same as the incident energy. The second term in Eq. 2.10 describes scattering by a spherical wave, where $f(k,\theta,\phi)$ indicates that there is a different probability of scattering in different directions, (θ,ϕ).

Classically one considers an incident beam of finite width consisting of many incoming particles centered on the target region. A detector is placed that detects any scattered particles that travel to some solid angle, defined by the area of the detector, in the direction θ,ϕ. The differential cross-section, $\frac{d\sigma}{d\Omega}$, is defined as

$$\frac{d\sigma}{d\Omega} = \frac{\text{flux scattered into the solid angle element } d\Omega \text{ per unit solid angle}}{\text{flux in the incident beam per unit area}} \tag{2.11}$$

where the differential solid angle element is $d\Omega = \sin\theta d\theta d\phi$. Classically, flux here has units of number per second. The number per second passing through a differential area $d\vec{S}$ is $\vec{J}\cdot d\vec{S}$ where $\vec{J}$ is the current density, which describes the number of particles passing through a unit area per unit time. In the absence of sources or sinks (no particles are created or destroyed) $\vec{J}$ obeys the continuity equation

$$\frac{d\rho}{dt} + \vec{\nabla}\cdot\vec{J} = 0 \tag{2.12}$$

where ρ is the density of particles (the number of particles per unit volume).

To determine a quantum mechanical expression for the differential cross section, consider again our case of a single particle subject to some localized potential. $|\psi_r|^2$ is a probability density (the probability of finding the particle at a particular place per unit volume) and can replace the classical density ρ in Eq. 2.12. In this case since $|\psi_r|^2$ has units of probability per unit volume, $\vec{J}$ will have units of probability per unit time per unit area. With this interpretation it can be shown [22] that $\vec{J}$ for a particle of mass μ has the form

$$\begin{aligned} \vec{J} &= \frac{\hbar}{2\mu i}(\psi^*\nabla\psi - \psi\nabla\psi^*) \\ &= \frac{\hbar}{\mu}\mathrm{Im}(\psi^*\nabla\psi) \end{aligned} \tag{2.13}$$

The denominator of Eq. 2.11, using a plane wave $\psi_r = e^{ikz}$ in Eq. 2.13 and $d\vec{S} = dxdy\hat{z}$, is

$$\frac{\vec{J}\cdot d\vec{S}}{dS} = \frac{\hbar k}{\mu}. \tag{2.14}$$

The numerator of Eq. 2.11 can be found using $\psi_r = f(k,\theta,\phi)\frac{e^{ikr}}{r}$ in Eq. 2.13 and $d\vec{S} = r^2\sin\theta d\theta d\phi\hat{r} = r^2 d\Omega\hat{r}$ as

$$\frac{\vec{J}\cdot d\vec{S}}{d\Omega} = \frac{\hbar k|f(k,\theta,\phi)|^2}{\mu}. \tag{2.15}$$

Taking the ratio of Eq. 2.15 and Eq. 2.14 the differential cross section is

$$\frac{d\sigma}{d\Omega} = |f(k,\theta,\phi)|^2. \tag{2.16}$$

Hereafter cylindrical symmetry is assumed so f is not a function of ϕ.

The total cross section is given by integrating the differential cross section over all solid angles

$$\sigma = 2\pi \int_0^{\pi} |f(k,\theta)|^2 \, \sin\theta \, d\theta. \tag{2.17}$$

The loss collisional cross section given in Eq. 2.1 for the loss rate constant, Γ, is similar to the total cross section but only accounts for collisions that induce loss from the trap. This means that instead of starting at zero for the scattering angle θ we start from the minimum scattering angle that results in loss. This was expressed as $\theta_{\min}$ in Eq. 2.9 and gives a cross section for loss as

$$\sigma_{\text{loss}} = 2\pi \int_{\theta_{\min}}^{\pi} |f(k,\theta)|^2 \, \sin\theta \, d\theta. \tag{2.18}$$

The cross section for heating collisions that do not result in trap loss is given as

$$\sigma_{\text{heat}} = 2\pi \int_0^{\theta_{\min}} |f(k,\theta)|^2 \, \sin\theta \, d\theta. \tag{2.19}$$

2.2 Calculation of $\langle \sigma_{\text{loss}} v_i \rangle_{X,i}$

The section explains how σ_{loss} is calculated and the beginning treatment follows these references [1, 17, 22]. Eq. 2.7 for $\psi_r(r,\theta,\phi)$ written in terms of spherical coordinates and the angular momentum operator squared, $\hat{L}^2$, is [18]

$$\frac{\hbar}{2\mu}\left[-\frac{1}{r^2}\frac{\partial}{\partial r}\left(r^2\frac{\partial \psi_r}{\partial r}\right) + \frac{\hat{L^2}}{r^2}\psi_r\right] + V(r)\psi_r = E\psi_r. \tag{2.20}$$

The solution $\psi_r(r,\theta,\phi) = R_l(r)Y_{l,m}(\theta,\phi)$ is comprised of a radial and angular part. The angular part, the spherical harmonics, $Y_{l,m}(\theta,\phi)$, are eigenfunctions of $\hat{L}^2$ with $\hat{L}^2 Y_{l,m} = l(l+1)Y_{l,m}$.

Substituting this solution for $\psi_r(r,\theta,\phi)$ into Eq. 2.20 gives [18]

$$\frac{1}{r^2}\frac{d}{dr}\left(r^2\frac{dR_l}{dr}\right) - \frac{l(l+1)}{r^2}R_l + \frac{2\mu}{\hbar^2}\left[E - V(r)\right]R_l = 0 \tag{2.21}$$

In our case we assume cylindrical symmetry so that ψ_r is a function of r and θ only. For this case the spherical harmonics are proportional to the Legendre polynomials $Y_{l,0} \propto P_l(\cos\theta)$. Taking linear combinations for the most general solution of $\psi_r(r,\theta)$ gives

$$\psi_r(r,\theta) = \sum_{l=0}^{\infty}(2l+1)i^l A_l R_l(r) P_l(\cos\theta) \tag{2.22}$$

where $A_l = 1$ for a free particle and otherwise it is a constant to be determined.

Eq. 2.21 for the radial part R_l can be expressed in terms of $\psi_l(r) = krR_l(r)$ as

$$\left[\frac{d^2}{dr^2} + W(r)\right]\psi_l(r) = 0 \tag{2.23}$$

with

$$W(r) = k^2 - \frac{2\mu}{\hbar^2}V(r) - \frac{l(l+1)}{r^2}. \tag{2.24}$$

Note $\psi_l(r)$ is not to be confused with $\psi_r(r,\theta)$.

When $V(r) = 0$ the solution to Eq. 2.21 is [22]

$$R_l(r) = \cos(\delta_l)j_l(kr) - \sin(\delta_l)n_l(kr) \tag{2.25}$$

where $j_l(kr)$ and $n_l(kr)$ are the spherical Bessel and Neumann functions, respectively, and δ_l is a real number called the partial wave dependent phase shift. This phase shift is key for interpreting elastic scattering. For a free particle $R_l(r) = j_l(kr)$ because the potential is zero at $r = 0$ and the Neumann part of the function is discounted because it blows up as r approaches zero. For our case we are interested in the solution for $V(r) \to 0$ for $r \to \infty$. At $r = 0$ we have $V(r) \neq 0$ and so the Neumann term is retained. The asymptotic form of $j_l(kr)$ as $r \to \infty$ is

$$j_l(kr) \to \frac{\sin(kr - \frac{1}{2}\pi l)}{kr}. \tag{2.26}$$

The asymptotic form of $n_l(kr)$ as $r \to \infty$ is

$$n_l(kr) \to \frac{-\cos(kr - \frac{1}{2}\pi l)}{kr} \tag{2.27}$$

so that the asymptotic form of $R_l(r)$ is

$$R_l(r) \to \frac{\sin(kr - \frac{1}{2}\pi l + \delta_l)}{kr}. \tag{2.28}$$

The asymptotic solution for ψ_r given in Eq. 2.10 can be matched with Eq. 2.22 with the form of $R_l(r)$ given in Eq. 2.28. The free particle part of the solution $e^{i\vec{k}\cdot\vec{r}}$ can be replaced by Eq. 2.22, with $A_l = 1$ and with the form of $R_l(r)$ given in Eq. 2.26. This gives

$$\sum_{l=0}^{\infty}(2l+1)i^l P_l(\cos\theta)A_l\frac{\sin(kr - \frac{1}{2}\pi l + \delta_l)}{kr} \tag{2.29}$$

$$= \sum_{l=0}^{\infty}(2l+1)i^l P_l(\cos\theta)\frac{\sin(kr - \frac{1}{2}\pi l)}{kr} + \frac{f(k,\theta,\phi)e^{ikr}}{r}$$

The sin and cos functions can be expressed as complex exponentials and coefficients of e^{-ikr} and e^{ikr} can be matched on either side of the expression giving [22]

$$A_l = e^{i\delta_l} \tag{2.30}$$

and

$$f(k,\theta) = \frac{1}{k}\sum_{l=0}^{\infty}(2l+1)\sin(\delta_l)e^{i\delta_l}P_l(\cos\theta). \tag{2.31}$$

To determine $f(k,\theta)$ complex T-matrix elements need to be determined

$$T_l(k) \equiv e^{i\delta_l}\sin\delta_l. \tag{2.32}$$

The $T_l(k)$ values can be found from the complex S-matrix elements

$$S_l(k) \equiv e^{2i\delta_l} = 1 + 2iT_l(k). \tag{2.33}$$

Finally $S_l(k)$ can be found from the real K-matrix elements

$$K_l(k) \equiv \tan\delta_l(k). \tag{2.34}$$

The S and K matrix elements are related by

$$S_l(k) = \frac{1+iK_l(k)}{1-iK_l(k)}. \tag{2.35}$$

To find $K_l(k)$ Eq. 2.23 is expressed interms of the logarithmic derivative

$$y_l(r) = \frac{\psi_l'(r)}{\psi_l(r)} \tag{2.36}$$

to give

$$y'(r) + y^2(r) + W(r) = 0. \tag{2.37}$$

Here the prime in Eq. 2.36 and Eq. 2.37 means differentiation with respect to r. The values $y_l(r)$ are solved for in the limit of large r using numerical methods described in [17, 23]. The asymptotic form of the solution for $\psi_l(r)$ given in Eq. 2.25 can be expressed in terms of $K_l(k)$ as

$$\psi_l(r) = B_l\left[\hat{j}_k(kr) - K_l(k)\hat{n}_l(kr)\right] \tag{2.38}$$

where $B_l = cos(\delta_l)$ and

$$\hat{j}_l(kr) = krj_l(kr) \tag{2.39}$$

$$\hat{n}_l(kr) = krn_l(kr). \tag{2.40}$$

$$\tag{2.41}$$

Replacing Eq. 2.38 in the definition of $y_l(r)$ given in Eq. 2.36 and solving for $K_l(k)$ gives

$$K_l(k) = \frac{y_l(r)\hat{j}_l(kr) - \frac{d}{dr}(\hat{j}_l(kr))}{y_l(r)\hat{n}_l(kr) - \frac{d}{dr}(\hat{n}_l(kr))} \tag{2.42}$$

where the prime means differentiation with respect to r. Once $K_l(k)$ is determined then $S_l(k)$ can be found from Eq. 2.35. $T_l(k)$ can then be found from Eq. 2.33. The scattering amplitude, $f(k,\theta)$, for a particular k and θ can be found by substituting $T_l(k)$ into Eq. 2.31 and summing over l until convergence criteria are met. Next $f(k,\theta)$ is substituted into Eq. 2.18 to obtain the loss cross section, σ_{loss}, and the integral is performed numerically over θ . This gives σ_{loss} for one particular $k = \mu v_r/\hbar \approx \mu v_i/\hbar$ value where v_i is the background particle speed in the lab frame and we used the assumption that the trapped atom is stationary in the lab frame. To determine $\langle \sigma_{\text{loss}} v_i \rangle_{X,i}$ for the trapped species X and background species i an average over all speeds v_i using a Maxwell-Boltzmann distribution is performed

$$\langle \sigma v_i \rangle_{X,i} = 4\pi \int_0^\infty (\frac{m_i}{2\pi k_B T})^{3/2} v_i^3 e^{-\frac{m_i v_i^2}{2k_B T}} \sigma(\frac{\mu |v_i|}{\hbar}) dv_i \tag{2.43}$$

which requires another numerical integration over v_i.

It is important to note that $\langle \sigma_{\text{loss}} v_i \rangle_{X,i}$ is a function of trap depth through the limits of integration in Eq. 2.18. Intuitively one would predict that $\langle \sigma_{\text{loss}} v_i \rangle_{X,i}$ will decrease as trap depth increases. This is because the larger the kinetic energy needed for a trapped atom to escape the trap the less probable it is that a collision with a background gas particle will cause loss. Figure 2.2 shows the variation of $\langle \sigma_{\text{loss}} v_{\text{Ar}} \rangle_{^{87}\text{Rb},^{40}\text{Ar}}$ with trap depth. For this calculation both species are taken to be in the ground state and the potential used is $V(r) = \frac{C_{12}}{r^{12}} - \frac{C_6}{r^6}$. The coefficients are taken to be $C_6 = 280 E_{\text{H}} a_{\text{B}}^6$ and $C_{12} = 8.6 \times 10^7 E_{\text{H}} a_{\text{B}}^{12}$, where $E_{\text{B}} = 4.35974 \times 10^{-18}$ J and a_B is the Bohr radius [1]. In the limit of zero trap depth the loss cross section becomes the total cross section. The points superimposed on the curve are experimental data which will be discussed in the next chapter.

For large trap depths classical calculation predicts a $U^{-1/6}$ dependence of the loss cross section on trap depth for a long range potential interaction of $V(r) = -\frac{C_6}{r^6}$ [15, 25, 26]. As trap depth decreases scattering of smaller angles θ becomes included in the loss cross section calculation. For small trap depths, where small angle scattering can induce loss, a quantum calculation is needed for the loss cross section. The energy scale, ϵ_d, beyond which classical scattering calculation of the loss cross section is valid is approximated

as [27]

$$\epsilon_d = \frac{4\pi\hbar^2}{m_t\sigma} \tag{2.44}$$

where m_t is the mass of the trapped atom species and σ is the total cross section. For collisions between ^{87}Rb and ^{40}Ar in their ground state ϵ_d is 8.9 mK [1].

The calculation of $\langle\sigma_{\text{loss}}v_{\text{Ar}}\rangle_{^{87}\text{Rb},^{40}\text{Ar}}$ depends on what state the background atoms and trapped atoms are in. The long-range form of the potential when the ^{87}Rb is excited and ^{40}Ar is in its ground state is $V(r) = -\frac{C_6}{r^6}$. If f is the fraction of trapped atoms in the excited state then the expected collision cross section is

$$\langle\sigma_{\text{loss}}v_{\text{Ar}}\rangle_{^{87}\text{Rb},^{40}\text{Ar}} = (1-f)\langle\sigma_{\text{loss,g}}v_{\text{Ar}}\rangle_{^{87}\text{Rb},^{40}\text{Ar}} + f\langle\sigma_{\text{loss,e}}v_{\text{Ar}}\rangle_{^{87}\text{Rb},^{40}\text{Ar}} \tag{2.45}$$

where the subscript e and g refer to when ^{87}Rb is in the excited state or the ground state, respectively.

The next chapter describes the experimental verification of the dependence of the velocity averaged loss cross section on trap depth. ^{87}Rb was the trapped atom species and ^{40}Ar was the background species. Further reference to σ implicitly means the loss cross section σ_{loss} unless otherwise noted.

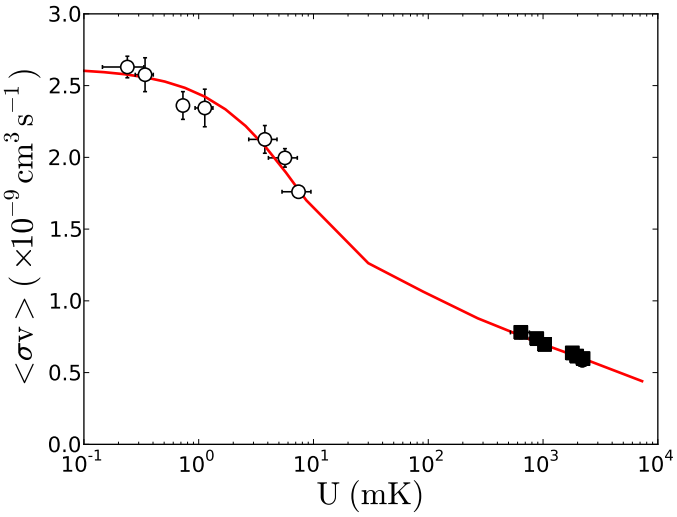

Figure 2.2: The velocity averaged loss cross section plotted versus trap depth showing a decrease in the loss cross section with increasing trap depth. As trap depth increases the kinetic energy required to leave the trap grows and the probability of a collision with a background gas particle imparting sufficient energy to leave the trap decreases. The curve is generated by numerically calculating $\langle \sigma_{\rm loss} v_{\rm Ar} \rangle_{^{87}{\rm Rb},^{40}{\rm Ar}}$ at discrete trap depths for ^{87}Rb as the trapped species and ^{40}Ar as the background species both in their ground state. The potential used in the calculation is $V(r) = \frac{C_{12}}{r^{12}} - \frac{C_6}{r^6}$. The coefficients are taken to be $C_6 = 280 E_{\rm H} a_{\rm B}^6$ and $C_{12} = 8.6 \times 10^7 E_{\rm H} a_{\rm B}^{12}$ where $E_{\rm B} = 4.35974 \times 10^{-18}$ J and a_B is the Bohr radius [1, 24]. The points superimposed on the curve are experimental data.

Chapter 3

Experimental verification of the dependence of the loss cross section on trap depth

The first section of this chapter describes how the velocity averaged collisional cross section for loss, $\langle \sigma v_i \rangle_{X,i}$, due to collisions between trapped atoms of type X and background gas of species i is measured. In our experiments we used ^{87}Rb as the trapped species, X, and ^{40}Ar as the background species i. The velocity averaged loss cross section $\langle \sigma v_{\mathrm{Ar}} \rangle_{^{87}\mathrm{Rb},^{40}\mathrm{Ar}}$ was calculated for a range of trap depths and measured previously by members of our lab using a magnetic trap [1, 17]. The magnetic trap used could obtain trap depths up to 10 mK. The work performed for this thesis was the measurement of $\langle \sigma v_{\mathrm{Ar}} \rangle_{^{87}\mathrm{Rb},^{40}\mathrm{Ar}}$ at larger trap depths using a MOT. A technique adapted from Hoffmann et al. [28] to measure the trap depth of a MOT is described. It is also proposed that the dependence of $\langle \sigma v_i \rangle_{X,i}$ on trap depth can be used as a measurement technique for trap depth. The work described in this chapter is also reported in [14].

3.1 Experimental apparatus

Our apparatus consisted of optics and a vacuum apparatus to produce a 3D MOT as well as to introduce a background gas to the 3D MOT. The $5^2S_{1/2}$ to $5^2P_{3/2}$ transition was used for trapping of either ^{85}Rb or ^{87}Rb. The pump was chosen to be the $F = 2$ to $F' = 3$ transition for ^{87}Rb and $F = 3$ to $F' = 4$ transition for ^{85}Rb. The repump was chosen to be the $F = 1$ to $F' = 2$ transition for ^{87}Rb and $F = 2$ to $F' = 3$ transition for ^{85}Rb. A schematic of the optical setup is shown in Fig. 3.1. On a separate table, shared among several experiments, external cavity diode lasers generate laser light locked 180 MHz below the pump and repump transitions using saturated absorption signals [29, 30]. The pump light was fibered over to the experimental table where it injected a diode laser amplifier (fiber FC1) to provide more power

for the experiment than was sent in the fiber. The repump light in fiber FC2 was not amplified. Double pass acousto-optical modulator (AOM) setups were used to bring the pump and repump frequencies from the fibers to the values used in the experiment [31]. The frequency shifted pump and repump light were combined together and sent to the MOT optics.

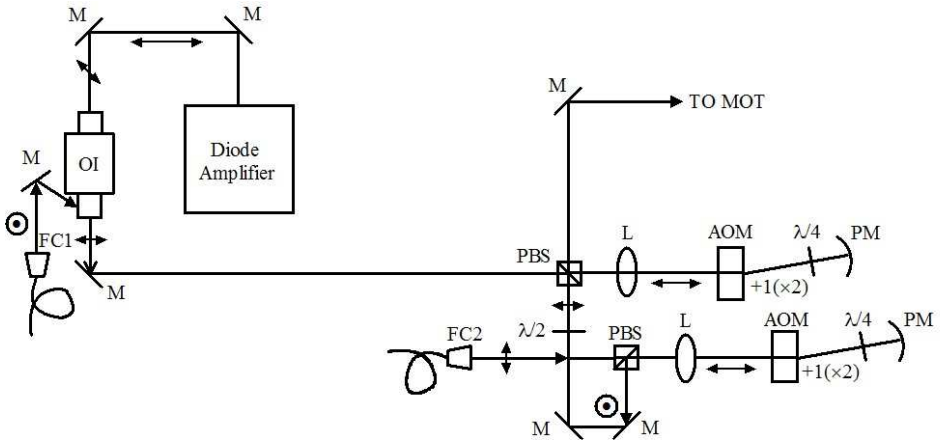

Figure 3.1: A schematic of the optical setup used to produce the pump and repump light for the MOT used in the loss cross section measurement experiment. Light from the master table was used to inject a diode amplifier via fiber FC1. An acousto-optical modulator (AOM) was used to bring the output of the amplifier from 180 MHz to 12 MHz below the pump resonance. Repump light from fiber FC2 from the master table was also brought up to resonance using an AOM in double pass configuration. The pump and repump beams were combined and sent towards the MOT optics. M: mirror, L: lens (PCX 300 mm), OI: optical isolator, PM: parabolic mirror 300mm focal length, Q: quarter wave plate, H: half wave plate, PBS: polarizing beam splitter.

A retroreflected 3D MOT configuration was used with a maximum six beam total power of 18.3 mW for the pump and 0.3 mW for the repump. The $1/e^2$ horizontal (vertical) diameter of the MOT beams was 7.0 (9.5) mm. This corresponds to a maximum pump intensity of 34.5 mW/cm^2.

The axial magnetic field gradient used for the MOT was 27.9(0.3)G/cm. To achieve different MOT trap depths different pump intensities and detunings were selected with the AOM used for the pump light. A glass cell of dimensions 1 cm by 1cm by 3.5 cm under vacuum was used. Rb vapour was

introduced into the system by running current through a Rb dispenser (Alvatec Rb-20). The system also contains an ion pump (PS-100 Thermionics) and a non-evaporable getter pump (SAES getters).

To introduce Ar into the system, a portable station was attached to a valve on the MOT vacuum chamber by a flexible bellows. This station (called the 'bakeout station') has a turbo pump (TV-70 Varian), a scroll pump (SH 100, Varian), a residual gas analyzer (RGA) (RGA200, Standford Research Systems), an ion gauge (843 Varian), and a leak valve(951-5106 Varian). The Ar could be introduced in the MOT region through the leak valve while the pressure of the Ar was measured with the RGA.

3.2 Measurement of $\langle \sigma v_{\mathrm{Ar}} \rangle_{^{87}\mathrm{Rb},^{40}\mathrm{Ar}}$

The velocity averaged loss cross section $\langle \sigma v_{\mathrm{Ar}} \rangle_{^{87}\mathrm{Rb},^{40}\mathrm{Ar}}$ can be measured for a trap of a certain trap depth by measuring the background collision loss rate constant, Γ, at various measured densities, n_{Ar}, of ^{40}Ar. Eq. 2.1 predicts that plotting Γ vs n_{Ar} will give a linear relationship with a slope of $\langle \sigma v_{\mathrm{Ar}} \rangle_{^{87}\mathrm{Rb},^{40}\mathrm{Ar}}$. The velocity averaged loss cross section, $\langle \sigma v_{\mathrm{Ar}} \rangle_{^{87}\mathrm{Rb},^{40}\mathrm{Ar}}$, was measured in this manner for different trap depths of the MOT. As already mentioned, the different trap depths were attained by changing the intensity and detuning of the pump light. The technique for measuring the loss rate constant, Γ, in our magnetic and magneto-optical trap will be discussed next.

3.2.1 Measurement of Γ for a MOT

In a MOT when the magnetic field is first turned on atoms will start to accumulate in the intersection of the six laser beams comprising the MOT. The fluorescence from the trapped atoms can partially be captured by a lens and focused onto a photodiode. The photodiode voltage, $V(t)$, is proportional to the number of the atoms in the MOT, $N(t)$, where we assume

$$V(t) = \alpha \gamma_{\mathrm{sc}} N(t). \tag{3.1}$$

Here α is a proportionality constant relating the efficiency of collecting the photons being fluoresced by the atoms onto the photodetector and the conversion efficiency of photons to voltage by the photodetector. The scattering rate, γ_{sc}, is the rate at which an atom in the MOT scatters photons and is dependent on the frequency and intensity of the light.

For the purposes of obtaining the loss rate constant, Γ, we recorded the fluorescence voltage on the photodetector as a function of time as the

atoms accumulate in a MOT until a steady state voltage (atom number) is reached. Time $t = 0$ was set to be when the magnetic field was turned on with the repump and pump light already on. Fig. 3.2 shows an example of a MOT loading curve from which Γ can be determined [14]. This is a plot

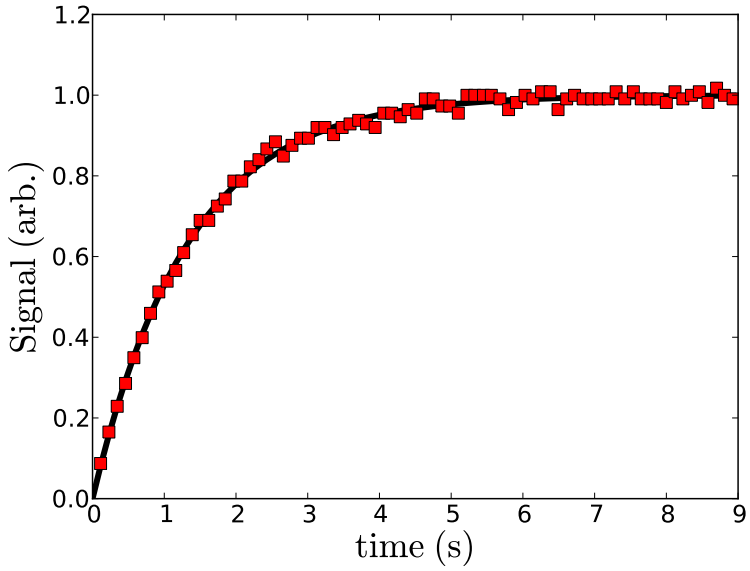

Figure 3.2: The fluorescence signal of the atoms accumulating in a MOT as a function of time from the turn on of the magnetic field.

of the photodiode voltage versus time from initial turn on of the MOT. This loading curve can be fit to an equation proportional to Eq. 1.2 and Γ can be determined. For determination of Γ we do not need to know α and γ_{sc}.

3.2.2 Measurement of Γ for a magnetic trap

A magnetic trap is initially loaded by turning off the MOT light and turning up the current to the magnetic coils to increase the magnetic field gradient. A magnetic trap starts off with its maximal atom number which then decays over time. Eq. 1.9 models this decay with

$$\frac{N(t)}{N(0)} = e^{-\Gamma t} \tag{3.2}$$

where $N(t)$ is the number of atoms in the magnetic trap after a hold time, t, from initial loading of $N(0)$ atoms. Consider instead the ratio $\frac{N(t)}{N_{\mathrm{MOT}}}$ where N_{MOT} is the steady state number of atoms in the MOT before loading into the magnetic trap. The initial number in the magnetic trap is proportional to the steady state value in the MOT, $N(0) \propto N_{\mathrm{MOT}}$, so that

$$\frac{N(t)}{N_{\mathrm{MOT}}} \propto \frac{N(t)}{N(0)} = e^{-\Gamma t}. \tag{3.3}$$

Fig. 3.3 shows an example set of data taken to determine $\frac{N(t)}{N_{\mathrm{MOT}}}$ for a particular hold time, t. The experimental sequence is as follows:

(a) First the fluorescence voltage due to the steady state atom number in our MOT was recorded.

(b) The light was turned off and the magnetic field was increased to load atoms into a magnetic trap. The atoms were held in the magnetic trap for some hold time, t.

(c) The MOT light was turned back on and the magnetic field was put back to the settings used for the MOT. The MOT was then allowed to load for a short time.

(d) The magnetic field was turned off to let the trapped atoms escape. The MOT light was left on to record a background level.

(e) The magnetic field was turned back on allowing the MOT to reload completely before starting at step (a) again. Each cycle a different hold time was used.

Step c is needed because a magnetic trap has no light and the atoms do not fluoresce so that only background light is detected on the photodetector. In order to see how many atoms are left in the magnetic trap we turned the MOT conditions back on to detect the fluorescence. Because there are some atoms there to start with from the magnetic trap the fluorescence voltage will be higher than when loading the MOT initially.

We are interested in the ratio of the voltage corresponding to the number of atoms in the magnetic trap, $V_{\mathrm{MT}}(t)$, to the voltage in the steady state MOT, V_{MOT}. Both of these observables are labelled in Fig. 3.3. From Eq. 3.1 and Eq. 3.3 we have

$$\frac{V_{\mathrm{MT}}(t)}{V_{\mathrm{MOT}}} = \frac{N(t)}{N_{\mathrm{MOT}}} \propto \frac{N(t)}{N(0)} = e^{-\Gamma t}. \tag{3.4}$$

By measuring $\frac{V_{\mathrm{MT}}(t)}{V_{\mathrm{MOT}}}$ for different hold times and then fitting to an equation proportional to $e^{-\Gamma t}$ we could determine Γ. An example result is shown in Fig. 3.4.

3.2.3 Results of Γ vs n_{Ar} measurement

Fig. 3.5 shows the loss rate constant versus argon density, Γ vs n_{Ar}, for two different trap depths obtained using a magnetic trap and a MOT. The relationship is linear and the slope, $\langle \sigma v_{\mathrm{Ar}} \rangle_{^{87}\mathrm{Rb},^{40}\mathrm{Ar}}$, is larger for the smaller trap depth of the magnetic trap as predicted.

Measuring Γ vs n_{Ar} provides a method of measuring $\langle \sigma v_{\mathrm{Ar}} \rangle_{^{87}\mathrm{Rb},^{40}\mathrm{Ar}}$ for a given trap depth. We measured $\langle \sigma v_{\mathrm{Ar}} \rangle_{^{87}\mathrm{Rb},^{40}\mathrm{Ar}}$ for a range of trap depths accessible by our magnetic trap (0 - 10 mK) and our MOT (500 mK to 2 K). The trap depth of a magnetic trap can be calculated as described in section 1.2.2. By varying the magnetic trap gradient different trap depths can be chosen. The trap depths for various MOT settings was determined using the 'catalysis method' described in the next section.

3.3 MOT Trap depth determination by the 'Catalysis method'

Fig. 3.6 shows a mechanism of imparting kinetic energy to trapped atoms [28]. Two cold ground state atoms in the trap separated by a certain internuclear separation are photo-associated by a 'catalysis' laser to a repulsive molecular potential. The atoms quickly move apart picking up kinetic energy and then spontaneously emit back to the ground state. The kinetic energy picked up by each atom in the case of homonuclear collisions is $h\Delta/2$ where Δ is the detuning of the catalysis laser above the atomic resonance between the ground and the excited state (in our case $5^2S_{1/2}$ to $5^2P_{3/2}$ for ^{87}Rb). If $h\Delta/2 > U$, where U is the trap depth, then the catalysis laser will cause loss of the atoms from the trap.

Fig. 3.7 shows the experimental setup used to measure the trap depth of a MOT. The MOT setup is described earlier in section 3.1. A Coherent Titanium:Sapphire Ring laser (899-01) pumped by a Verdi V10 Coherent laser was used as the catalysis laser. The frequency of the catalysis laser was set by a dc input voltage, from a frequency generator, fed to the control box. This voltage was stepped through discretely to increment the catalysis laser frequency. A small portion of the catalysis laser light was sent to a wavemeter (Bristol 621). The rest of the light was sent through an AOM

(IntraAction Corp. ADM-602AF3) and the first order used. The AOM was used to turn the catalysis laser on and off at a duty cycle given by a frequency generator (Standford Research Systems DS345) sent to the AOM driver (IntraAction Corp. DE-603H6). The first order of the AOM was coupled into a single mode polarization preserving fiber and transferred to the MOT setup. The catalysis light was focused to ≈ 1 mm, with an intensity of ≈ 2 W/cm^2, and overlapped with the trapped atoms in the MOT. A photodiode was used to monitor the fluorescence of the MOT in steady state without the catalysis light and also in the presence of the catalysis light with a certain duty cycle. A LabVIEW program was used to control the frequency generators responsible for stepping through different catalysis laser frequencies and for turning on and off the catalysis light being sent to the MOT. The LabVIEW program was used to capture fluorescence data from an oscilloscope (Tektronix TDS3014) as described later in this section, as well as to record the catalysis light frequency from the wavemeter.

Part of the catalysis light (not shown in Fig. 3.7) was sent to a Rb cell (Triad Technology Inc. TT-Rb-75-V-P). This was so that the catalysis laser could be scanned over the Rb absorption lines to see how the laser was behaving and to position the frequency at an appropriate starting place for the catalysis laser experiments. As mentioned, the catalysis laser light was focused onto the trapped atoms to be roughly the same size as the cloud of atoms. For initial alignment of the catalysis laser onto the trapped atoms in the MOT the catalysis laser was tuned to the MOT pump atomic resonance. During this alignment process the intensity was attenuated by neutral density filters so that the atoms could still be trapped with the catalysis laser on. In the presence of resonant catalysis light the fluorescence was lowered. The mirrors sending the catalysis laser light to the MOT were adjusted to minimize the fluorescence of the MOT so that the catalysis beam had maximal overlap with the trapped atoms.

The presence of the catalysis laser affects the loading dynamics in a MOT so that Eq. 1.1 becomes [28]

$$\frac{dN}{dt} = R - \Gamma N - (\beta + d \cdot \beta_{\mathrm{cl}}) \int n^2(\vec{r}, t)\, d^3\vec{r} \tag{3.5}$$

where β_{cl} is the contribution to the two body intra-trap loss constant due to the presence of the catalysis laser and β is the contribution from all other two body intra-trap losses not mediated by the catalysis laser. We consider the case where the catalysis laser is modulated on and off with duty factor, d, where duty factor is the percentage of on time. β_{cl} will increase as the laser detuning Δ approaches the value where $h\Delta/2 = U$ where U is the

trap depth of the trap. As detuning Δ increases past that condition $\beta_{\rm cl}$ will decrease. Following the argument made in [28], $\beta_{\rm cl} \propto \sigma P(h\Delta/2)$, where σ is the photoassociative cross section and $P(h\Delta/2)$ is the probability of escape of a trapped atom with kinetic energy $h\Delta/2$. The cross section can be written as $\sigma = \pi r^2 f$ where r corresponds to the internuclear separation at which the catalysis laser transition occurs for a given detuning Δ. The excitation probability, f, is inversely proportional to $\frac{dV}{dr}$. For a potential of $V(r) = -\frac{C_3}{r^3}$ and for $V(r) = h\Delta$ this gives $\sigma \propto \Delta^{-2}$. This means that $\beta_{\rm cl}$ will decrease for detunings greater than $h\Delta/2 = U$ due to the decreasing probability of excitation for decreasing internuclear separation [28]. Fig. 3.10 shows a plot of a measure of $\beta_{\rm cl}$ versus detuning, Δ.

The steady state number for the trap when the catalysis light is present with duty factor, d, is

$$N_{\rm ss} = \frac{R}{\Gamma + (\beta + d\beta_{\rm cl})n_{\rm ss}}. \tag{3.6}$$

Taking the ratio of $N_{\rm ss}$ with the steady state number when the catalysis laser is not present, $N^0_{\rm ss}$, gives

$$\frac{N^0_{\rm ss}}{N_{\rm ss}} = 1 + \frac{\beta_{\rm cl} n_{\rm ss} d}{\Gamma + \beta n_{\rm ss}}. \tag{3.7}$$

Experimentally the ratio of $\frac{N^0_{\rm ss}}{N_{\rm ss}}$ was determined from $\frac{V^0_{\rm ss}}{V_{\rm ss}}$ as per Eq. 3.1. Here $V^0_{\rm ss}$ is the steady state fluorescence voltage from the trapped atoms when the catalysis laser is off. $V_{\rm ss}$ is the steady state voltage when the catalysis laser is on with duty factor, d. Rearranging Eq. 3.7 we define the parameter J as

$$J = \frac{N^0_{\rm ss}}{N_{\rm ss}} - 1 = (\frac{\beta_{\rm cl} n_{\rm ss}}{\Gamma + \beta n_{\rm ss}})d. \tag{3.8}$$

As long as d is not too large so as to change the steady state density $n_{\rm ss}$, the relationship between J and d will be linear. Fig. 3.8 shows J as a function of d for different catalysis laser detunings. Fig. 3.9 shows the portion over which J versus d is linear. The slope of the linear portion of J vs d is proportional to $\beta_{\rm cl}$ values. Plotting this slope as a function of catalysis laser detuning provides a measure of $\beta_{\rm cl}$ and will be maximum when $h\Delta/2 = U$. Fig. 3.10 shows an example set of data for a MOT whose trap depth was determined from this data to be $U = 0.64(0.12)K$. We note that Hoffmann et al. [28] plot the probability of a trapped atom escaping as a function of Δ. They interpret the detuning, Δ, at which this probability starts to increase past approximately 30 % to correspond to the trap depth.

3.4 Comparison of measurement with theory

The catalysis laser provides a means of determining the depth of a MOT. Measuring Γ versus n_{Ar} provides a method of determining $\langle \sigma v_{\mathrm{Ar}} \rangle_{^{87}\mathrm{Rb},^{40}\mathrm{Ar}}$. The theoretical predictions of $\langle \sigma v_{\mathrm{Ar}} \rangle_{^{87}\mathrm{Rb},^{40}\mathrm{Ar}}$ versus trap depth U can now be compared with experimentally measured values. Fig. 3.11 shows that the experimental results follow the predicted dependence (this is the same figure shown in Fig. 2.2). A zoomed in portion of the curve for the data taken with a magneto-optical trap is given in Fig. 3.12

It should be noted that measurements of $\langle \sigma v_{\mathrm{Ar}} \rangle_{^{87}\mathrm{Rb},^{40}\mathrm{Ar}}$ and U did not necessarily fall on the predicted curve before a corrective factor was applied to the $\langle \sigma v_{\mathrm{Ar}} \rangle_{^{87}\mathrm{Rb},^{40}\mathrm{Ar}}$ measurements. This corrective factor was necessary due to calibration inaccuracies in determining n_{Ar} with the residual gas analyzer. To account for this the loss rate constant, Γ, for a magnetic trap, with trap depth 3.14(0.84) mK, was measured at each n_{Ar} where Γ for a particular MOT setting was also measured. The trap depth of the magnetic trap was calculated and the theoretical value of $\langle \sigma v_{\mathrm{Ar}} \rangle_{^{87}\mathrm{Rb},^{40}\mathrm{Ar}}$ for that trap depth was calculated. The ratio of the measured and calculated value of $\langle \sigma v_{\mathrm{Ar}} \rangle_{^{87}\mathrm{Rb},^{40}\mathrm{Ar}}$ for the magnetic trap provided a correction factor for all the $\langle \sigma v_{\mathrm{Ar}} \rangle_{^{87}\mathrm{Rb},^{40}\mathrm{Ar}}$ values taken for the MOT settings. Table 3.1 gives the velocity averaged loss cross section values for various pump intensities and detunings.

Table 3.1: Velocity averaged loss cross section, $\langle \sigma v_{\mathrm{Ar}} \rangle_{^{87}\mathrm{Rb},^{40}\mathrm{Ar}}$, measurements for various MOT pump intensities and detunings.

MOT detuning (MHz)	Intensity (mW cm^{-2})	$\langle \sigma v_{\mathrm{Ar}} \rangle_{^{87}\mathrm{Rb},^{40}\mathrm{Ar}}$ ($\times 10^{-9}$cm^{3}s^{-1})
-5	2.7	0.780 (0.043)
-8	2.7	0.737 (0.033)
-10	2.7	0.696 (0.031)
-12	6.9	0.637 (0.008)
-12	9.6	0.615 (0.006)
-12	34.5	0.598 (0.003)

3.5 Proposal for a new trap depth measurement technique

This chapter has focused on confirming that the shape of the calculated $\langle \sigma v_{\mathrm{Ar}} \rangle_{^{87}\mathrm{Rb},^{40}\mathrm{Ar}}$ vs U curve agrees with measurement. It is proposed that this dependence can be used to determine the depth of a trap by measuring the velocity averaged loss cross section and determining based on calculation what trap depth this corresponds to. The loss rate constant, Γ, can be measured for a trap as a function of n_i where n_i the density of background species of choice i. The slope of Γ versus n_i gives $\langle \sigma v_i \rangle_{X,i}$. The value of $\langle \sigma v_i \rangle_{X,i}$ can be calculated for a sufficient number of trap depths in the region where the depth of the trap is estimated to be and can be numerically fit to give a dependence of $\langle \sigma v_i \rangle_{X,i}$ on U. This dependence of $\langle \sigma v_i \rangle_{X,i}$ on U can then be inverted to give U as a function of $\langle \sigma v_i \rangle_{X,i}$. The measured $\langle \sigma v_i \rangle_{X,i}$ from the slope of Γ vs n_i can be used to determine trap depth. The accuracy of this trap depth determination would be limited by the accuracy to which n_i is known. As described above, inaccuracies in density measurement can be corrected for when measuring $\langle \sigma v_i \rangle_{X,i}$ for a trap whose depth is unknown if $\langle \sigma v_i \rangle_{X,i}$ is also measured simultaneously for a known trap depth. Table A.1 shows trap depths measured using the catalysis techniques for various pump detunings and intensities. The trap depths determined by numerical fitting as described above are also included.

Table 3.2: 3D MOT trap depths for various pump detunings and intensities. The trap depths, U_{cat}, were determined using the catalysis method described in section 3.3. As a comparison the trap depths were also obtained by fitting the numerically calculated $\langle \sigma v_{\mathrm{Ar}} \rangle_{^{87}\mathrm{Rb},^{40}\mathrm{Ar}}$ vs U and then determining trap depth from measured values of $\langle \sigma v_{\mathrm{Ar}} \rangle_{^{87}\mathrm{Rb},^{40}\mathrm{Ar}}$. Trap depths determined numerically are denoted $U_{\langle \sigma v \rangle}$

Detuning (MHz)	Intensity (mW cm^{-2})	$U_{\langle \sigma v \rangle}$ (K)	U_{cat} (K)
-5	2.7	0.55 (0.15)	0.64 (0.12)
-8	2.7	0.77 (0.17)	0.88 (0.12)
-10	2.7	1.05 (0.22)	1.03 (0.12)
-12	6.9	1.64 (0.10)	1.80 (0.18)
-12	9.6	1.93 (0.07)	1.99 (0.18)
-12	34.5	2.20 (0.05)	2.23 (0.24)

A complication of the trap depth measurement technique using back-

ground collisions is that the $\langle \sigma v_i \rangle_{X,i}$ value changes depending on the state of the trapped atom X. For both Rb and Ar in their ground state, Mitroy and Zhang [32] give $C_6 = 336.4$ in a.u. For Rb in its np excited state and Ar in its ground state the long range potential is given as $V(r) = -\frac{C_6}{r^6}$. In this case $C_6 = 924.1$ for the Σ molecular state, and for the Π molecular state it is $C_6 = 545.1$, both in atomic units. This gives a total velocity averaged collision cross section, $\langle \sigma v_{\mathrm{Ar}} \rangle_{^{87}\mathrm{Rb},^{40}\mathrm{Ar}}$, in the three cases of 2.8×10^{-9}, 4.2×10^{-9} , 3.4×10^{-9} cm^3 s^{-1}, respectively. For ^{40}Ar as the background choice an estimate of excited state fraction in our MOT at a maximum of 15% did not cause significant error in the agreement of the measured $\langle \sigma v_i \rangle_{X,i}$ with the $\langle \sigma v_i \rangle_{X,i}$ calculated for ground state rubidium.

As mentioned, it was necessary to correct the measurements of $\langle \sigma v_{\mathrm{Ar}} \rangle_{^{87}\mathrm{Rb},^{40}\mathrm{Ar}}$ to account for pressure measurement inaccuracies in the density of ^{40}Ar. The accuracy of the density measurement can only be roughly estimated. Present pressure gauges in the $\approx 10^{-8}$ Torr range, as will be discussed in the next chapter, are subject to calibration drift. Calibration is difficult and expensive and depends on gas type. It is proposed by our lab (Dr. James Booth and Dr. Kirk Madison), that the atoms themselves could serve to provide accurate and stable measurements of the density of argon, n_{Ar}, as well as possibly of other desired background gases. The idea is based on the relationship between the loss rate constant, Γ, due to background collisions and knowledge of the velocity averaged loss cross section. The remaining chapters of this thesis focus on the proposal of using trapped atoms as a pressure sensor. The next chapter introduces existing gauges and standards, and explains more fully the concept of the 'atom pressure sensor'. The chapters afterwards describe the experimental progress made to date on the atom pressure sensor.

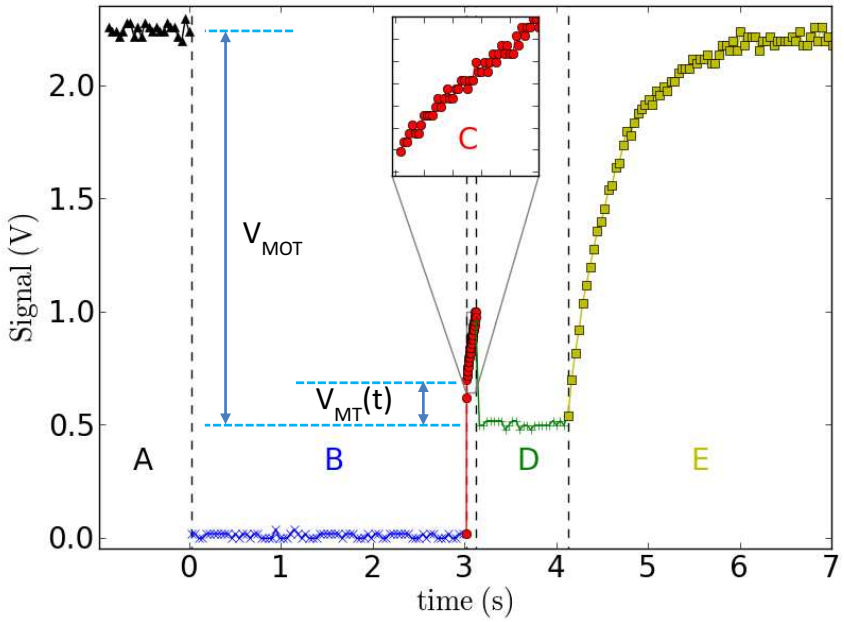

Figure 3.3: An example of data taken to determine $\frac{N(t)}{N_{\mathrm{MOT}}}$ for a certain hold time, t, in the magnetic trap. A) First the fluorescence voltage is recorded for a MOT in steady state. B) Atoms are loaded into the magnetic trap by turning off the MOT light and ramping up the magnetic field. The atoms are held in the magnetic trap for a hold time, t. C) The MOT light is turned back on and the magnetic field set to the MOT setting. The MOT is allowed to load for a short amount of time in order to get a line that one can use to extrapolate the fluorescence voltage when the MOT light was first turned back on. D) The magnetic field is turned off while the light is left on which dumps the atoms from the trap. E) The magnetic field is turned back on to its MOT setting and the MOT is reloaded back to its steady state atom number. The difference between voltage levels D and the start of C, labelled $V_{\mathrm{MT}}(t)$, is proportional to the number of atoms in the magnetic trap, $N(t)$, after hold time, t. The difference between voltage levels A and D, labelled V_{MOT}, is proportional to the number of atoms in the MOT, N_{MOT}. As shown here the hold time was long and not many atoms remained in the magnetic trap.

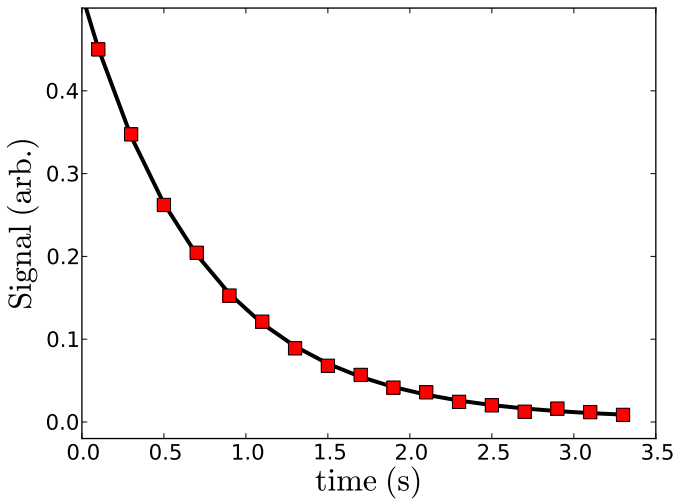

Figure 3.4: The number of atoms in the magnetic trap divided by the original steady state number in the MOT, $\frac{N(t)}{N_{\mathrm{MOT}}}$, measured as a function of hold time,t. Each point is generated as described in Fig. 3.3. The data is fit to an equation proportional to $e^{-\Gamma t}$ to determine the background loss rate constant, Γ.

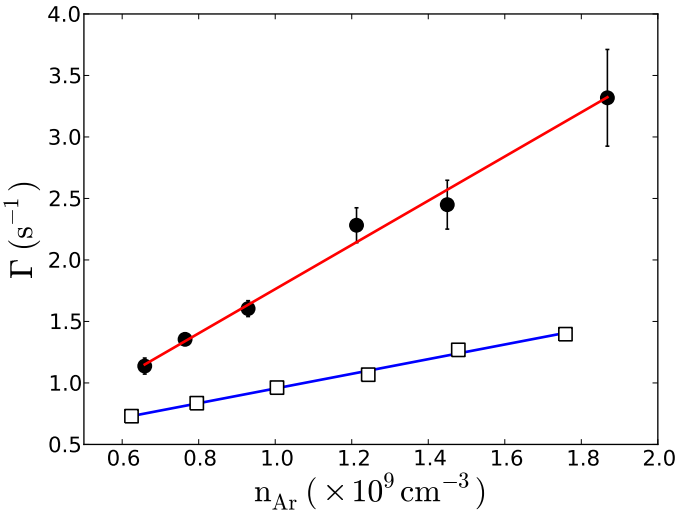

Figure 3.5: The background loss rate constant, Γ is measured for a MOT (squares) and a magnetic trap (circles) as a function of the density of argon n_{Ar}. The density of argon was measured using a residual gas analyzer as described in section 3.1. The slope of Γ vs n_{Ar} is equal to the velocity averaged cross section for loss between trapped ^{87}Rb atoms and ^{40}Ar background atoms $\langle \sigma v_{\mathrm{Ar}} \rangle_{^{87}\mathrm{Rb},^{40}\mathrm{Ar}}$. The slope for the magnetic trap is greater than for a MOT because the magnetic trap has a smaller trap depth and the probability of background collisions causing loss is greater.

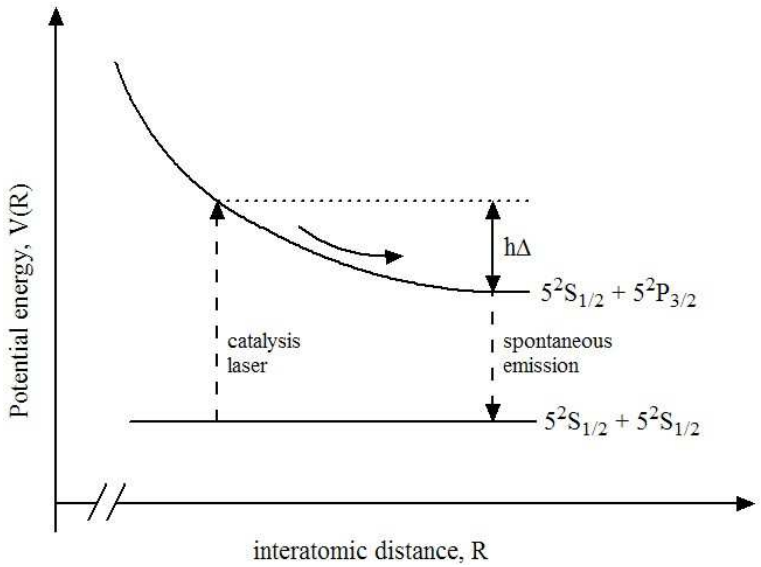

Figure 3.6: A 'catalysis laser' excites the ground state atoms to a repulsive excited molecular potential. The atoms quickly repel each picking up $h\Delta/2$ in kinetic energy for the homonuclear case. Δ is the detuning of the catalysis laser above the $5^2S_{1/2}$ to $5^2P_{3/2}$ atomic resonance for ^{87}Rb. If the kinetic energy imparted to the atoms is greater than the trap depth loss will result.

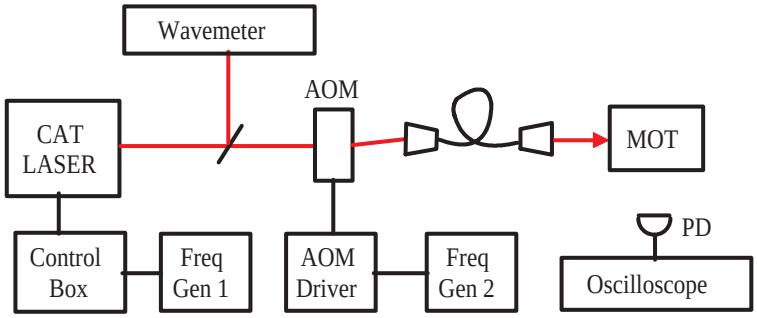

Figure 3.7: The experimental setup used to measure the trap depth of a MOT using a catalysis laser (CAT laser). The catalysis laser frequency is measured with a wavemeter. The frequency of the CAT laser is control by external control of the laser control box with a frequency generator. The catalysis light was sent through an acousto-optical modulator (AOM) and the first order used for the experiment. The AOM driver had a TTL input so that a function generator could be used to turn the catalysis light on and off at a given duty cycle. The catalysis light was fibered over to the MOT and aligned onto the MOT atom cloud. The fluorescence of the MOT in steady state with no catalysis light and with catalysis light on at a certain duty cycle was recorded with a photodiode and an oscilloscope. A Labview code was used to control the function generator and read from the wavemeter and oscilloscope by GPIB.

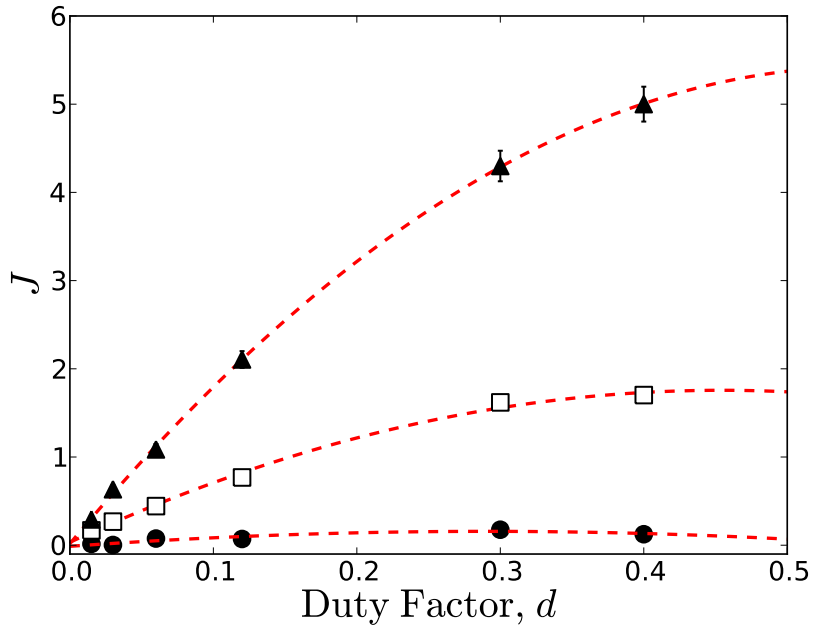

Figure 3.8: $J = \frac{N_{ss}^0}{N_{ss}} - 1$ vs the catalysis laser duty factor d. For small duty factors the steady state density of the MOT, n_{ss} is unaffected and J vs d is linear. As d increases too much n_{ss} becomes dependent on d and the curve becomes non linear. Each of the curves is for a different catalysis laser detuning.

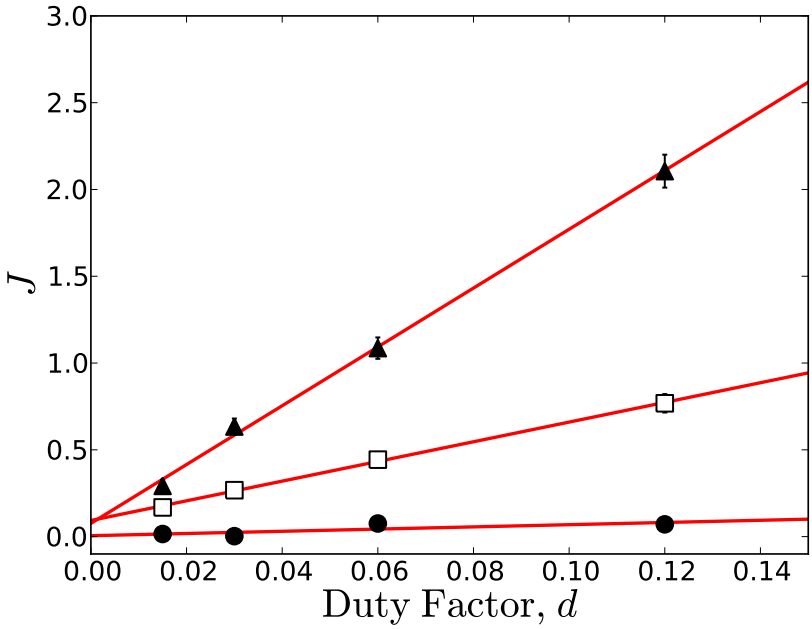

Figure 3.9: J vs d shown taken from Fig.3.8 in the linear region. The slope as given by Eq. 3.8 is proportional to the loss rate constant β_{cl} for the repulsive loss mechanism induced by the catalysis laser. Each of the curves is for a different catalysis laser detuning.

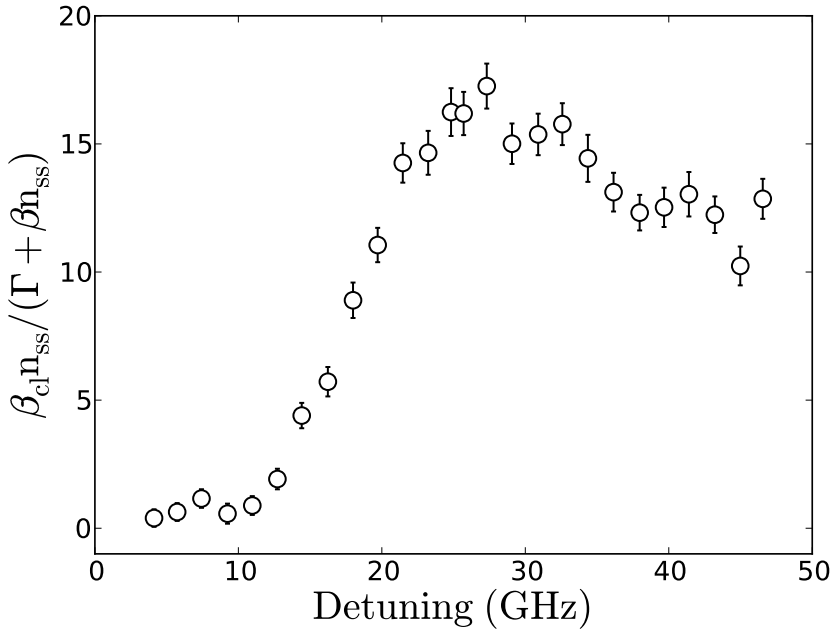

Figure 3.10: The slope of the J vs d curve (as shown in Fig. 3.9)is plotted as a function of catalysis laser detuning. The J vs d curve is proportional to the loss rate constant β_{cl} for the repulsive loss mechanism induced by the catalysis laser and the detuning, Δ at which β_{cl} is maximal corresponds to $h\Delta/2 = U$ where U is the depth of the trap. In this manner the trap depth can be measured for a MOT. The data shown is for a ^{87}Rb MOT with a pump detuning of -5 MHz and a pump intensity of 2.7 mW cm^{-2}

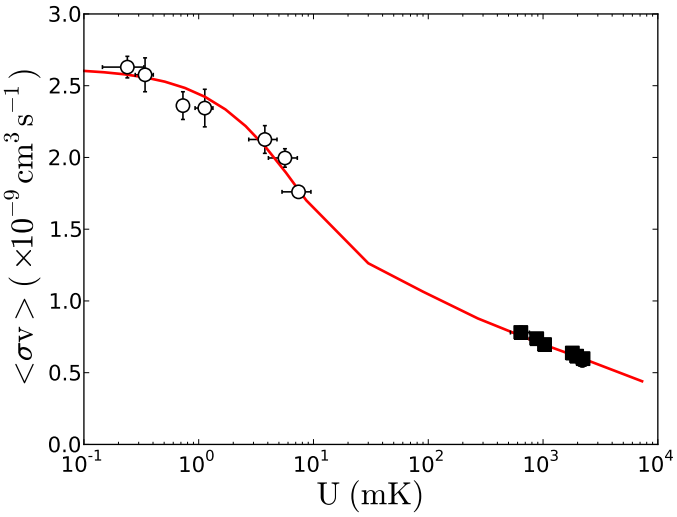

Figure 3.11: The velocity averaged loss cross section plotted versus trap depth showing a decrease in the loss cross section with increasing trap depth. As trap depth increases the kinetic energy required to leave the trap grows and the probability of a collision with a background gas particle imparting sufficient energy to leave the trap decreases. The curve is generated by numerically calculating $\langle \sigma v_{\mathrm{Ar}} \rangle_{^{87}\mathrm{Rb},^{40}\mathrm{Ar}}$ at discrete trap depths for ^{87}Rb is the trapped species and ^{40}Ar as the background species. The points superimposed on the curve are experimental data.

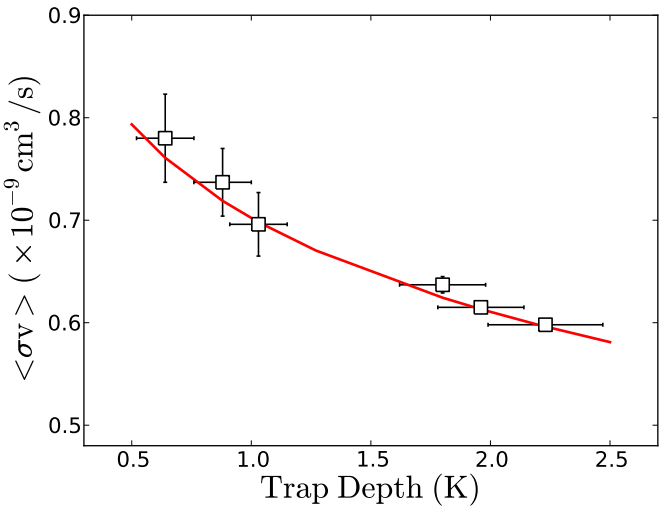

Figure 3.12: The velocity averaged loss cross section plotted versus trap depth for the data taken with a magneto-optical trap. The trap depth of the trap was changed by varying the pump detuning and intensity.

Chapter 4

Proposal for a Cold Atom Based Pressure sensor

The method of pressure measurement we will discuss actually measures the local density where the trapped atoms are situated. For sufficiently low pressures and high temperatures, the pressure, P, of a gas relates to its density by the ideal gas law. The ideal gas law is $PV = Nk_BT = nRT$, where N is the total number of atoms in volume V, k_B is Boltzmann's constant, T is the temperature, n is the number of moles, and R is the Rydberg constant. The official SI unit of pressure is the Pascal (Pa). In North America (particularly in the US) a commonly used unit is Torr where 1 Torr = 133.3 Pa. Ranges of vacuum are defined as low/rough vacuum (10^5 to 10^2 Pa), medium/fine vacuum (10^2 Pa to 10^{-1} Pa), high vacuum (HV)(10^{-1} to 10^{-6} Pa), ultra-high vacuum (UHV)(10^{-6} to 10^{-10} Pa) and extremely high vacuum (XHV)(10^{-10} Pa and below) [33].

There are a variety of pressure measurement devices (pressure gauges) on the market, most of which have to be calibrated by a primary or a transfer standard. A primary standard is a 'measurement standard established using a primary reference measurement procedure, or created as an artifact, chosen by convention'. A primary reference measurement procedure gives '...a measurement result without relation to a measurement standard for a quantity of the same kind'. Quantities of the same 'kind' require the same units (for example diameter and circumference are of the kind length) [34].

An example of a primary pressure standard is a mercury manometer (Fig. 4.1). The pressure difference, $P_1 - P_2$, between two connected columns, partially filled with mercury, is determined by the height difference h of the mercury in each column. The relation is $P_1 - P_2 = \rho gh$ where ρ is the density of mercury. By pumping down on one side so that $P_2 \ll P_1$ we have $P_1 \approx \rho gh$.

Primary standards are normally quite involved both in apparatus and technique so that they are not employed as gauges in a commercial way. Instead they are maintained by national laboratories who use their primary standards to calibrate commerical gauges that can then be used as transfer

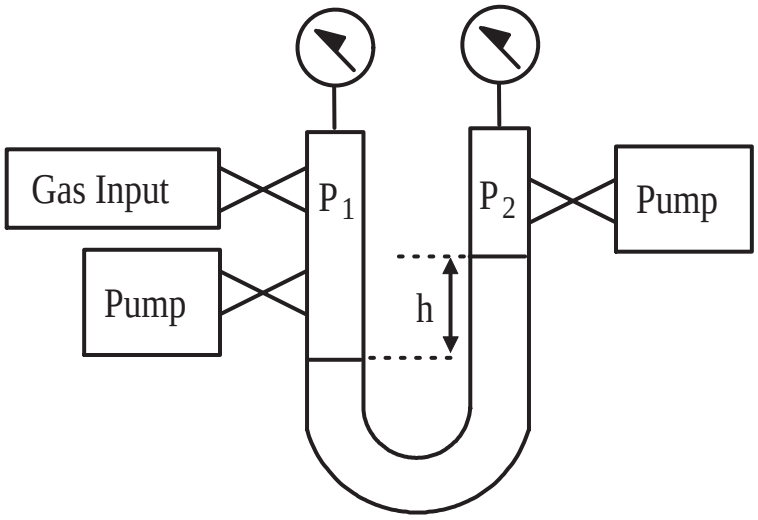

Figure 4.1: A mercury manometer is used as a primary pressure standard relating the height difference, h of mercury in a connected tube to the pressure difference by $P_1 - P_2 = \rho g h$. Both the density of mercury is ρ and height difference h are traceable to primary standards in length and mass.

standards. This chapter begins with discussion of some existing pressure gauges for the HV and UHV range and some existing primary pressure standards for the UHV vacuum range. At the end of the chapter a proposed primary pressure standard based on cold trapped atoms is discussed.

4.1 Pressure gauges

In this section we describe several pressure gauges used in the HV and UHV range. The focus is on pressure gauges that are used in our experimental apparatus for our proposed pressure standard.

4.1.1 Capacitance diaphragm gauge

Fig. 4.2 shows a schematic representation of a capacitance diaphragm gauge. The capacitance diaphragm gauge consists of a sealed chamber divided into two sections by a thin incon el tensioned sheet of metal (the diaphragm). For absolute pressure measurement one side is evacuated to low pressure $\approx P_{\text{ref}} = 0$ and sealed. A chemical getter is included to absorb any particles

that outgas from the gauge material in order to maintain low pressure after this section is sealed. On the other side of the diaphragm there is an inlet to accept the gas whose pressure P_x is to be measured. The diaphragm will deflect by an amount related to the pressure of the gas introduced. On the evacuated side several electrodes are placed so that the diaphragm forms a capacitor with each electrode. These two capacitance signals, C_1 and C_2 in Fig.4.2, are fed into an AC bridge via connections A, B, and C. Fig. 4.3 shows an AC bridge where the voltage V across the bridge is zero if the impedance Z_1, Z_2, Z_3 and Z_4 satisfies $\frac{Z_1}{Z_3} = \frac{Z_2}{Z_4}$. For capacitors $Z = \frac{1}{i\omega C}$ where ω is the frequency of the AC source. As the diapraghm deflects with pressure the capacitances C_1 and C_2 inducing a voltage across the bridge. The voltage across the bridge versus pressure can be characterized and the device made to output a voltage that varies linearly with pressure. The 615A from MKS instruments for the 1 Torr range has a claimed accuracy of $\pm 0.25\%$ [35]. The pressure range for the gauge is 1×10^{-5} to 1 Torr. The pressure reading can change with temperature changes so that often they are temperature controlled [36].

4.1.2 Spinning rotor gauge

The spinning rotor gauge consists of a set of magnets and magnetic coils in the midst of which a magnetized steel ball is levitated (shown in Fig. 4.4). The ball (R) is levitated by two permanent magnets (M). Using drive coils (D) the ball is set to spin at a certain number of revolutions per second as detected by two pick-up coils (P). Two stabilization coils in the vertical direction (S) and four in the horizontal direction (L) are used to minimize deviations in the position of the rotor. The drive coils are then turned off and the rate of angular deceleration is measured. The relative rate of angular deceleration ($\frac{1}{\omega}\frac{d\omega}{dt}$) is proportional to the pressure of the environment surrounding the ball. The ball is within the vacuum surrounded by a steel tube. The magnets and sense coils slip over the tube and are external to the vacuum environment. When the ball is spinning eddy currents induced in the ball and surrounding structures will cause a 'residual drag' which results in a pressure reading even for zero pressure of gas and needs to be corrected for. Fluctuations of this residual drag limit the lowest pressure that can be detected by the SRG. The SRG3 from MKS instruments which is currently in our setup can read a pressure range of 5×10^{-5} Pa to 100 Pa. The quoted stability is $\leq 1\%$ per year [37]. To read accurately the device must be calibrated since exposure to air, travel, baking and remounting of the magnetic sensing head all effect the original calibration [38, 39].

4.1.3 Ionization gauge

In an ionization gauge (see Fig. 4.5) current is sent through a thin tungsten filament heating the filament. The filament emits electrons which are accelerated towards an anode grid at + 180V and follow trajectories around and through the grid until they hit the grid. As the electrons travel they can ionize gas they collide with forming positive ions. The grid surrounds a thin wire at 0V towards which any ions formed inside the grid will go to. This wire is called the ion collector. Ions formed outside the grid are accelerated towards the walls of the gauge (also held at 0V) and do not contribute to the ion collector current. The ratio of ion collector current to electron emission current is proportional to the pressure of the gas in which the gauge is situated and the gauge can be calibrated to give pressure readings. The calibration constant will change for different gas types because the ionization probability is different.

This gauge though popular has several unwanted features [40, 41]:

1. The calibration of the ion gauge can drift with time due to the sagging of elements in the ion gauge [42]. Any relative movement of the filament to the grid affects the electron trajectories either by changing the electron path length or by changing the amount of time the electron spends within the grid where detectable ions can be formed. Changes in electron trajectories will therefore change the ion collector current for a given pressure. The calibration can also change as the filament wears with time. 'Poisoning' of the filament surface by chemical reactions and by adsorption of gases can change the work function of the filament and can change the emission current [43].

2. X-rays are produced when the electrons hit the grid. These x-rays can strike the ion collector and cause electrons to be liberated from the collector. This is indistinguishable from an ion current and is not related to the presence of gas being measured. This places a limit (called the 'X-ray limit') on the lowest pressure that can be read reliably. The ion collector is made to be a very thin wire so as to minimize this effect by intercepting as little x-rays as possible.

3. The gauge changes the local pressure in which it is in by ionizing the gas being measured and by heat-induced outgassing of the gauge components, especially the filament and the surrounding structures. Chemical reaction of the gauge components with the gas being measured can occur [43]. The electron emission current is kept low in an effort to minimize these effects.

The ion gauge installed on our system is the Granville-Phillips Series 370 Stabil-Ion Gauge with Yttria-coated Iridium filaments. The measurement range is 2×10^{-11} to 5×10^{-4} Torr. The x-ray limit is 2×10^{-11} Torr so measurements near this limit will not be repeatable [44]. The quoted accuracy for N_2 is $\pm 4\%$ of the reading from 1×10^{-8} to 1×10^{-4} Torr. The quoted repeatability is $\pm 3\%$ of the reading from 1×10^{-8} to 1×10^{-4} Torr [45].

4.1.4 Residual gas analyzer

Similar to an ion gauge, a residual gas analyzer (RGA) uses an electron beam to ionize gases present. A quadrupole RGA in addition uses an arrangement of electric fields to select which charge to mass ratio of ions will be detected. In this way by sweeping over different charge to mass ratios to be detected the RGA provides information on the composition of the gas being measured and the relative amount of different gas species. Residual gas analyzers are most easily used for qualitative detection of the presence of various species in the vacuum system. For quantitative work they must be calibrated for the species that is to be measured. The RGA on our system is the QMG220 M2 PrismaPlus from Pfeiffer Vacuum (part number PTM06241213) which has a minimum detection limit less than 2×10^{-12} mbar and a mass range of 1-200 amu [46].

4.1.5 Pirani gauge

In a pirani gauge changes in resistance of a heated wire with pressure are detected. One of these gauges (a 'convectron' gauge accompanying the 370 Stabil-Ion gauge, part number 275256 and 275196) is installed on our system to detect failures in the turbo and scroll pumps. The pressure range they read is in the 1×10^{-4} to 1000 Torr range.

4.2 Existing pressure standards

This section outlines some of the existing pressure standards that are used to calibrate gauges in the high and ultra-high vacuum pressure range.

4.2.1 Static expansion method

In the static expansion method [47] the pressure in a chamber of known volume, V_1, is measured at a pressure P_1. The pressure P_1 is high enough

that it can be accurately measured with a gauge calibrated on a high pressure standard (such as a mercury manometer). The gas is then expanded into volume V_1 and V_2 so that $P_1V_1 = P_2(V_1 + V_2)$ where P_2 is the pressure after expansion. Provided that the volumes V_1 and V_2 are accurately known and P_1 is accurately measured then P_2 can be determined. A gauge connected to the volume V_1 or V_2 can be calibrated at lower pressures than the gauge that was used to measure P_1. This could also be used to extend the calibration range of the gauge that measured P_1. The static expansion method typically is used as a standard down to 10^{-5} Pa, though it can be extended for inert gases down to 10^{-7} Pa [48]. The lower pressure limit is mainly determined by the outgassing from the vacuum chamber.

4.2.2 Orifice Flow method

For calibration of gauges at a pressure range of (10^{-1} to 10^{-10} Pa) orifice-flow standards (also known as dynamic expansion methods) are used [33, 47, 49–51]. The typical setup of the orifice flow method is shown in Fig. 4.6. Two chambers are separated by an orifice with gas being fed into chamber 1 and pumped out at chamber 2. The flow of gas through the orifice can be characterized by the 'throughput'. Throughput, Q, also sometimes called flow or flow rate, of gas into/out of a volume V with pressure P is defined as $Q = \frac{d(PV)}{dt}$. For the ideal gas law $PV = nRT$ and

$$Q = \frac{d(PV)}{dt} = RT\frac{dn}{dt} \tag{4.1}$$

so that throughput is proportional to the rate or molar increase/decrease in the volume V. Throughput has units of $\frac{\text{Pa}\cdot\text{m}^3}{\text{s}}$. The molar rate of change $\frac{dn}{dt}$ is also commonly called flow or flow rate and has units of mol/s. Through the orifice there will be a throughput of

$$Q = C(P_1 - P_2) \tag{4.2}$$

where P_1 and P_2 are the pressures in chamber 1 and 2 respectively. The conductance C depends on the dimensions of the orifice, and the gas type and temperature [40, 41]. The conductance is independent of pressure for sufficiently low pressures (i.e < 100 Pa) [52]. Chamber 1 in Fig. 4.6 has a net throughput of zero and its pressure, P_1, is in steady state.

In the schematic of an orifice flow standard shown in Fig. 4.6 two gauges are installed at the upper chamber. One of the gauges (G_a) is calibrated on another standard in some pressure range, and another gauge (G_b) is to be

calibrated at a lower pressure range than G_a. Dividing Eq.4.2 above by P_1 we have

$$\frac{Q}{P_1} = C(1-r) \tag{4.3}$$

where $r = P_2/P_1$. In the molecular flow regime (where the gas atoms or molecules hit the walls before hitting each other) the ratio r is a constant at different flow rates, Q. The ratio r can be determined by generating a large flow so that the pressure, P_1, in chamber 1 is high enough that it can be measured with gauge G_a. Gauge G_a is typically a spinning rotary gauge. In addition, throughput Q is measured with a flowmeter so that the ratio r can be solved from Eq. 4.3 with a known conductance.

To calibrate the gauge G_b in Fig. 4.6, the flow can then be cut back so that the pressure P_1 is below the measuring range of the calibrated gauge G_a. With measured Q, r, and known C, the pressure P_1 can be determined from Eq. 4.3.

Various flowmeters exist but a popular choice is the constant pressure flowmeter described by [53, 54]. For a constant pressure flowmeter the volume of a gas filled region is changed at a constant rate, $\frac{dV}{dt}$, driving gas out of the volume through a leak valve. The pressure, P, is kept constant in the volume and is measured by a calibrated pressure gauge. With the pressure, the rate of volume change, and the temperature T, the molar flow rate $\frac{dn}{dt}$ is given as

$$Q = P\frac{dV}{dt} = \frac{dn}{dt}RT. \tag{4.4}$$

The conductance of an orifice can be measured using a constant pressure flow meter. The orifice is used as the outlet for the flowmeter instead of a leak valve [54]. The basic idea is that for a known flow Q produced by the flowmeter, a known pressure P inside the flowmeter, and a small pressure on the output side of the orifice, the conductance C of the orifice is given as $C = Q/P$.

A separated flow method can also be used to extend the range of a flowmeter [49, 52]. A known throughput Q from a flowmeter is put into a volume with two orifices. The flow through the orifice of conductance C_1 will be $Q_1 = Q\frac{C_1}{C_1+C_2}$. The flow through the orifice of conductance C_2 will similarly be $Q_2 = Q\frac{C_2}{C_1+C_2}$. Eq. 4.3 gives that smaller known flows enables calibration of smaller pressures P_1.

4.3 A proposed density/pressure standard using trapped atoms

It is proposed that measurement of background gas collisions can be used as a standard for the density of a given background gas surrounding a cloud of trapped atoms. Assume for the moment that there is only one background species, for example ^{40}Ar, and that the trapped species is ^{87}Rb. The principle is to determine the density of ^{40}Ar from measurement of the loss rate constant due to background collisions, Γ. From Eq. 2.1 the loss rate constant can be expressed as

$$\Gamma = n_{\mathrm{Ar}} \langle \sigma v_{\mathrm{Ar}} \rangle_{^{87}\mathrm{Rb},^{40}\mathrm{Ar}} \tag{4.5}$$

The velocity averaged collision cross section for loss $\langle \sigma v_{\mathrm{Ar}} \rangle_{^{87}\mathrm{Rb},^{40}\mathrm{Ar}}$ was described in Chapter 2. The proposed density measurement is to measure Γ for ^{87}Rb atoms trapped in a magnetic trap and to solve for n_{Ar} with known $\langle \sigma v_{\mathrm{Ar}} \rangle_{^{87}\mathrm{Rb},^{40}\mathrm{Ar}}$ for a trap depth of the magnetic trap. In this manner ultracold atoms would provide a primary standard for density/pressure because it is not reliant on any other density/pressure measurement. This proposal is not restricted to our particular choice of trapped atom or background gas.

A decay time constant of 0.01 to 100 s, corresponding to a loss rate constant, Γ, of 100 to 0.01 s^{-1}, corresponds to a pressure measurement range of 10^{-6} to 10^{-10} Torr. It is within vacuum technology to achieve ultimate background pressures order of magnitudes lower than this pressure range so that the assumption that ^{40}Ar, for example, could be taken as the dominant species is reasonable.

The proposed method potentially also allows density measurement of multiple species in the background (i.e. differential pressure measurement), provided that what those species are is known. Suppose the background composition is known to contain N different background species. The loss rate Γ will have a contribution from each of these species

$$\Gamma = \sum_{i=1}^{N} n_i \langle \sigma_{\mathrm{loss}} v_i \rangle_{X,i}. \tag{4.6}$$

The loss cross section depends on trap depth. Measurements of Γ could be taken at N different trap depths and the values of $\langle \sigma v_i \rangle_{X,i}$ at each trap depth determined. Eq. A.14 then gives N equations and N unknowns and the densities $n_1 ... n_N$ can be solved for.

It is hoped that the method of density measurement using trapped atoms could serve as a primary pressure standard. Currently the pressure stan-

dards for the UHV pressure range rely on measurements using gauges calibrated at higher pressures. The proposed method has the possibility of not having to use calibrated gauges, for example for Ar, where calculation of the velocity averaged collision for loss has had some success. [1, 14, 17].

There is still merit to the proposed method even if it is not desired or difficult to calculate the velocity averaged collision cross section for loss between the trapped atom species and the background gas species chosen. If a gauge that is calibrated can be used to measure the density of a particular background gas, for example Ar, then the loss rate constant , Γ, for trapped atoms can be measured as a function of the density of Ar. As seen in subsection 3.2.3 The slope of the plot of Γ versus n_{Ar} yields $\langle \sigma v_{\mathrm{Ar}} \rangle_{^{87}\mathrm{Rb},^{40}\mathrm{Ar}}$. The advantage of using trapped atoms in this case is that once $\langle \sigma v_{\mathrm{Ar}} \rangle_{^{87}\mathrm{Rb},^{40}\mathrm{Ar}}$ is known for a given trap depth it does not change and is the same in all laboratories using the same trap depth and trap. This means that a continual up keep of calibrated gauges for the standard would not be necessary.

As a first test of the atom trap standard the density measurements of a test gas such as Ar given by the atom trap will be compared to commercial gauges with calibration traceable to national laboratories. NIST is also planning on sending an ionization gauge and two spinning rotary gauges calibrated on their orifice flow standard.

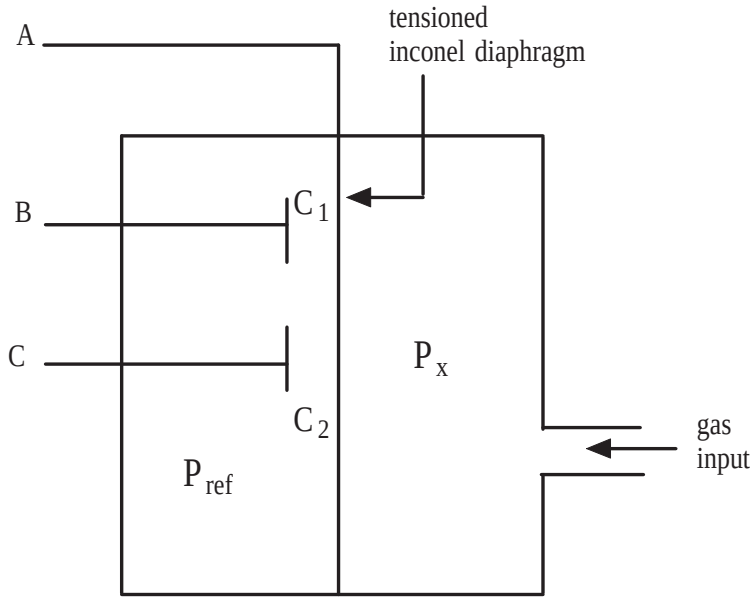

Figure 4.2: A capacitance diaphragm gauge (CDG) consists of an enclosure divided into two sections by a thin metal sheet called the diaphragm. The diaphragm is typically inconel, an alloy of predominantly nickel and chromium. For absolute pressure measurement one side of the enclosure is evacuated to a very small pressure so that $P_{ref} \approx 0$. The other side of the diaphragm will be deflected according to the pressure P_x to be measured. At different positions of the diaphragm the capacitance C_1 and C_2 formed between the diaphragm and electrodes will change. These capacitances (C_1 and C_2) are fed into an AC bridge (see Fig. 4.3) and the voltage V across the bridge related to the pressure P_x.

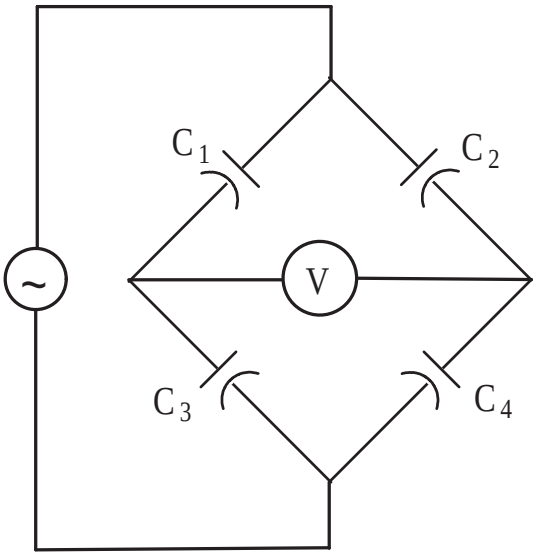

Figure 4.3: An AC bridge. The voltage, V, across the bridge is zero if the impedances satisfy $Z_1/Z_3 = Z_2/Z_4$.

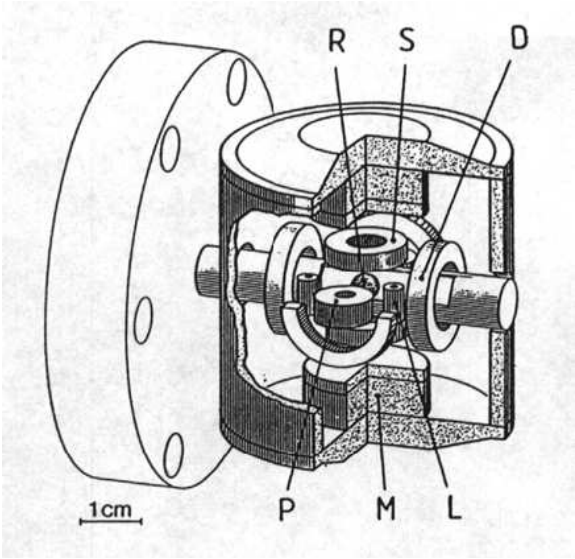

Figure 4.4: A schematic of a spinning rotary gauge. Two permanent magnets (M) are used to levitate a stainless steel ball (R). Four drive coils (D) are used to spin the ball (R) at a certain angular frequency. Vertical deviations of the ball are suppressed by two stabilization coils (S) and horizontal deviations are suppressed by four coils (L). Pickup coils (P) are used to sense the angular frequency of the ball and the rate of angular deceleration when the ball is allowed to spin without being driven in the presence of gas. From the rate of angular deceleration the pressure of the gas can be determined. The ball resides in a steel tube connected to the vacuum apparatus while the magnets and coil assembly slide over the tube external to the vacuum.

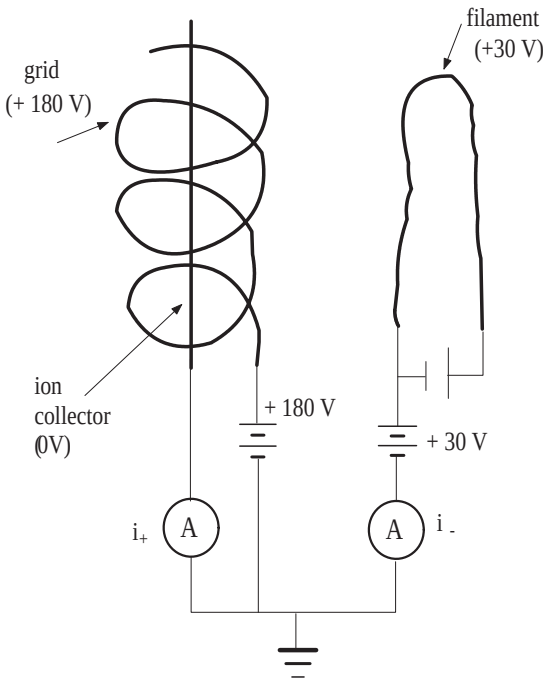

Figure 4.5: A schematic of an ion gauge. A filament (typically tungsten or yttria-coated iridium) is heated and electrons released. The electrons travel trajectories towards the positively charged grid. Ions that are formed from collision of the electrons with the gas present will travel towards the ion collector and a current will be detected on the ion collector (i_+). The pressure, P of the gas being measured is proportional to the ratio of the ion collector current and the electron emission current (i_-) so that $P = \frac{i_+}{i_-}$.

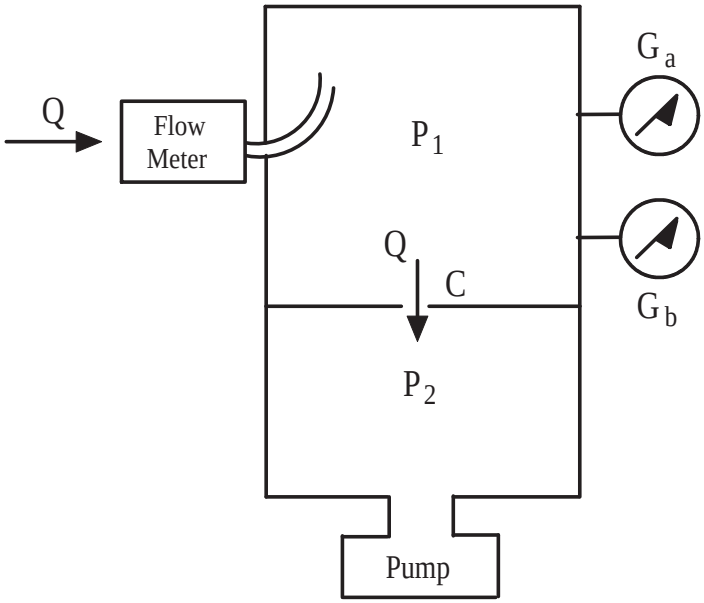

Figure 4.6: Two chambers are separated by an orifice of known conductance C. The throughput through the orifice is $Q = C(P_1 - P_2)$. This throughput will be the same as the throughput input to chamber 1 providing the pressure P_1 in the upper chamber is in steady state and outgassing is negligible. Two gauges are connected to the upper chamber. Gauge A (G_A) is calibrated on another higher pressure range standard. Gauge B (G_B) is the gauge that is to be calibrated by the orifice flow standard. Q is measured with a flowmeter and C is either independently measured or calculated. The ratio $r = P_1/P_2$ is determined by sending a large enough throughput through the system so that gauge A can measure P_1. The flow is then cut back to a pressure P_1 at which one wishes to calibrate gauge B. The ratio r is constant within the molecular flow regime so that the pressure P_1 in the upper chamber can be determined from Q, C and r.

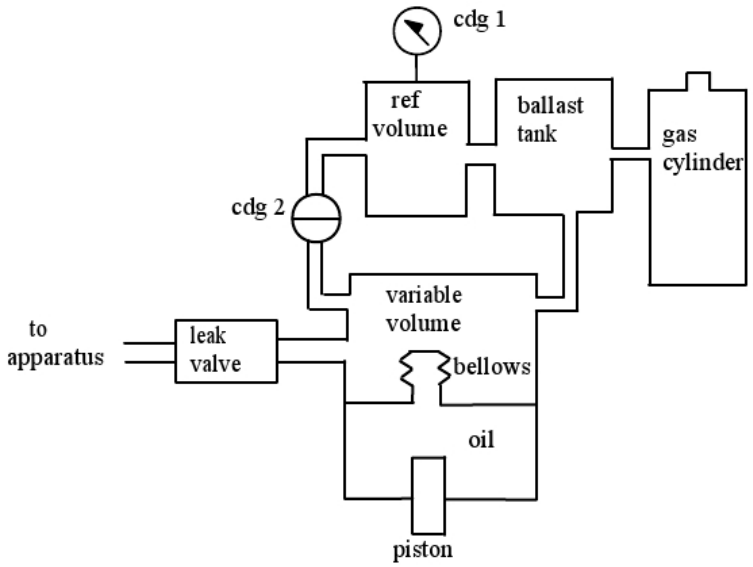

Figure 4.7: A constant pressure flowmeter used to generate a known flowrate. The volume of a chamber is changed steadily while the pressure is kept constant with respect to a reference chamber allowing a precise determination of flowrate out of the chamber.

Chapter 5

Experimental Apparatus for the Pressure Sensor Experiment

This chapter provides details on the design and construction of the experimental apparatus for taking pressure measurements using trapped atoms. A solidworks drawing of the vacuum apparatus is given in Fig. 5.1. Fig. 5.2 shows the same apparatus from a different point of view. Vacuum created in the system starts with the high-vacuum (HV) pump region of the apparatus consisting of scroll and turbo pumps. The 2D MOT section consists of a chamber with viewports for the 2D MOT light to enter. A Rb source is also attached to the 2D MOT chamber to load the 2D MOT from Rb vapour. The 2D MOT section is connected to the 3D MOT section through a series of tubes used for differential pumping. The 2D MOT provides an atomic beam of ^{85}Rb or ^{87}Rb atoms to the 3D MOT section. The 3D MOT section consists of a glass cell for input of laser beams and surrounding magnetic coils to create a 3D MOT and a magnetic trap. The 3D MOT cell has ultra-high vacuum (UHV) pumps attached to it to maintain low pressures (i.e. in the 10^{-11} Torr range). Diagnostics (pressure gauges) are also attached to the 3D MOT cell to compare pressure measurements of commercial gauges with measurements taken using trapped atoms. Below the 2D MOT section is a leak valve to input gases whose pressures are to be measured. This chapter will provide more detail on all of these different sections of the experimental apparatus. Not shown in Fig. 5.1 and Fig. 5.2 are the optics to generate the 2D and 3D MOT light. These optics will also be discussed in this chapter.

Several features of our apparatus that are not common in experiments involving ultra cold atoms are the presence of a leak valve to introduce background gas, the design of our differential pumping system, and the numerous pressure gauges installed on our apparatus.

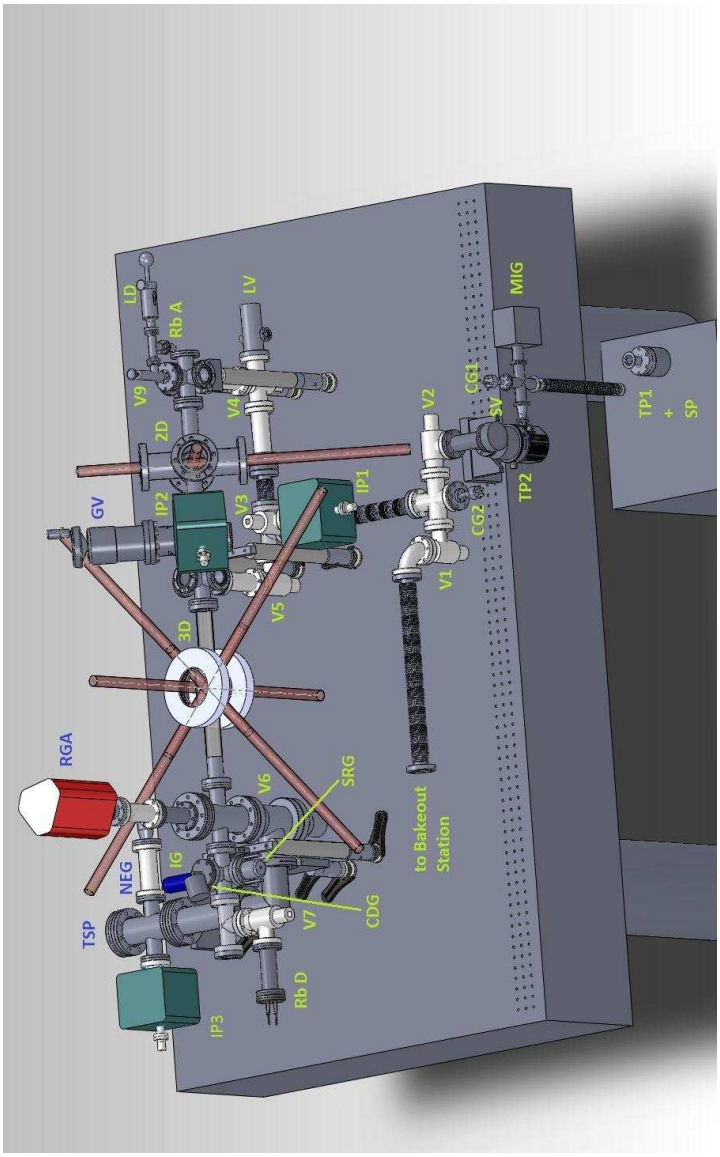

Figure 5.1: The vacuum apparatus for the pressure sensor experiment. SP: scroll pump, TP1, TP2: turbo pumps, MIG: mini ion gauge, CG: convectron gauge, SV: solenoid valve, V1-V8: all metal valves, IP1-IP3: ion pumps, LV: leak valve, LD: linear drive mechanism, RbA: rubidium ampoule, 2D: 2D MOT chamber, GV: gate valve, 3D: 3D cell, RGA: residual gas analyzer, CDG: capacitance diaphragm gauge, SRG: spinning rotary gauge, IG: ion gauge, RbD: rubidium dispensers, TSP: titanium-sublimation pump, NEG, non-evaporable getter.

Figure 5.2: Another perspective of the vacuum apparatus for the pressure sensor experiment. The apparatus consists of different main sections. At the 2D MOT section a 2D MOT is created to form an atomic beam to load a 3D MOT. A Rb source is connected to the 2D MOT region to load the 2D MOT from Rb vapour. The 3D MOT section consists of a glass cell. UHV pumps are used to maintain ultra-high vacuum pressure in the 3D MOT cell. Pressure gauges are attached to the 3D MOT cell to provide measurements of pressure to compare to the pressure measurements taken with trapped atoms.

Throughout this chapter any abbreviated labelling refers to Fig. 5.1 unless otherwise noted.

5.1 High Vacuum Pumps

Our experiment uses a variety of vacuum pumps to establish ultra-high vacuum (UHV) in our apparatus (pressures $< 10^{-8}$ Torr). Starting from atmospheric pressure we pump with a scroll pump (SH-110, Agilent) labelled SP. The scroll pump has two circular mechanisms that move with respect to each other and compress gas that enters the mechanism towards an exhaust output. The scroll pump has a specified base pressure of 5×10^{-2} Torr [55]. The measured base pressure with an eyesys mini-BA ion gauge from Varian connected to the scroll pump and nothing else was 3.6×10^{-2} Torr. Note often Pa are used for pressure instead of Torr (1 Torr = 133.3 Pa).

To get lower in pressure we attach a turbomolecular pump (TV 70 , Agilent) labelled TP to the scroll pump. Turbomolecular pumps have a series of blades which are angled. When spinning the blades impart momentum to molecules that hit the blades towards another set of blades etc. until they makes their way to the exhaust which is pumped away by the scroll pump. The specified base pressure of the turbo pump is 3.8×10^{-10} Torr.

During initial evacuation and while baking we attached to the vacuum system the 'bakeout station' described in sec. 3.1 which contains another scroll (SH-100, Agilent) and turbo pump (TV 70, Agilent). During initial pump down and baking the turbo and scroll pumps are the only pumps operating since the other pumps in the apparatus operate in the UHV regime and need 'cleaning' by baking.

An electromagnetic solenoid valve labelled SV (SA0150EVCF, Kurt Lesker) was placed after the turbo pump in the high-vacuum pump region in case of a power failure to prevent air leaking into the vacuum chamber through the pumps. Two manual all metal valves, V1 and V2 (9515027, Agilent) can be used to valve off the HV pumps when not in use and for removal or repair of the pumps.

The high vacuum pumps are connected to the main apparatus by a bellows. This bellows connects to ion pump IP1 (9191145, Agilent) through all metal valve V3 (9515027, Agilent). This bellows is also attached by a tee to all metal valve V4 and V5. Valve V4 (9515017, Agilent) connects the high vacuum pumps to the 2D MOT chamber portion up above. Valve V5 (9515027, Agilent) connects the 3D MOT and UHV pump region of the apparatus to the high vacuum pumps and to the leak valve LV (9515106,

Agilent). A convectron gauge (labelled CG) is present after valves V1 and V2 but can only read down to 10^{-4} torr.

The base pressure achieved by the high vacuum pumps measured by a mini-ion gauge (eyesys mini-BA, Varian) is around 8×10^{-9} Torr. This is after some mild baking (up to 110 deg C) using heater tape from the turbo pump to the solenoid valve. Earlier implementations of the connections from the turbo pump to the SV valve used NW 25 KF connections which limited the base pressure to the 10^{-6} torr range. The electromagnetic solenoid valve (SV) has a fluorocarbon seal which causes the pressure to rise when it is on because it heats up and outgasses more. Keeping the valve cool with a fan while on has reduced that effect.

5.2 2D MOT Section

A 2D MOT is formed from two orthogonal pairs of counterpropagating laser beams travelling along, for example, the $\pm y$ and $\pm z$ directions. In addition, magnetic field gradients along those directions are needed, and also appropriate right or left circular polarization choices for the light. There are no trapping laser beams along the x direction and the field gradient along the x direction is small compared with the y and z direction. This means atoms entering the intersection of the trapping laser beams from a background vapour will have their y and z velocity components decreased in magnitude but not their x velocity component. As a result an atomic beam will form exiting the trapping region (the intersection of the laser beams) along the $\pm x$ axis. This atomic beam travels through small tubes connected to the section of the vacuum apparatus where the coils and optics for the 3D MOT reside. A 'push' laser beam is sent through the 2D MOT to push atoms in the positive x direction towards the tubes. The small tubes provides differential pumping where the pressure on the 2D MOT side of the tubes can be high (e.g. 10^{-7} Torr) and on the 3D MOT side it can be low (e.g. 10^{-10} Torr). The tubes also act as a speed filter so that the speed distribution of the atomic beam travelling to the 3D MOT is significantly below the speed distribution expected from a thermal gas. The 2D MOT is loaded from Rb vapour which is on the order of 10^{-7} Torr. An advantage of loading a 3D MOT from a 2D MOT is that the 3D MOT vacuum region can be orders of magnitude lower in pressure. For our case this is important since we want the residual background pressure that the pressure measurements are performed in to be as low as possible while still maintaining a sizeable 3D MOT.

5.2.1 2D MOT chamber region

The 2D MOT chamber (labelled 2D in Fig. 5.1 and also shown in Fig. 5.3) was custom built (Johnsen Ultravac) with seven ports. Four of these ports form a four way cross with 4.5 inch CF viewports for light to enter for the 2D MOT. One port along the atomic beam axis is connected to a six way cross (shown in Fig. 5.2). This six way cross connects to the Rb source through valve V8 (9515014, Agilent). The Rb source consists of a glass ampoule with 1g of Rb (K4584x from ESPI metals). This ampoule has a custom made holder (Johnsen Ultravac). A linear drive mechanism LD (KLPDAA, Kurt Lesker) was installed for the purpose of breaking open the ampoule after baking. The six way cross also connects to the HV pumps when valve V4 is open. Three viewports are installed on the six way cross for looking for Rb fluorescence when filling the chamber with Rb, for viewing the 2D MOT down the atomic beam axis, and for sending in the push beam mentioned above.

The port of the 2D MOT chamber in line with the beam axis, and closest to the 3D MOT section, contains a differential pumping section vacuum-welded into the port. Fig. 5.4 shows a cut away of the differential pumping section of the chamber. The first tube in the differential pumping design separates the 2D MOT chamber where the Rb vapour resides from an ion pump (IP2 9191145, Agilent). A second tube then connects the region with the ion pump to the 3D MOT side of the apparatus. The second tube has a graduated opening to allow for divergence in the atomic beam as it propagates towards the 3D MOT. Having the ion pump separated from the Rb vapour helps to preserve the lifetime of the ion pump. The two tubes are lined up along the x direction. Atoms from the 2D MOT propagate primarily along the x direction and will make it through both tubes. Atoms that randomly make their way into the tubes will tend not to be travelling with such high x directionality and will bounce around in the region between the two tubes until they are removed by the ion pump. The distance from the entrance of the differential pumping tube in the 2D MOT chamber to the center of the cell at the 3D MOT region is approximately 55 cm. Dimensions of the differential pumping tube are included in appendix **??**.

The design of the 2D MOT chamber as well as preliminary design of the vacuum apparatus is credited to Ian Moult, Weiqi Wang, and Haotian Pang. The mechanical drawings for the 2D MOT chamber and the Rb ampoule holder, as well as differential pumping analysis are found in their report [56].

5.2.2 2D MOT coils

Figure 5.5 shows a picture of the 2D MOT coils installed on the 2D MOT chamber. Four rectangular coils are used to produce a magnetic field gradient along the two perpendicular arms of the large four way cross of the 2D MOT chamber. Each coil is parallel to the viewport it fits around. The inside dimensions of each coils is 8 by 26 cm. The coil pair surrounding the viewports in the y direction is separated by 8.5 cm and the pair surrounding the viewports in the z direction is separated by 14 cm. There are approximately 10 layers with 12 turns per layer totalling 120 turns. The wire used was 16 AWG magnet wire from Superior Essex (H GP/MR-200). The gradient with 5A going through all the coils was measured using a gaussmeter (model Bell 620) to be 16.6 G/cm along the transverse direction and 0.29 G/cm along the axial direction.

The inner width of the coils was less than the width of the viewports they slip over. For this reason the 2D MOT rectangular coils were wound on a separable frame (Fig. 5.6) that could be used to wind the coils and then could come away from the coils leaving just the coil. The design and manufacture of this frame as well as initial simulations of the 2D MOT coils is credited to Kousha Talebian. Electrical tape was placed on the frame surface to prevent the wire from scratching on the frame when winding. This could lead to the removal of the insulating layer on the wires and shorting them out. The coils were wound by hand with feet placed on a rod going through the wire spool providing tension. The start of the first winding is secured so that the wire doesn't move around too much when the coil winding is getting started.

The coil shape once separated from the frame is maintained by wrapping around the coil cross section in a few positions either with high temperature kapton tape or with wire. The coils with slight deformation were slipped over the viewports of the four way cross of the 2D MOT chamber. Plastic wrap is placed over the viewports and over the bolts securing the viewports to the 2D MOT chamber when putting on the coils to prevent either the coils or the viewports from being scratched.

One of the coils needed to be mounted before the ion pump used for the differential pumping in the 2D MOT chamber could be installed. This coil can not be removed and was present during baking. The three others coils were not present during baking and are removable. The magnet wire used for the coils has an insulating layer of polyester/polyamideimide (which is not kapton). This coating has a limited lifetime above 215°C. For future reference this wire should not be used on a system where the wire needs

to be baked. The wire was tested at 220°C and turns a deep colour but otherwise seemed to be okay. After baking for a long period of time at 180°C and then cooling down to room temperature cracks formed at stress points so that extreme care should be taken in handling these coils so that the coating is not rubbed off causing shorts.

5.3 3D MOT section

The 2D MOT chamber is separated from the 3D MOT section by a gate valve (48132-CE01-0002, VAT valve). After the gate valve is a six-way cross with viewports for diagnosing the 2D MOT beam characteristics exiting the differential pumping tubes. The six way cross connects to an ion pump, leak valve and turbo and scroll pumps through valve V5 in Fig. 5.1. This six way cross is also attached to a glass cell into which laser beams for the 3D MOT are sent. This glass cell is rectangular in shape where the laser beam enter. The cross section of the cell is square with inner dimensions of 40 mm by 40 mm. Magnetic coils are also needed for the 3D MOT which are representatively shown in Fig. 5.1 and Fig. 5.2.

5.4 UHV pumps and diagnostics

Several gauges are attached to the UHV region (the part numbers and specifications are given in chapter 4). A capacitance diaphragm gauge (labelled CDG in Fig. 5.1) is installed to calibrate a spinning rotary gauge, which in turn will be used to calibrate an ion gauge. Pressure measurements with the ion gauge (IG) will be compared with the measurements provided by trapped atoms. A residual gas analyzer (RGA) is also installed for analysis of the different species present in the background and for comparative differential pressure measurements.

The UHV section has a titanium sublimation pump attached to it (labelled TSP, 916-0050, Agilent). A non-evaporable getter pump (NEG, C 400-2-DSK ,SAES getters) and an ion pump (IP3, VacIon Plus 20, 9191145, Agilent) are also attached to achieve a low background pressure. These pumps are behind a valve (V6, VZCR60R, Kurt Lesker) so that they can be isolated from the 3D MOT region during any pressure measurements to reduce pressure gradients and to protect the pumps. An elbow is installed between the valve V6 and the TSP, NEG, and IP3, to prevent Titanium from the Ti-sub pump coating the valve which will be exposed to the 3D

MOT cell when the valve is closed. A more detailed description of these pumps is given in the next section.

Part of the 3D MOT section is also a connection to Rb dispensers (Rb D, AS-3-Rb-50-V , Alvatec) which can be valved off with valve V7 (9515027, Agilent) if not needed. These were installed for trouble shooting purposes in case a 3D MOT could not be achieved easily at first using the 2D MOT.

The titanium sublimation pump and the non-evaporable getter in our system work by chemisorption [40]. Chemisorption is when a material (titanium or Zr V Fe in the case of our NEG) has a high binding energy for active gases such as O_2, N_2, CO_2 and H_2 so that these gases adhere to the material. The titanium sublimation pump shown in Fig. 5.7 consists of titanium filaments that are heated. At a sufficiently high temperature the titanium evaporates forming a film on the surrounding walls of the chamber which can then pump gases from the system. The titanium is evaporated at intervals forming a fresh layer and trapped material adsorbed onto previous layers.

Our non-evaporable getter is ZrVFe arranged in disks to have a large surface area. The getter is only activated occasionally by heating so that the external monolayer of gases adhering to the surface moves within the getter material allowing a fresh surface for continued pumping. The getter is then cooled because the lower the temperature of the getter, the lower the base pressure of H_2 realized in the system. About 90-100 activations can be performed, with the time between activations depending on the gas input to the system, how often the system is baked, and how often it is vented to atmosphere. The getter is reaching its end of use when the hydrogen pressure slowly rises and re-activation leads to a baseline hydrogen pressure that is higher than for previous re-activations. The getter pumps hydrogen and active gases well however the getter pumps do not pump inert gases. These pumps are typically used to achieve and maintain UHV but can only be activated once a sufficiently low pressure has already been achieved by other pumps such as the scroll, ion, and turbo pumps.

Ion pumps (VacIon Plus 20, 9191145, Agilent) are placed in several locations of our apparatus. Ion pumps have an ultimate pressure of less than 10^{-11} Torr and should not be turned on above 10^{-3} Torr. In ion pumps electrons are discharged from cathodes towards an anode. Magnetic fields are used to maximize the electron trajectory length by producing spiral trajectories. During its trajectory an electron can ionize gases found in the system creating positive ions which are then accelerated towards a negatively charged cathode. This cathode is typically made of titanium so that the ions react with the titanium and are removed from the system. Also neu-

tral gases can react with the titanium as in a titanium sublimation pump. When the ions hit the cathode they have sufficient energy to knock out or 'sputter' titanium from the cathode which coats surfaces with fresh titanium [40, 41]. Ionized noble gases can be pumped by accelerating towards the cathode and being buried within the cathode material. They are further buried by incoming sputtered cathode material.

5.5 Vacuum apparatus assembly

This section describes the assembly steps of the vacuum apparatus. The vacuum apparatus was assembled from the 2D MOT side towards the 3D MOT side. All the standard stainless steel vacuum components were assembled first, except for the gauges, pumps, and Rb sources. Mounts for 2.5 inch ConFlat (CF) flanges and 4.5 inch CF flanges were machined and mounted on 1.5 inch diameter posts to hold up the vacuum apparatus. The CF flanges are secured to the mounts using hose clamps that are cut and screwed to the mounts. The height from the optical table top to the center of the cell where the atoms are trapped in the 3D MOT is 17.5 inches.

Each piece used for ultra-high vacuum has one or multiple CF flanges to connect to other pieces. This CF flange consists of a sharp knife edge which cuts into a copper gasket placed between two CF flanges when they are bolted and tightened together. If the connection is ever taken apart (vacuum is broken) then a new gasket must be used. Scratches in the gaskets can prevent proper sealing. It is sometimes hard to hold the gasket in place while holding pieces together and putting in screws and bolts. A helpful suggestion from a labmate was to put kapton tape on the edges of the copper gasket to secure it to the conflat flange while connecting flanges. This prevents the gasket from falling out while tightening the bolts. The tape is removed after the flanges and bolts have been finger-tightened together. The flange bolts are tightened in opposing pairs to maintain uniform cutting of the flanges into the gasket. The bolts are tightened until sliver of copper gasket can still be seen so that, in the case of a leak, the bolts can be further tightened and to allow for expansion when baking. Wherever possible silver bolts (eg. TBS25028125P from Kurt Lesker) to prevent seizing after baking. Otherwise an anti-seize compound (VZTL from Kurt Lesker) can be used but care should be taken not to introduce the compound to the vacuum side of the flanges.

All CF connections on the tee and valve V8 that are attached to the Rb ampoule RbA have Ni annealed gaskets (GA-0275NIA and GA-0133NIA,

Kurt Lesker) since this region comes in the highest contact with Rb. The viewports on the apparatus have annealed copper gaskets (VZCUA38 and VZCUA64, Kurt Lesker) rather than regular copper gaskets to put less stress on the viewport which reduces the chance of the viewports developing a leak.

No precleaning of vacuum parts was used (they are precleaned from the factory). Gloves were used at all times and changed frequently. Care was taken not to talk or breathe into the vacuum apparatus. The bellows on the Rb cell was scrubbed with a bottle washer with alconox, sonicated in alconox for 1 hr, then in distilled water, then in acetone and then in methanol. The bellows side of the cell was attached to the 2D MOT side of the apparatus to strain relieve the connection of the cell to the 2D MOT region while all the components on the other side of the cell were being added. The compensation coils shown in Fig. 5.12 that surrounded the cell were put in at this stage.

Another part that had to be cleaned was the electrical feedthrough which was machined (cut down and holes inserted) so that the Rb dispenser tabs could be put through. The feedthrough was cleaned with methanol sonication after machining. The NEG holder was also sonicated in methanol. Both the NEG holder and the feedthrough have ceramic parts deeper inside the pieces and it is recommended not to get these wet with methonal or other solvents since the ceramic will absorb it and outgas later under vacuum.

The apparatus was leak-tested periodically as it was being built by blanking off all openings and pumping down using our bakeout station. The residual gas analyzer on the bakeout station described in section 4.1 was used to detect any He entering the system. Once the main vacuum apparatus frame was in place, the Ti-sub was installed.

The ion pumps were installed next with the magnets left on. The 2D MOT coil which wraps around the ion pump port on the 2D MOT chamber was installed prior to connecting the ion pump. The ion pumps are shipped under vacuum, sealed off with a CF flange. This flange has a bolt hole in it into which one can insert a bolt and use the bolt to remove the flange, which is held tightly onto the pump due to the low pressure inside and the high pressure outside. The ion pumps were installed with their bakeable cables attached since the ion pumps needed to be turned on towards the end of the baking phase (described in the next section). The optical table surface is grounded using a metal braid attached to grounded electrical piping in the lab. This provides grounding to the vacuum apparatus through the mounts holding the vacuum apparatus up.

Gauges were installed as per the manuals consisting mostly of routine connections of CF flanges. The spinning rotary gauge was installed using a

level since the axis of the measurement head needs to be vertical within $\pm 1^\circ$. After the gauges were installed two Rb dispensers were installed. Finally the NEG was installed. It was clear that the standard 2.75 inch CF nipple was too small in diameter as the NEG scrapes the walls. If vacuum is ever broken, it is recommended to buy and install the manufacturer designed pump body for the NEG or to install the NEG in a larger diameter flange so that the pumping capacity is not limited as it is now. Also the capacitance diaphragm gauge should be oriented so that the housing can come off and the cables removed. Consideration of putting on a valve on any of the gauges should be made in case one wants to disconnect them and send them away for calibration or repair. Also a valve should be installed where a calibrated comparison gauge could be added. Additional recommended changes include the installation of a cooling sleeve on the Ti-Sub (9190180, Agilent).

5.6 Bakeout

Baking out a vacuum apparatus involves heating the apparatus to high temperatures (above 100°C) to drive the water and other gases like H_2, CO_2, and O_2 off of the vacuum apparatus walls and to pump them away.

To bakeout the chamber an oven was formed right around the vacuum apparatus on the optical table (see Fig. 5.8). Firebricks (K23 Firebrick and 3 feet by 1 feet Fibre Block Insulation from Greenbarn Potters Supply) were used to form the oven. They were wrapped in aluminum foil to prevent the dust from the porous firebrick material from getting everywhere. Two layers of firebricks were put down on a layer of aluminum foil on the optical table around the base of the vacuum setup. A few bricks were cut to try to fill in gaps in this bottom layer and aluminum foil was scrunched up and put in to fill remaining gaps. Five infrared heaters (900 W Infrared Salamander heaters from Mor Electric Heating Assoc., Inc) powered individually by a variac were placed on this base layer of bricks at roughly equally spaced locations. Thermocouple gauges were also placed at various positions of the chamber to monitor the temperature while baking out. The thermocouple gauges were assembled from Newark part numbers (93F9305, 93F9313, 50B5932, 93B0462). The firebricks have dimensions of roughly 9" by 4.5" by 2" and the overall dimensions of the oven was approximately 7 feet by 3 feet by 3 feet and required around 420 firebricks. The lid of the oven was made from 3 feet by 1 feet Fibre block insulation with double layers put on top.

Before any of the oven was formed we removed the wooden platform

above the optical table and the HEPA filter to reduce the amount of heat trapped, to protect the filter and to allow the oven to be built tall enough to surround the vacuum apparatus. In preparation for the bakeout aluminum foil was placed in thick layers around the viewports and cell to protect against temperature gradients and anything melting onto them. The plastic handles for the gate valve (labelled GV in Fig. 5.1), 4.5" CF valve (labelled V6) and the linear drive mechanism (labelled LD) were removed. The linear drive mechanism was locked so as not to break the Rb ampoule. Any electrical connections to the ion gauge, capacitance diaphragm gauge as well as the spinning rotary gauge measurement head were not installed prior to baking and must be removed for any future baking. Any stickers or plastic were also removed. The all metal valves as well as the gate valve were open fully. The leak valve (labelled LV) was kept closed.

Heater tapes powered by variacs were also used for heating the parts of the vacuum apparatus not contained in the oven such as the bellows connecting the apparatus to the bakeout station. The lab's 'bakeout station' consists of a scroll and turbo pump for pumping, an ion gauge to indicate the pressure, a residual gas analyzer, and a bank of inputs for thermocouple gauges. A labview program collects the temperature readings of the thermocouple gauges and the pressure from the ion gauge.

Before starting the bake we pumped on the vacuum apparatus using the bakeout station to a pressure of 7×10^{-8} Torr as read by the ion gauge on the bake out station. Initially we ran 30 A through each Ti-Sub filament just to test the Ti-Sub filament controller, the pressure rose to the high 10^{-4} Torr range and then decreased. The Ti-Sub filaments were then turned off. After pumping down to the 10^{-8} Torr range again the NEG was activated. To activate the NEG DC voltage was applied in steps of 1V/min up to 16V which is then left for 60 min. The heating curves provided by SAES getters give a getter temperature of 475°C at 16V. Again pressure in the range of 10^{-4} Torr is reached when the NEG is being heated due to outgassing. It was noted that when first applying voltage the current predicted through the NEG by SAES getters will be about a factor of two off of their provided curves. This is because the resistance of the NEG increases as it is being heated so that after waiting a while at a given voltage the current will match the measurements provided by SAES getters. While the NEG was at 16 V the TSP filaments were outgassed by running each in turn at 37 A for 1.5 min. Once the NEG was activated the voltage was brought down to 7V which corresponds to 250°C and was left at that voltage for the duration of the bakeout so that the NEG would be hotter than the rest of vacuum apparatus since the coldest spot in the apparatus is where outgassed material

preferentially sticks. The TSP controller can only send current through one of the three filaments at a time, so for the remainder of the bake out we cycled from filament to filament running 30A continuously through them. When changing from one filament to another pressure increase by about 10 times and then decreases.

The actual baking started by increasing the voltage to the infrared heaters in 5V intervals waiting for the temperature inside given by the thermocouples to stabilize in between. The time to reach a steady temperature after each increase of variac voltage to the heaters was around 12 hours. When approaching the maximum care was taken not to overshoot the maximum temperature. We set a goal of 180°C in the oven since the RGA, linear drive mechanism to break the ampoule and the capacitance diaphragm gauge cables all have a maximum temperature of 200°C and we wanted to account for potential inaccuracies in thermocouple gauge measurement. At the bottom of the oven the temperature attained to was 157°C with temperature rising up to 185°C at the top of the 3D MOT cell and then decreasing to 179°C at the top of the RGA since this is close to the top cover of the oven where heat escapes. The hottest place in the oven was on top of the 4 way cross containing the NEG and Ti-Sub filaments at 200°C. This is because the NEG and Ti-Sub filaments were additionally being heated by running current through them.

The oven was brought up first in temperature with the outside bellows lagging behind in temperature so as not to outgas material from hot bellows into a colder main apparatus. Since the bakeout was low temperature compared to typical bakeout temperatures, we baked out for a longer time period of about 1 month. During bakeout the maximum pressure attained at maximum temperature was 2.2×10^{-6} Torr. While pumping it decreased to 2.5×10^{-7} Torr with both the bakeout station (one turbo, one scroll pump) and the main apparatus pumps (two turbo's and one scroll pump). We then ran each of the Ti-sub filaments at 40 A for 1.5 min, then went back to putting 30 A through one of the filaments.

At this stage we turned on the ion pumps and baked for another week. Though others [57] valve off their turbo pumps at this point we found that valving them off caused the pressure to rise 2 to 5 times and so we kept the turbo pumps and scroll pumps pumping on the system while the ion pumps were pumping. Cool down occurred slowly over the course of two days again cooling the bellows before the main chamber in a staggered fashion. When the experimental chamber was below 100°C. The NEG was reactivated at 16V for 60 min and then turned to zero and the current to the Ti-sub filament was shut off. The system then was allowed to completely cool down. When

cooled the ion gauge on the bake out station 'flat lined' at the lowest reading of 1.01×10^{-8} Torr. The ion current readout from the ion pumps which is proportional to the pressure in the system also indicated that when the turbos were valved off the current went down meaning that the ion pumps were doing a more effective job of pumping than the turbos and the scroll pumps. At this stage we closed valve V1 to the bakeout system and the solenoid valve SV to the high vacuum experimental pumps. 48 A was put through one of the Ti-sub filaments several times with a maximum duration of two minutes and a minimum of 30 seconds to sublimate the titanium and coat the surrounding chamber walls. Turning on the ion gauge in the experimental apparatus over the course of a day the pressure dropped to 1.7×10^{-10} Torr. The next step was to break the Rb ampoule and see if the system needed more baking due to the gases released in the ampoule.

5.7 Rb release from the ampoule

While baking the Rb for the 2D MOT was inside of a sealed glass ampoule. To break this ampoule the UHV section was valved off from the pumps. The gate valve GV was closed connecting the 2D and 3D MOT sections and the valve V3 to the ion pump IP3 closest to the high vacuum pumps was also closed. The reason for this was to protect the 3D MOT region and UHV pumps from contamination while breaking the ampoule. Valves V1, V4 and V8 were left open so that the 2D MOT section could be pumped on while the Rb ampoule was being broken and heated. Breaking the ampoule involved pushing the linear drive mechanism over the top of the Rb ampoule to break the glass which was prescored so that the top snapped off easily. When the ampoule broke the Ar in the ampoule was released and the pressure went above 10^{-4} Torr dropping rapidly as the Ar was pumped away.

Once the ampoule was broken the custom holder and the tee holding the Rb ampoule was wrapped in heater tape and heated up over several hours to 75 °C. This is to release Rb vapour into the 2D MOT chamber so that there is Rb to trap in the 2D MOT. The 2D MOT chamber was pumped on using the bakeout station and several (5-10) Ar bursts from Ar trapped inside the Rb were seen on a RGA. To see whether Rb was being released a laser beam was shone through a viewport close to the ampoule region scanning over the $5^2S_{1/2}$ to $5^2P_{3/2}$ transition of ^{85}Rb. A photodetector was also placed close to the beam to detect fluorescence and the photodetector readout on an oscilloscope was averaged to reduce noise. Once the ampoule region was at 75 °C it took several hours to see fluorescence close to the

ampoule region. After turning off the heat and letting the ampoule region cool for a short time the valve connecting the 2D MOT chamber to the turbo and scroll pump (V4) and the valve for the Rb ampoule (V8) was closed by hand.

A few days later the ampoule was heated again up to 86 °C while pumping on the 2D MOT chamber using the turbo and scroll pump on the bakeout station. Again valve V4 and V8 were open for heating and closed while cooling.

Several weeks later we opened up the Rb ampoule valve V8 (not heating). The gate valve (GV) was open also and the pressure in the UHV region shot up to 10^{-5} Torr. The UHV section was opened to the bakeout station pumps and the UHV region recovered to the 10^{-9} Torr range from the 10^{-10} Torr range previous to the leak. The leak was traced to a seal at the top of the Rb ampoule valve V8. Tightening this seal stopped the leak as determined by a He test detected with the RGA on the bakeout station. The ampoule valve V8 had its top uncovered to air to allow access to tighten it while the bottom portion was heated so it seems that the temperature differential on the valve caused the leak. The heater tape was moved away from the valve and the ampoule was heated to 95 °C for about an hour. After this valve V4 connecting the 2D MOT chamber was closed and the rubidium ampoule valve V8 was left open.

After the leak was fixed, running the Ti-Sub pump several times for 1-2 min at 48 A allowed the pressure to decrease to around 2×10^{-10} Torr. The NEG was also reactivated but it is not clear that helped as the baseline pressure was higher than before to start with very slow decrease. Again the Ti-Sub was run around 1.5 min several times and then the UHV section pressure slowly made its way to 9.4×10^{-11} Torr over the course of several months with valve V5 closed. This is from an original low of 8.9×10^{-11} Torr prior to the leak. Currently the base pressure with only the UHV pumps is 6.7×10^{-11} Torr.

After breaking and heating the ampoule the next step was to try to produce a 2D MOT. The next section explains the optical setup used for creating a 2D MOT and for the first version of the 3D MOT.

5.8 Optics

The $5^2S_{1/2}$ to $5^2P_{3/2}$ D2 transition is used for trapping of either ^{85}Rb or ^{87}Rb. The pump is chosen to be the $F = 2$ to $F' = 3$ transition for ^{87}Rb and $F = 3$ to $F' = 4$ transition for ^{85}Rb. The repump is chosen to be the $F = 1$

to $F' = 2$ transition for ^{87}Rb and $F = 2$ to $F' = 3$ transition for ^{85}Rb. Light that is 180 MHz from the repump and pump transitions for either ^{87}Rb or ^{85}Rb is brought over to the experimental table from a central table that provides the initial frequency stabilized light for all of our experimental tables [29, 30]. The fibers are from OZ optics.

The optical setup is shown in Fig.5.9. A list of optical components used in the setup with part numbers is given in Table. 5.1

Table 5.1: Optical Components used in Fig. 5.9

Component	Part Number	Vendor
Quarter wave plate	WPL1212-L/4-780	Casix
Half wave plate	WPL1212-L/2-780	Casix
Acousto-optical modulator	ATD-801A2	IntraAction Corp.
Polarizing Beam Splitter	BPS0202	Casix
Fiber collimator	F230FC-B	Thorlabs
Mirror	45606	Edmund Optics
Optical Isolator	I-80-T4-H	Isowave
Tapered Amplifier	TEC-400-0780-2500	Sacher Lasertechnik
Laser diode	MLD780-100S5P	MeshTel
Lenses	various e.g. LA1484-B	Thorlabs
Irises	53914	Edmund Optics
Fiber collimator	F230FC-B	Thorlabs

For the repump light the fiber light from the central table (1.5 mW) injects a slave laser diode (MeshTel MLD780-100S5P at 18 °C) which outputs 44 mW. This laser diode light is shifted up to an experimental frequency of 5 MHz below resonance using an acousto-optical modulator (AOM) in a double pass configuration. Part of the repump light is used for the 2D MOT (5.7 mW in each arm to total 11.4 mW). The remainder of the repump is coupled into a fiber and into a 2 by 6 fiber splitter (Evanescent Optics Inc) used for the 3D MOT. There is 0.7 mW repump light in each fiber output of the splitter.

The pump fiber light from the central table (1.1 mW) injects a slave (again MeshTel MLD780-100S5P at 18 °C). This slave light is coupled into a fiber and about 7.8 mW sent into a tapered amplifier (TA) which generates approximately 1W out of a high-power fiber. A tapered amplifier is a semiconductor gain medium with a tapered shaped. A small sized input beam to the tapered amplifier with reasonable powers can achieve significant amplification. The tapered amplifier (TA) is from Sacher Lasertechnik

(TEC-400-0780-2500) with a fiber coupled input and ouput. The TA light is sent to three double pass AOMs. One for the 3D MOT pump light which is fiber coupled into the 2 by 6 splitter (giving 18 mW pump in each of the six fibers). A second double pass is for the push beam for the 2D MOT which is also fiber coupled (0.4-0.6 mW out of push fiber, approximately 2 mm diameter). A third double pass is for the the 2D MOT pump light. The 2D pump light is combined with the repump and is sent free space to the 2D MOT chamber. There is 54 mW pump light in each 2D MOT arm (108 mW total). The 2D MOT beam for each arm of the 2D MOT is increased in size with several lenses to a size of approximately 25 mm diameter. Fig. 5.10 shows the lenses and mirrors used to expand the 2D MOT pump and repump for one arm and sent to the 2D MOT chamber. The pump and repump beams for the 2D MOT are expanded using a -50 mm focal length plano concave lens (1 inch diameter lens) labelled L1 in Fig. 5.10 , then a -75 mm focal length plano concave lens (1 inch diameter) labelled L2 and finally a 3 inch diameter plano convex +200 mm focal length lens labelled L3. The mirrors used to direct the expanded laser beams to the 2D MOT chamber are 75 mm by 75 mm and are from Edmund optics (part number 45341). The direction of the push beam from a fiber collimator is shown in Fig. 5.10 as well. The 2D MOT was aligned so that outer edge of the beams clip on the entrance of the differential pumping tube so that the 2D MOT cloud is close to the tube. Looking down the axis of the atomic beam with a camera focused on the differential pumping tube entrance we were able to see the flourescence of the laser beams and a 2D MOT (see Fig. 5.11). With independent control of each of the four 2D MOT coils we aligned the 2D MOT to overlap with the differential pumping tube. With the camera removed the push beam was sent down the atomic axis and aligned to pass through the differential pumping tubes by sending a flashlight down from the other end of the apparatus and aligning the push beam to that.

The 2D MOT operates 12 MHz below resonance and the push beam is 12 MHz above resonance. To detect the presence of an atomic beam making its way to the 3D MOT region we setup a 3D MOT. This turned out to be the best way to initially detect flux coming from the 2D MOT where the initial signals from methods described in the next chapter were too weak to detect the presence of the beam. For the 3D MOT, three of the six fibers from the fiber-splitter were used to make a retroreflection MOT. The other three fibers were used for general purposes such as the beam divergence measurement described in the next chapter. Each arm of the 3D MOT consisted of a bare fiber output followed by a lens (100 mm PCX) and a 1 inch quarter waveplate (see Fig. 5.12). The optics are mounted using cage

mount components from Thorlabs. To provide a retroreflection a quarter waveplate and mirror are placed on the opposite side of the cell. The 3D MOT pump was 12 MHz below resonance. The 3D MOT optics are mounted on an 80 20 frame that is used to support the compensation coils. These coils are not currently in use but would be for loading into a optical dipole trap which may be implemented in the future. There are six compensation coils in total two of which encircle the cell and had to be installed prior to the cell during the vacuum assembly.

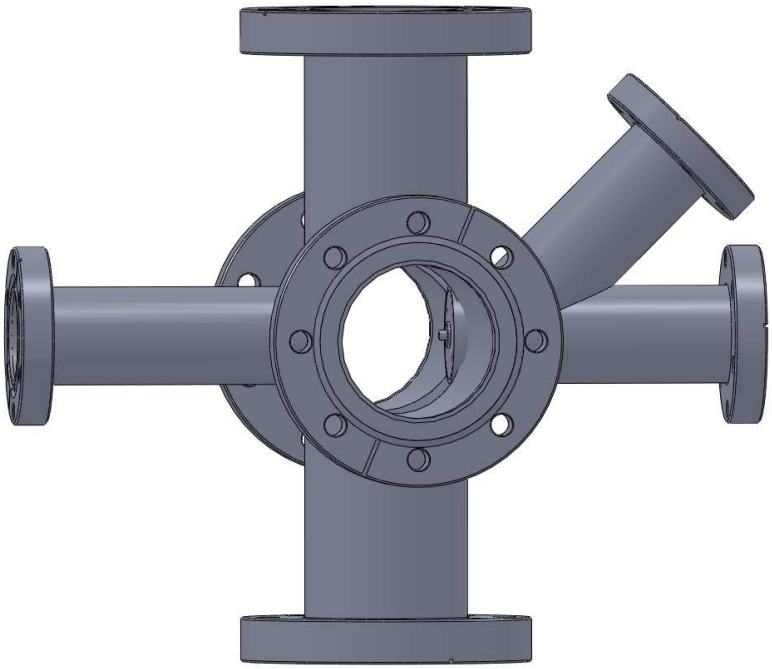

Figure 5.3: The custom made 2D MOT chamber. The differential pumping tube (see Fig. 5.4) can be seen to protrude slightly into the chamber. This tube then leads to an opening where an ion pump is attached on the port that is coming out at a 45 degree angle. A second series of tubes connects this opening to the 3D MOT chamber. The four large ports are for the viewports through which the 2D MOT laser beams are sent. The port on the left in the figure is attached via a six way cross to the Rb source and to viewports. These viewports were used to view the fluorescence of the Rb vapour when first heating the Rb source. Also a viewport in line with the atomic beam axis is used both to view the 2D MOT and to send a push beam that sends the atoms towards the 3D MOT region.

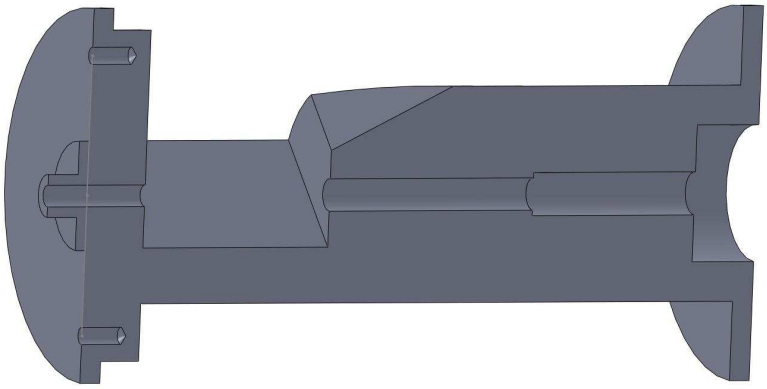

Figure 5.4: A cut away of the differential pumping section. Atoms travel from left to right through one tube and then through another series of tubes before exiting and going to the 3D MOT cell. Atoms in the atomic beam have a high directionality and will make their way through the tubes. Atoms that randomnly enter the tubes from the vapour on either side of the 2D or 3D MOT regions will tend to bounce around in the section between the two different tube sections and be pumped away by an ion pump.

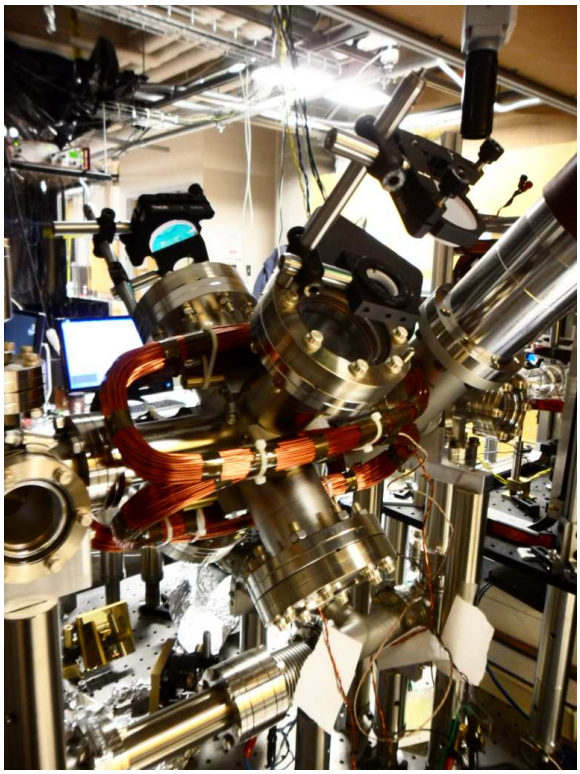

Figure 5.5: Four rectangular coils are slipped around each of the four viewports of the 2D MOT chamber and provide the magnetic field gradient for the 2D MOT.

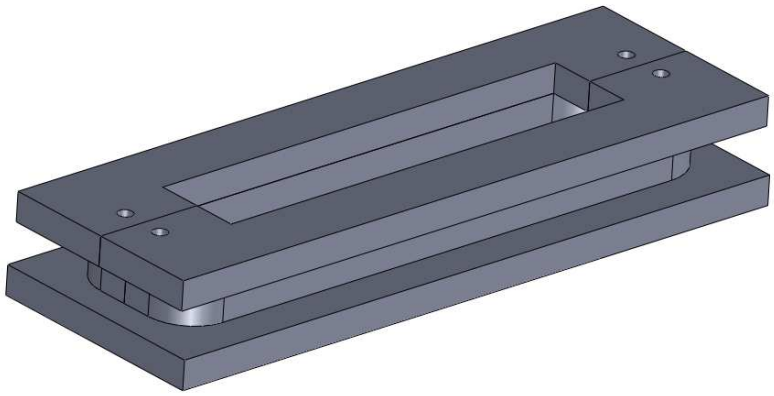

Figure 5.6: A drawing of the frame used to wind the 2D MOT coils. The frame is made to separate away from the coils once the coils are wound. The coil is held together by wrapping high temperature kapton tape around the coil in a few places. The coils can then be slipped over the viewports of the 2D MOT chamber.

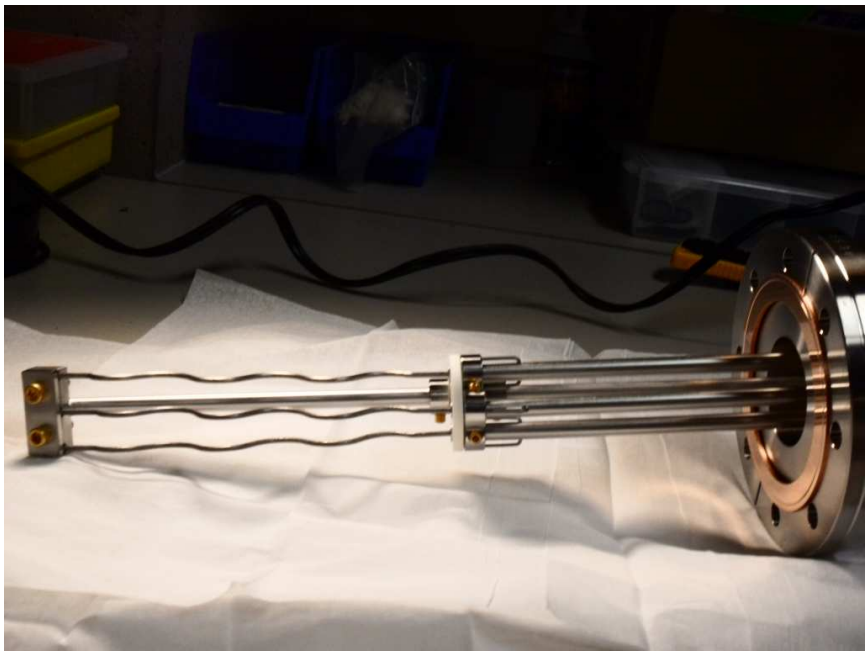

Figure 5.7: A picture of the titanium sublimation pump. The wavy metal is three titanium filaments. They are mounted such that high currents can be put through them sublimating the titanium and coating surrounding structures in the vacuum apparatus. The thin titanium layer coating the surround surfaces acts like a pump because gases bind to it.

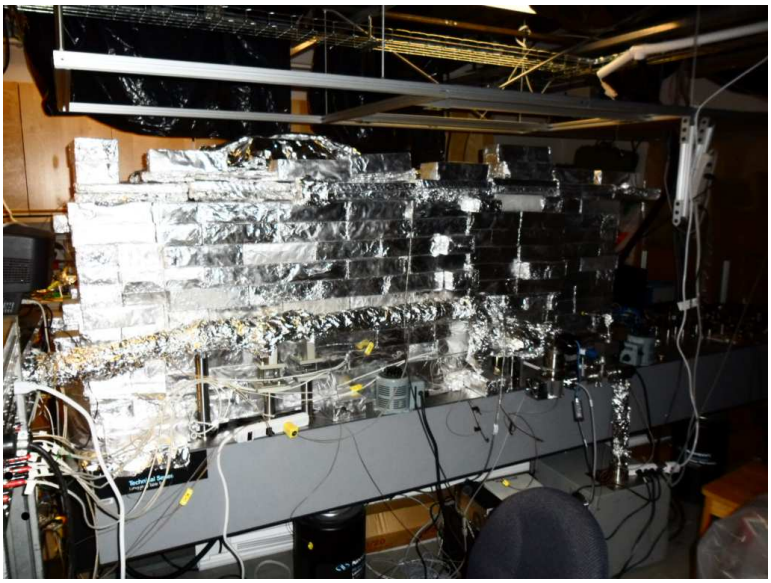

Figure 5.8: A picture of the oven built around the setup to bakeout the vacuum apparatus.

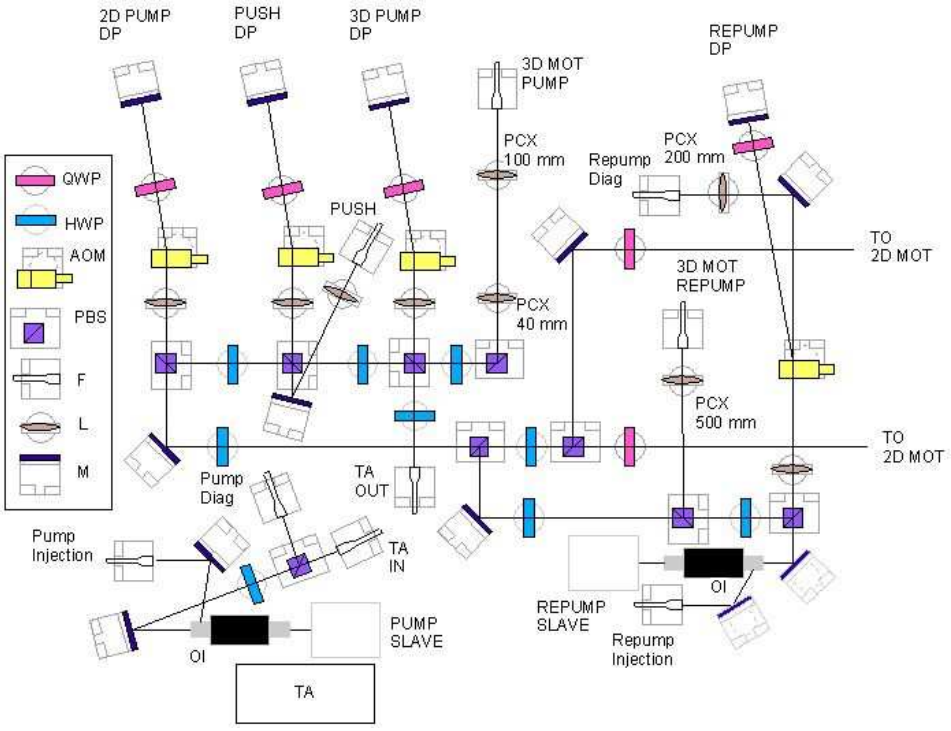

Figure 5.9: A schematic of the optical setup. QWP: quarter wave plate. HWP: half wave plate. AOM: acousto-optical modulator. L: plano-convex lens (f = 300 mm unless otherwise noted). PBS: polarizing beam splitting cube. F: fiber output/input using fiber collimator. M: mirror. The repump slave light is shifted to its experimental frequency by an AOM in double pass configuration (REPUMP DP). The repump light is sent to a fiber (3D MOT repump) for use in the 3D MOT. The rest is sent to the 2D MOT to form the two arms of the 2D MOT. The pump slave light is sent to a fiber (TA IN) which is sent to the tapered amplifier (TA). The output of the tapered amplifier (TA OUT) is sent to three AOM double passes (2D PUMP DP, PUSH DP, and 3D PUMP DP). The 2D pump light produced by 2D PUMP DP is sent free space to the 2D MOT chamber and is combined with the repump light. Push light for the 2D MOT is produced by PUSH DP and is coupled into fiber PUSH. The 3D pump light is produced by 3D PUMP DP and is sent into a fiber labelled 3D MOT PUMP. The 3D MOT PUMP and 3D MOT REPUMP fibers are coupled to a 2 by 6 fiber splitter (Evanescent Optics) used for the 3D MOT. Pump diag and Repump diag: fibers to send some pump and repump slave light to a fabry-perot cavity and absorption signal from a Rb vapour cell to ensure the slaves are injected. OI: optical isolator. Irises (not shown) are used to block unwanted orders from the AOMs.

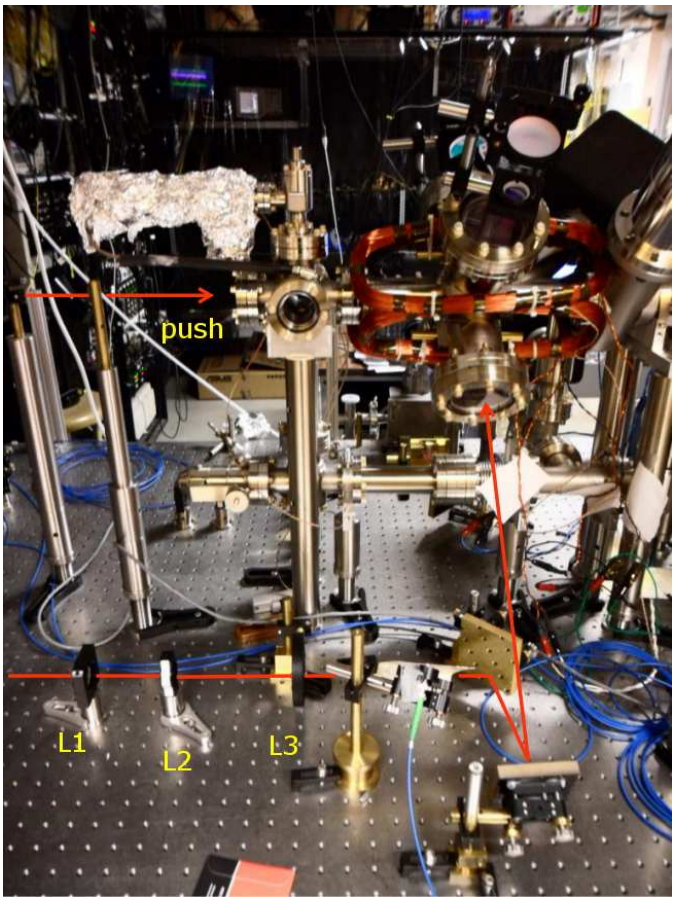

Figure 5.10: A picture of the lenses and mirrors used for expanding the 2D MOT pump and repump along one arm and sending them to the 2D MOT chamber. L1 is a f = -50 mm plano concave lens, L2 is a f = -75 mm plano concave lens and L3 is a f = + 200 plano convex lens. On the opposite side is a quarter waveplate and a mirror for retroreflection. Only one arm of the 2D MOT beams is shown. The other arm is identical coming into the 2D MOT chamber perpendicularly to the laser beams depicted in the figure. The push beam orientation and path of travel is also shown.

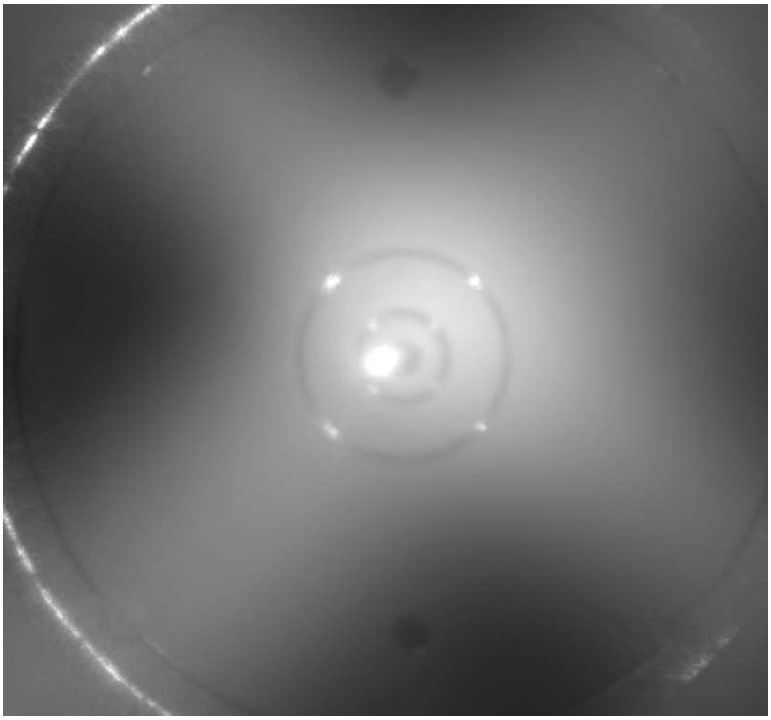

Figure 5.11: A picture of the 2D MOT cloud. The differential pumping tube is in the background. The fluorescence from the laser beams can also be seen.

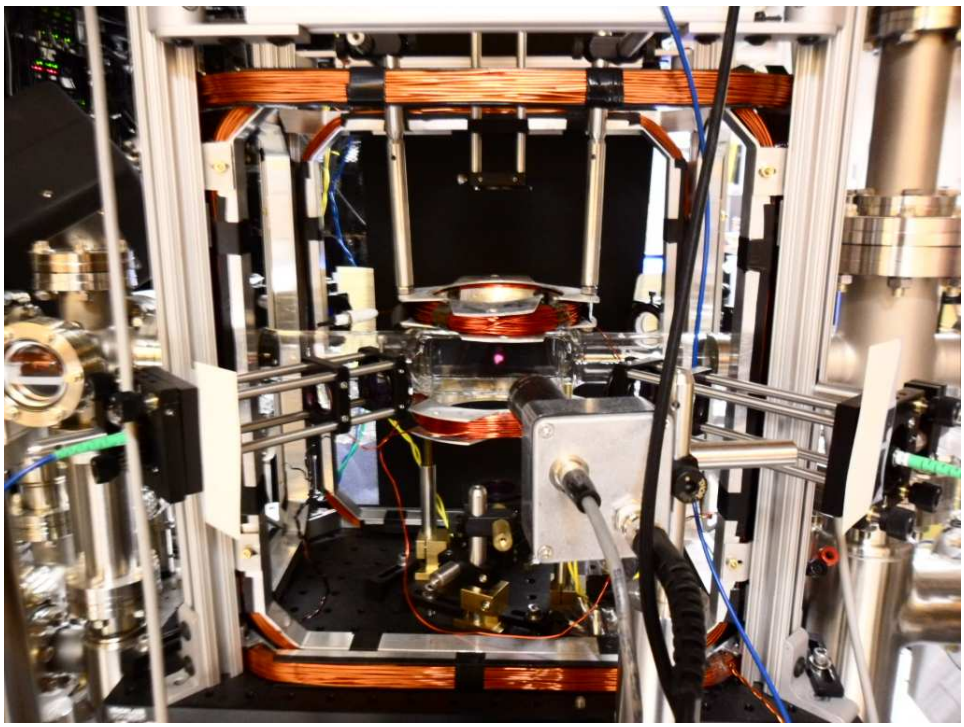

Figure 5.12: A picture of a 3D MOT loaded from the 2D MOT.

Chapter 6

2D MOT characterization

This chapter provides some characterization of the 2D MOT, including the Rb beam, such as beam divergence, flux in the atomic beam from the 2D MOT, and the speed distribution.

6.1 Rubidium atomic beam divergence characterization

Fig. 6.1 shows a schematic of the experimental setup used to measure the beam divergence of the atomic beam. An approximately 5 mm diameter diagnostic probe laser beam with 18 mW pump and 0.7 mW repump was introduced perpendicular to the direction of the atomic beam and retroreflected. The purpose of the retroreflection is to decrease the deflection and ensure the probe beam perturbs the atomic beam as little as possible. A camera (PixeLink PL-B741EF) was placed perpendicular to both the diagnostic laser beam and the atomic beam, and recorded the atomic beam fluorescence and an image of the background scattered light with no atomic beam present. The two images were subtracted using python code and an example result is shown in Fig. 6.2. A lens in a lens tube was attached to the camera to focus at roughly the intersection of the laser beam and the atomic beam, and to reduce stay light signal. A slice of the subtracted images taken going through the atomic cloud was fit to a gaussian, $ae^{-\frac{((x-u)/w)^2}{2}}$, giving $w = 133$ pixels. The diameter of the atomic beam is $2w = 266$ pixels. Based on taking a camera picture of an object of a known size, a 10 mm width corresponds to 372 pixels. This gives a atomic beam size of ≈ 7 mm in diameter at the place where the fluorescence picture was taken. The distance from the entrance tube of the differential pumping section to where the fluorescence picture was taken is 258 mm. This gives a full angle divergence of 28 mrad. The distance from the tube entrance to 3D MOT center is 55 cm so that the atomic beam size at the 3D MOT is approximately 15 mm in diameter.

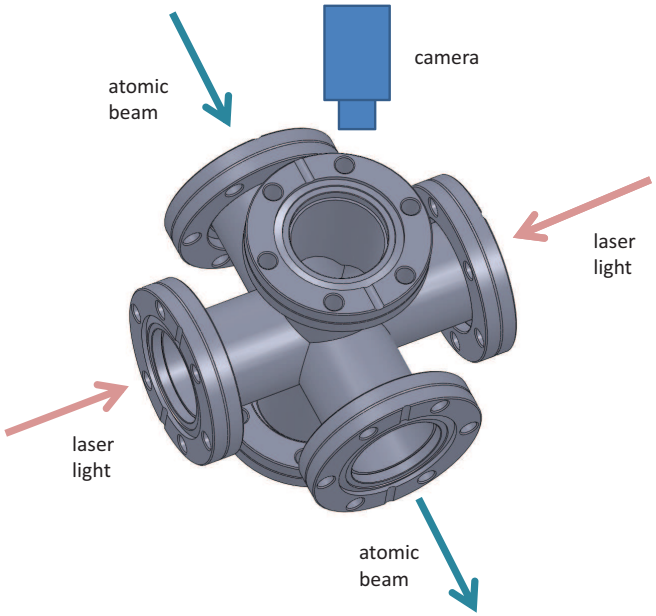

Figure 6.1: The setup used to measure the atomic beam divergence. Fluorescent laser light (pump and repump) was incident on the atomic beam perpendicular to the atomic beam motion. The laser beam was retroreflected. A picture with a camera was taken with and without the atomic beam present.

6.2 Atomic speed distribution characterization

To measure the speed distribution coming from the 2D MOT we used the 3D MOT as a diagnostic tool. The fluorescence of the trapped atoms in the 3D MOT was recorded as a function of the time after the 2D MOT was turned on and the atomic beam established. The 2D MOT was turned on by energizing the 2D magnetic field coils with the 2D MOT light already on. The 2D MOT is turned on with the 3D MOT light and magnetic field already on. Fig. 6.3 shows the resulting fluorescence data. The voltage on the photodiode from fluorescence of the atoms trapped in the 3D MOT, as

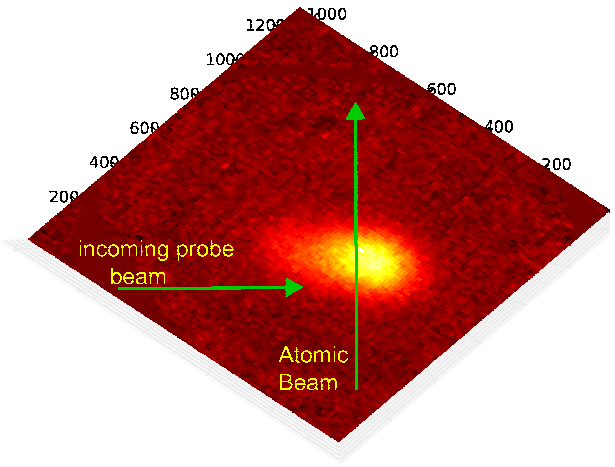

Figure 6.2: A fluorescence image of the Rb beam. The result of subtracting pictures taken with a camera as shown in Fig. 6.1, with and without the atomic beam present. A portion of the atomic beam is shown. The direction of travel of the atomic beam and the probe laser beam are labelled. Note the center of the beam seems to be pushed to the side slightly, it is not certain what the cause of this is.

given in Eq. 3.1, is

$$V(t) = \alpha\gamma_{\rm sc}N \tag{6.1}$$

As also given in Eq. 1.1 we have that the number of atoms in a 3D MOT, $N(t)$, from initial loading follows

$$\frac{dN}{dt} = R - \Gamma N - \beta \int n^2(\vec{r},t)\, d^3\vec{r} \tag{6.2}$$

where Γ and β are loss rate constants due to background collisions and intra-trap collisions respectively. The density of the trapped atoms at position $\vec{r}$ from the center of the trap at time t is $n(\vec{r},t)$. For short times following initial loading of the 3D MOT the loss terms can be neglected since there are not many atoms accumulated yet, meaning both N and $n(\vec{r},t)$ are small. This means we can approximate

$$\frac{dN}{dt} = R. \tag{6.3}$$

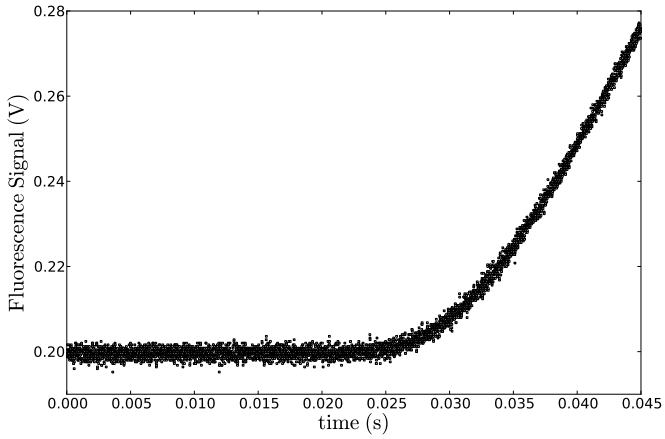

Figure 6.3: A plot of the 3D MOT fluorescence captured on a photodiode as a function of time from initial turn on of the 2D MOT. The 2D MOT is turned on with the 3D MOT light and magnetic field already on. The curvature gives information about the speed distribution of the atomic beam.

Combining Eq. 6.3 with Eq. 6.1 we have

$$\frac{dV}{dt} = \alpha\gamma_{\mathrm{sc}}\frac{dN}{dt} = \alpha\gamma_{\mathrm{sc}}R. \tag{6.4}$$

This links a measurable quantity, the initial slope of the fluorescence voltage curve, to the loading rate, R.

The 3D MOT has some maximum capture speed, v_{c}, so that atoms travelling to the 3D MOT from the 2D MOT that are exceeding this speed will not be trapped. There is a distribution of speeds, $f(v)$, coming from the 2D MOT. The loading rate, R, of the atoms into the trap will initially change as a function of time as atoms of different speeds arrive at the 3D MOT region. The curve in the fluorescence data shown in Fig. 6.3 relates to the speed distribution of the atomic beam arriving at the 3D MOT. If the speed probability distribution coming from the 2D MOT is $f(v)$ then the loading rate as a function of time, t, from initial turn on of the 2D MOT will follow

$$R(t) = \phi \int_{d/t}^{v_c} f(v)\, dv. \tag{6.5}$$

In Eq. 6.5 d is the distance from the exit tube of the 2D MOT to the 3D MOT capture region, and $t \geq (t_c = d/v_c)$. The total number per second from the 2D MOT is ϕ. When the curve in Fig. 6.3 becomes linear then

$$R_{\max} \approx \phi \int_0^{v_c} f(v)\, dv \tag{6.6}$$

meaning that the majority of all speed classes have reached the 3D MOT region from initial turn on of the 2D MOT.

To extract the shape of $f(v)$ a few mathematical rearrangements are needed. First the derivative of $R(t)$ from Eq. 6.5 is taken giving

$$\frac{dR(t)}{dt} = \phi f(d/t)(\frac{d}{t^2}). \tag{6.7}$$

Next $\frac{dR(t)}{dt}$ is obtained from Eq. 6.4 and inserted into Eq. 6.7 giving

$$\frac{1}{\alpha\gamma_{\rm sc}}\frac{d^2V}{dt^2} = \phi f(d/t)\frac{d}{t^2}. \tag{6.8}$$

Now we divide both sides by $R_{\max}$ given in Eq. 6.6

$$\frac{1}{R_{\max}\alpha\gamma_{\rm sc}}\frac{d^2V}{dt^2} = \frac{f(d/t)\frac{d}{t^2}}{\int_0^{v_c} f(v)\, dv} \tag{6.9}$$

Finally we apply Eq. 6.4 again to write $R_{\max}$ in terms of voltage giving

$$\frac{1}{(\frac{dV}{dt})_{\max}}\frac{d^2V}{dt^2} = \frac{f(d/t)\frac{d}{t^2}}{\int_0^{v_c} f(v)\, dv} \tag{6.10}$$

Solving for $f(d/t)$ gives

$$f(d/t) = \frac{V''}{V'_{\max}}\frac{t^2}{d}\int_0^{v_c} f(v)\, dv \tag{6.11}$$

where the prime indicates differentiation with respect to time and the integral involving $f(v)$ is a constant.

The goal now is to extract the speed probability distribution, $f(v)$, from the data shown in Fig. 6.3. A python script was used to numerically extract the second derivative, V'', and the maximum slope, $V'_{\max}$, from the data as a function of time from the 2D MOT turn on. The method used here was to take a time interval of 0.007 s starting at t=0 and fit the fluorescence data, shown in Fig. 6.3, for that time interval to a line. The interval was then

shifted in time by 300 μs and then fit again. The slope of the linear fits was recorded and assigned a time at the center of each interval. This provides the first derivative of the original fluorescence data. The second derivative is obtained by repeating this procedure on the first derivative results. A plot of $\frac{V''}{V'_{\max}}\frac{t^2}{d}$ versus speed $v = d/t$ is given in Fig. 6.4

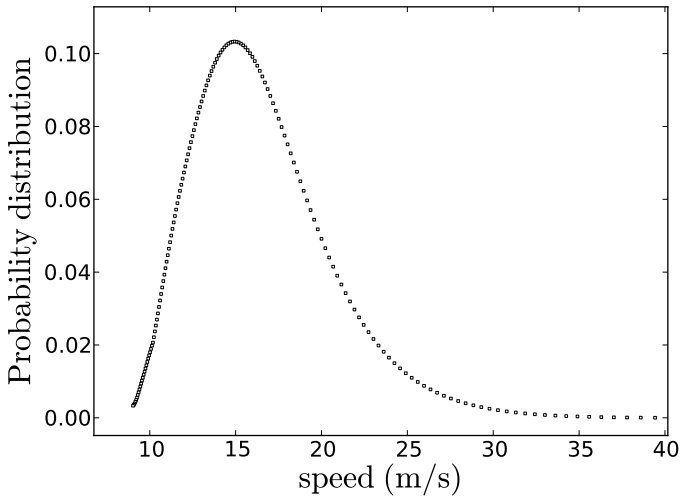

Figure 6.4: The speed distribution of atoms in the atomic beam from the 2D MOT. This curve is extracted from the fluorescence of the 3D MOT recorded from initial turn on of the 2D MOT.

Looking at Fig. 6.3 the 3D MOT fluorescence starts to rise approximately at 0.021 sec from initial turn on of the 2D MOT. The distance from the entrance of the differential pumping tube on the 2D MOT side to the 3D MOT center is 55 cm. This gives an approximate capture speed, v_c, of the 3D MOT as 26 m/s. From Fig. 6.4 one can see the bulk of of the speed probability distribution of the atomic beam lies below 26 m/s so that we approximate $\int_0^{v_c} f(v)\,dv \approx 1$. With this approximation Eq. 6.6 gives $R_{\max} \approx \phi$. Using $R_{\max} = \frac{1}{\alpha\gamma_{\text{scat}}}\left(\frac{dV}{dt}\right)_{\max} \approx \phi$ we can find an approximate value for ϕ. The max slope $\left(\frac{dV}{dt}\right)_{\max}$ is given by the data as the slope in the linear portion of Fig. 6.3. The coefficient α can be given as

$$\alpha = \frac{(r_{\text{lens}})^2}{4(d_{\text{MOT}})^2}\eta\frac{hc}{\lambda}\epsilon. \tag{6.12}$$

The first factor gives the fraction of the total solid angle collected by a plano-convex lens of focal length 60 mm with radius, r_{lens}, placed a distance d_{MOT} from the 3D MOT. The power to voltage conversion factor of the photodiode is η and $\frac{hc}{\lambda}$ is the energy of a fluoresced photon. ϵ describes the transmitted fraction of photons as the fluorescent light travels through the cell once. In our case $r_{\text{lens}} = 11.5$ mm, $d_{\text{MOT}} = 14.5$ cm, $\eta = 4.68\text{V}/\mu\text{W}$, and $\epsilon = \sqrt{11.2/11.5}$. The ϵ was determined by measuring one of the 3D MOT incoming beams as 11.5 mW before it entered the cell and 11.2 mW after it exited the cell having passed through two sides of the cell. This gives $11.5\epsilon^2 = 11.2$.

The scattering rate (number of photons per second emitted per atom per second) can be expressed as

$$\gamma_{\text{sc}} = \frac{\Gamma}{2}\left(\frac{s}{1+s+(\frac{2\delta}{\Gamma})^2}\right) \tag{6.13}$$

where δ is the detuning of the MOT pump light from resonance which for our experiment was 12 MHz. Γ is the natural line width of the pump transition [58] which is $2\pi \times 6.07$ MHz. The parameter $s = \frac{I}{I_{\text{sat}}}$ where I is the total intensity of the MOT pump beams and I_{sat} is the saturation intensity of the pump transition which is 1.67 mW/cm^2 for the $F = 3$ to $F' = 4$ transition for ^{85}Rb on the $5^2S_{1/2}$ to $5^2P_{3/2}$ transition for circularly polarized light. In the pressure sensor experiment, with each of the three arms having 18 mW initially travelling to the cell and getting retroreflected, the total pump power in the MOT is $P_{\text{tot}} = 3(18 \times \epsilon) + 3(18 \times \epsilon^3)$. The intensity $I = \frac{P_{\text{tot}}}{A}$ where area, A, is taken as $\pi {r_{\text{MOT}}}^2$ where r_{MOT} is the radius of the MOT pump beams. For our experiment the MOT beams were roughly 23 mm in diameter.

Combining our values for α and γ_{sc} gives $\alpha\gamma_{\text{sc}} = 3.23 \times 10^{-8}$ V. The value of $(\frac{dV}{dt})_{\text{max}} = 6.13$ so that $R_{\text{max}} \approx \phi = 2 \times 10^8$ atoms/s total comes from the 2D MOT beam.

Chapter 7

Loss rate measurements in a 3D MOT

This chapter describes two experiments where the loss rate Γ due to background collisions was measured in a MOT as pressure in the 3D MOT chamber varied. The first experiment was when the residual background pressure was varied and the second was when Ar was introduced into the system.

7.1 Total pressure measurement of residual background gas

This section is not related to 2D MOT characterization but is included as an interesting experiment performed while still tuning up the experimental apparatus and using components for the first time. Pressure measurements were taken with the ion gauge installed on our apparatus as the pressure varied due to outgassing of a residual gas analyzer installed on the bakeout system which is connected to our apparatus.

Degassing of residual gas analyzers (RGAs) and ion gauges occurs when a high current is run through the filaments. Degassing serves to clean the analyzers/gauges and typically a large amount of gas is released while degassing. With the system being brand new, and the RGA connected to the 3D MOT chamber having been exposed to atomsphere during shipping, we thought it best to degas the Pfeiffer RGA installed on our system. In preparation for degassing the Pfeiffer RGA we valved off the UHV pumps (with valve V6 in Fig. 5.1). The 3D MOT section was opened up to the bakeout station (with valves V5 and V1). The valve V3 connected to the ion pump labelled IP1 in Fig. 5.1 was also closed. The reason for this was that when degassing the RGA it was expected that the pressure might rise to a high enough level to overload the ion pumps. It turned out the Pfeiffer RGA with grid-ion source used on our apparatus can not be degassed and is designed for low outgassing rate but at that time this was not known.

The RGA on the bakeout station (RGA 200, Stanford Research Systems)

was turned on to monitor what we thought would be coming off of the Pfeiffer RGA. When the SRS RGA was turned on it caused the pressure to rise significantly. With the UHV pumps closed off the base pressure was around 1×10^{-8} Torr. When the RGA was turned on from the bakeout station the pressure rose to around 2×10^{-7} Torr and over the period of 5 hours dropped to 4.5×10^{-8} Torr. The SRS RGA was then shut off and the system pressure decreased down to the 1×10^{-8} range after another 3 hours.

As the pressure in the system was varying loading curves of the 3D MOT were recorded. The loading curves were recorded by turning off the 3D MOT magnetic field and then turning it back on and recording the fluorescence on a photodetector in the same way as described in section 3.2.1. The loading curve voltage was fit to $V(t) = A(1-e^{-\Gamma t})+B$. The coefficient $A = \alpha\gamma_{\text{scat}}\frac{R}{\Gamma}$ converts the steady state atom number $\frac{R}{\Gamma}$ to a steady state voltage. The coefficient B accounts for any offsets which commonly occur in experimental data due to, for example, scattered laser light and background light in the room. Fig. 3.2 shows an example of a loading curve.

Fig. 7.1 shows a plot of Γ versus pressure from fitting the loading curves. Arpornthip et al. [25] performed semi-classical calculations for the slope of Γ versus P for a 1K trap of Rb atoms and various background gases at a temperature of 300K. The results were 2.6×10^7 Torr/s for N_2 and for CO_2 while H_2 was 4.9×10^7 Torr/s. RGA scans taken with the Pfeiffer RGA showed that when the SRS RGA was first turned on the dominant species were N_2 or CO, CO_2 and H_2 while as the pressure decreased H_2 became increasingly the dominant species. This means as the background pressure decreased in our system and hydrogen became the dominant species the slope of Γ versus pressure P became steeper.

Arpornthip et al. [25] proposed that a MOT could provide rough measurements of background pressure (within a factor of two). As seen in Eq. 2.1 the loss rate due to background collisions, Γ, can be expressed as

$$\Gamma = \sum_i n_i \langle \sigma v_i \rangle_{X,i} \tag{7.1}$$

where n_i is the background density of species, i, and $\langle \sigma v_i \rangle_{X,i}$ is the velocity averaged loss cross section for collisions between the background species i and trapped atoms (labelled type X). Writing Eq. 7.1 in terms of partial pressure $P_i = n_i k_B T$ gives

$$\Gamma = \sum_i \frac{P_i}{k_B T} \langle \sigma v_i \rangle_{X,i}. \tag{7.2}$$

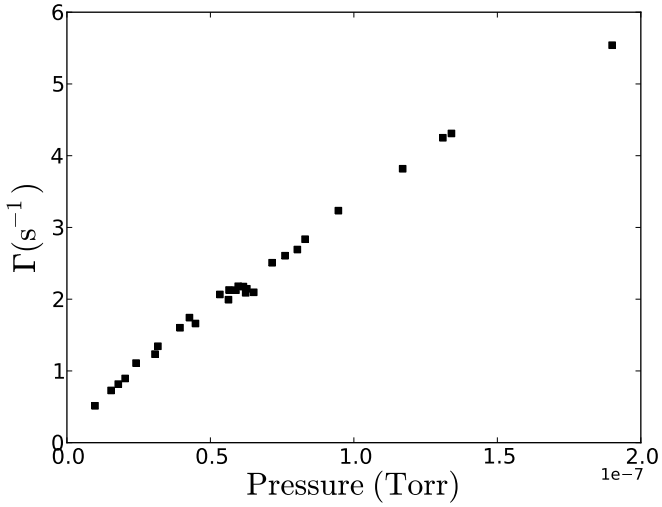

Figure 7.1: The loss rate constant, Γ, due to background collisions versus total background pressure. The pressure increased after a residual gas analyzer was turned on and then decreased. As the pressure decreased loading curves of the 3D MOT were taken. The loading curves (photodiode fluorescence) were fit to $V(t) = A(1 - e^{-\Gamma}t) + B$ to extract Γ.

Arpornthip et al. calculated that $\langle \sigma v_i \rangle_{X,i}$ varies roughly within a factor of two independent of background species choice i and can be pulled out of the summation. They estimate for background gases such a H_2, He, H_2O, N_2, Ar, and CO_2, that the quantity $a = \frac{\langle \sigma v_i \rangle_{X,i}}{k_B T}$ has an an approximate value of $a = 2 \times 10^7$ to 5×10^7 Torr^{-1} s^{-1}. This is for Rb as the trapped atom species. Assuming a is roughly the same for the different background species a can come out of the summation. This gives a sum over partial pressures which adds to total pressure giving

$$\Gamma = aP. \tag{7.3}$$

By taking measurements of Γ and using the rough values given for a one can determine the background pressure in their system using a MOT. This idea is very similar to our proposed pressure measurement using trapped atoms but is different in that this technique is useful for lower precision pressure measurements and not for a primary standard of pressure.

7.2 Measurement of background loss rate in a MOT for various pressures of Ar background gas

The loss rate constant, Γ, due to background collisons was measured for various Ar pressures. The fluorescence of the 3D MOT was recorded. While the 3D MOT conditions were on, the 2D pump light and push light were turned off and the push shutter was closed. The atom number in the 3D MOT then decayed exponentially and was fit to extract Γ. The data from was fit from a time 30 ms after initial turn off of the 2D MOT to account for the time needed for the atomic beam to stop travelling to the 3D MOT. The background pressure before Ar was added was 2.97×10^{-9} Torr. Ar was added through a leak valve installed on the bakeout station which was connected to the apparatus. The original leak valve on the apparatus failed and needs replacing. The ion gauge and SRS RGA on the bakeout station were turned off during measurement and the Pfeiffer RGA was also turned off. The Pfeiffer RGA generally increases the residual background pressure by 1.5 to 2 times so it was also turned off to keep the residual background pressure as low as possible. The measurements of Γ in the 3D MOT as a function of Ar pressure are shown in Fig. 7.2 on a log-log plot. At each Ar pressure five decay traces were taken at each pressure and averaged and then fit. The Γ versus the pressure of Ar was fit to a line and the slope extracted giving a velocity averaged loss cross section of 0.645×10^{-9} cm^3/s . This corresponds approximately to a trap depth of 2.1 K for the MOT in its present setup.

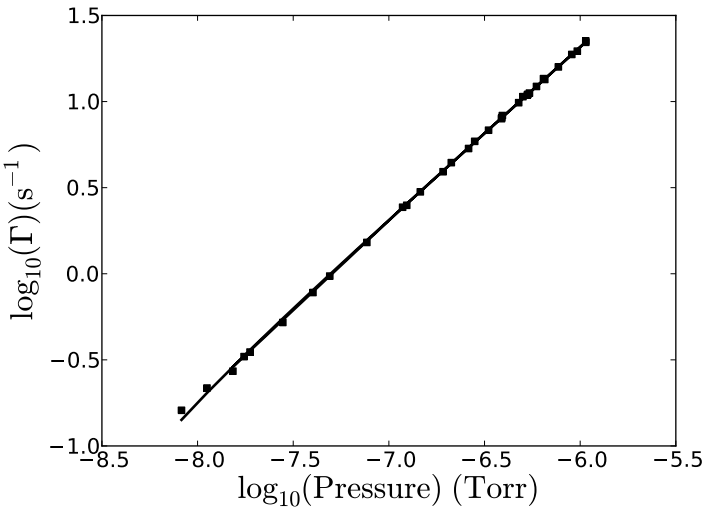

Figure 7.2: Measurements of loss rate constant, Γ, in a MOT at various Ar pressures. The Ar pressure was measured with an ion gauge.

Chapter 8

Future Outlook and Conclusions

8.1 Future Outlook

So far the work on the atom pressure sensor has shown that the 2D MOT is operational and that a 3D MOT can be loaded from it. Preliminary data of the dependence of the loss rate constant, Γ, with pressure measured with an ion gauge have been taken with a 3D MOT. Further experimental goals are to trap atoms in a magnetic trap, introduce gases into the system, and take measurements of pressure with the trapped atoms. These pressure measurements would be compared with pressure readings from commercial gauges and calibrated gauges to be sent from the national institute of standards and technology.

8.1.1 Magnetic trapping coils

The same magnetic coils used for the 3D MOT of the pressure sensor apparatus will be used for magnetic trapping. The 3D MOT coils currently in place do not provide a gradient deep enough for magnetic trappping of atoms from the 3D MOT. To perform pressure measurements using the loss rate in a magnetic trap another set of coils have been made from pvc coated hollow core copper tubing. The hollow core allows water to be run through the tubing for cooling.

The replacement coils have 8 axial windings and 8 radial windings. They are constructed from quarter inch outer diameter copper tubing with a quoted 0.03 inch wall thickness and a 0.032 inch thick PVC coating. The measured outer diameter of the copper tubing including the PVC is approximately 8.3 mm and the inner hollow core is 4.5 mm. The coil has a 188 mm outer diameter and 38 mm inner diameter. The height of each coil is 73 mm. The coil windings are secured by wrapping fiber glass tape around the cross section (see Fig. 8.1). The PVC coating is so that the coil windings do not short on each other. The tubing is from Alaskan Copper (part number

142797). The coils will be driven using a 60 V, 250 A power supply. The resistance of each coil is 38.5 Ω. The power outlet we have is 20 A and 208 V so that the maximum power from the outlet is 4160 W. For our coils this means a maximum of 233 A, however the circuit breaker goes off even for 200A unpredictably. The power outlet needs to be upgraded to a 30A, 208V to handle the 4750 W required at 250 A by the coils. Running water at 70-80

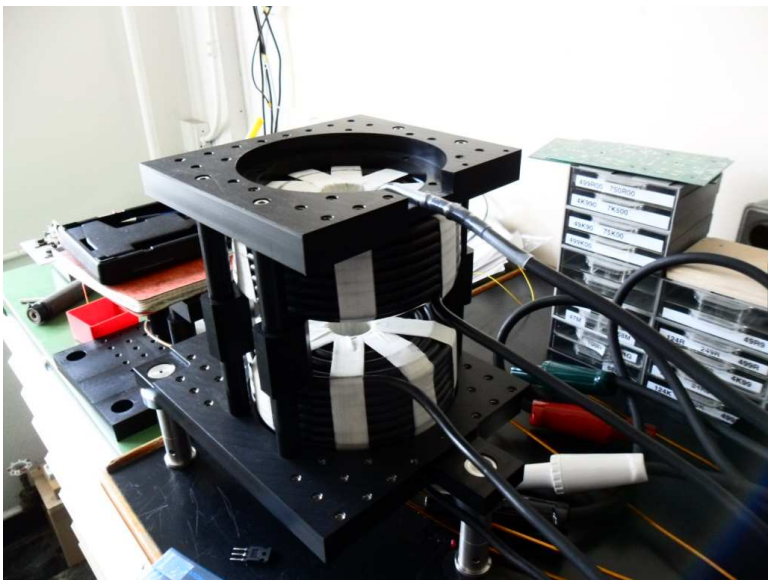

Figure 8.1: The new magnetic coils and mount for the 3D MOT and magnetic trap of the atom pressure sensor experiment.

psi from the tap in parallel through the coils gave a flow rate of 36 seconds per litre for one coil and 29 seconds per litre for the other. At 230 A, the temperature of the water exiting the coils was 28 degC. The incoming water was 11 deg C. The following paper was invaluable for designing magnetic coils using water cooled hollow core tubing [59]. The coils will be mounted by sandwiching them inbetween delrin plates with the top coil sitting on spacers in between the two coils (see Fig. 8.1.

The predicted magnetic field gradient is approximately 0.57 G/cm per A radially which would lead to a maximum radial magnetic field gradient of 125 G/cm at 250 A. From the center of the cell to where the magnetic field zero resides to the outer edge of the cell is 2 cm. The maximum magnetic field occurring at the edge of the cell would then be 250 G . The trap

depth as given in section 1.2.2 as $\Delta E = g_F m_F \mu_B B$ for the $m_F = -1$ of the $F = 1$ level of the $5^2S_{1/2}$ ground state for ^{87}Rb. Using $g_F = -1/2$ and $\mu_B = 9.274 \times 10^{-24}$ J/T from [7] and $B = 250$ G this gives a maximum radial trap depth of around 8 mK. The measured coil gradient in anti-helmholtz configuration is 0.58 G/cm/A along the radial direction and approximately double along the axial direction.

To trap atoms in a magnetic trap, coils for magnetic trapping and the supporting infrastructure such as breadboards, mounts, electrical and water connections, must be installed.

8.2 Conclusions

This thesis started with a brief description of magneto-optical trapping and magnetic traps. These traps are the tools we used to prepare and study samples of ultra cold atoms. A key parameter of interest for these traps is the loss rate constant due to background collisions, Γ. The loss rate constant was further related to the density of the background gas species. This relation involves the velocity averaged loss collisional cross section between the trapped atoms and the different background species. Quantum scattering calculations for the loss cross section were described and performed earlier in our group. The loss cross section depends on the trap depth and experimental verification of this dependence was shown previously for trap depths attainable with the magnetic trap used (up to 10 mK). This work provided verification for trap depths for a MOT ($\approx$ 1K). For this verification, a measurement of trap depth adapted from Hoffmann et al. [28] using photoassociative loss was used . Out of the relationship between Γ and the density of the background species came a proposal to measure density of a background species based on measurements of Γ and calculation of the loss cross section.

Part of the apparatus for the pressure sensor experiment was designed, assembled, baked out and a 2D MOT was shown to be operational. Future directions are to get a magnetic trap working and to make pressure measurements comparing these with commercial gauges. Gauges from NIST will need to be installed and changes to the vacuum apparatus made to accomodate these gauges. The pressure sensor experiment is important because it would allow a primary standard for pressure using ultracold atoms which has several benefits over existing standards. Those benefits are reproducibilty of standards from lab to lab, a possibly simpler experimental setup, and a faster time to calibration gauges.

Bibliography

[1] David E. Fagnan, Jicheng Wang, Chenchong Zhu, Pavle Djuricanin, Bruce G. Klappauf, James L. Booth, and Kirk W. Madison. Observation of quantum diffractive collisions using shallow atomic traps. *Phys. Rev. A*, 80:022712, Aug 2009.

[2] T. V. Tscherbul, Z. Pavlovic, H. R. Sadeghpour, R. Côté, and A. Dalgarno. Collisions of trapped molecules with slow beams. *Phys. Rev. A*, 82:022704, Aug 2010.

[3] Brian C. Sawyer, Benjamin K. Stuhl, Mark Yeo, Timur V. Tscherbul, Matthew T. Hummon, Yong Xia, Jacek Klos, David Patterson, John M. Doyle, and Jun Ye. Cold heteromolecular dipolar collisions. *Phys. Chem. Chem. Phys.*, 13:19059–19066, 2011.

[4] J. Weiner and P.-T. Ho. *Light-Matter Interaction*, volume 1. John Wiley and Sons, Inc., New Jersey, 2003.

[5] H. J. Metcalf and P. van der Straten. *Laser Cooling and Trapping.* Springer-Verlag, New York, 1999.

[6] T. P. Meyrath. Electromagnet design basics for cold atom experiments. http://george.ph.utexas.edu/ meyrath/informal/electromagnets.pdf.

[7] D. A. Steck. Rubidium 87 d line data. Internal Publication, 2001.

[8] A. Corney. *Atomic and Laser Spectroscopy.* Oxford University Press, Oxford, 1977.

[9] S. Martellucci, A. N. Chester, A. Aspect, and M. Inguscio. *Bose-Einstein Condensates and Atom Lasers.* Springer Link, 2002.

[10] John Weiner, Vanderlei S. Bagnato, Sergio Zilio, and Paul S. Julienne. Experiments and theory in cold and ultracold collisions. *Rev. Mod. Phys.*, 71:1–85, Jan 1999.

[11] J. Weiner, V. S. Bagnato, S. Zilio, and P. S. Julienne. Experiments and theory in cold and ultracold collisions. Rev. Mod. Phys., **71**, 1999.

[12] B. L. Lev. Magnetic microtraps for cavity qed, bose-einstein condensates, and atom optics. Ph.D. Thesis, California Institute of Technology, 2006.

[13] K. Overstreet, P. Zabawa, J. Tallant, A. Schwettmann, and J. Shaffer. Multiple scattering and the density distribution of a cs mot. *Opt. Express*, 13(24):9672–9682, Nov 2005.

[14] J. Van Dongen, C. Zhu, D. Clement, G. Dufour, J. L. Booth, and K. W. Madison. Trap-depth determination from residual gas collisions. *Phys. Rev. A*, 84:022708, Aug 2011.

[15] A. M. Steane, M. Chowdhury, and C. J. Foot. Radiation force in the magneto-optical trap. *J. Opt. Soc. Am. B*, 9(12):2142–2158, Dec 1992.

[16] Carl Wieman, Gwenn Flowers, and Sarah Gilbert. Inexpensive laser cooling and trapping experiment for undergraduate laboratories. *American Journal of Physics*, 63(4):317–330, 1995.

[17] D. Fagnan. Study of collision cross section of ultra-cold rubidium using a magneto-optic and pure magnetic trap. Honour Thesis, University of British Columbia, 2009.

[18] L. D. Landau and E. M. Lifshitz. *Quantum Mechanics Non-Relativistic Theory.* Addison-Wesley Publishing Company Inc., Reading, Massachusetts, 1958.

[19] D. E. Manolopoulos. Quantum scattering dynamics. Internal Publication.

[20] L. S. Rodberg and R. M. Thaler. *Introduction to the Quantum Theory of Scattering.* Academic Press, New York, 1967.

[21] R. L. Liboff. *Introductory Quantum Mechanics.* Addison-Wesley Publishing Company, Inc., second edition, 1992.

[22] L. E. Ballentine. *Quantum Mechanics.* Prentice Hall, Englewood Cliffs, N.J., 1990.

[23] B.R Johnson. The multichannel log-derivative method for scattering calculations. *Journal of Computational Physics*, 13(3):445 – 449, 1973.

[24] A. Dalgarno and W.D. Davison. Long-range interactions of alkali metals. *Molecular Physics*, 13(5):479–486, 1967.

[25] T. Arpornthip, C. A. Sackett, and K. J. Hughes. Vacuum-pressure measurement using a magneto-optical trap. *Phys. Rev. A*, 85:033420, Mar 2012.

[26] W. Kruithof. Laser trapping of sodium isotopes for a high-precision β-decay experiment. Ph.D. Thesis, University of Groningen, 2012.

[27] S. Bali, K. M. O'Hara, M. E. Gehm, S. R. Granade, and J. E. Thomas. Quantum-diffractive background gas collisions in atom-trap heating and loss. *Phys. Rev. A*, 60:R29–R32, Jul 1999.

[28] D. Hoffmann, S. Bali, and T. Walker. Trap-depth measurements using ultracold collisions. *Phys. Rev. A*, 54:R1030–R1033, Aug 1996.

[29] S. Singh. Progress towards ultra-cold ensembles of rubidium and lithium. M.Sc. Thesis, University of British Columbia, 2007.

[30] J. Van Dongen. Simultaneous cooling and trapping of ^{6}li and $^{85/87}$rb. M.Sc. Thesis, University of British Columbia, 2007.

[31] D. J. McCarron. A guide to acousto-optic modulators. Internal Publication, Durham Atomic and Molecular Physics. http://massey.dur.ac.uk/resources/slcornish/AOMGuide.pdf, 2007.

[32] J. Mitroy and J.-Y. Zhang. Long-range dispersion interactions. ii. alkali-metal and rare-gas atoms. *Phys. Rev. A*, 76:032706, Sep 2007.

[33] L. Peksa, D. Pražák, T. Gronych, P. Řepa, M. Vičar, J. Tesař, Z. Krajíček, and F. Staněk. Primary vacuum standard for uhv range - standing experience and present problems. Mapan, **24**, 77-88, 2009.

[34] B.I.P.M (Bureau International des Poids et Mesures). International vocabulary of metrology - basic and general concepts and associated terms, 3rd ed. jcgm 200:2012. Internal publication, 2008.

[35] MKS Instruments. Mks baratron® types 615a/616a/617a high accuracy sensor heads manual. Internal Publication, 2009.

[36] A. P. Miiller. Measurement performance of capacitance diapghragm gages and alternative low-pressure transduces. Internal Publication, 1997.

[37] MKS Instruments. Mks srg-3 spinning rotor vacuum gauge instruction manual. Internal Publication, 2009.

[38] Sharrill Dittmann, Bernd E. Lindenau, and C. R. Tilford. The molecular drag gauge as a calibration standard. *Journal of Vacuum Science & Technology A: Vacuum, Surfaces, and Films*, 7(6):3356–3360, 1989.

[39] Ren Fang Chang and Patrick J. Abbott. Factors affecting the reproducibility of the accommodation coefficient of the spinning rotor gauge. *Journal of Vacuum Science & Technology A: Vacuum, Surfaces, and Films*, 25(6):1567–1576, 2007.

[40] G. F. Weston. *Ultrahigh Vacuum Practice*. Butterworth & Co. (Publishers) Ltd., United Kingdom, 1985.

[41] J. F. O'Hanlon. *A user's guide to vacuum technology, 2nd Ed.* John Wiley & Sons, 1989.

[42] D. G. Bills. Causes of nonstability and nonreproducibility in widely used bayard–alpert ionization gauges. *Journal of Vacuum Science & Technology A: Vacuum, Surfaces, and Films*, 12(2):574–579, 1994.

[43] Stanford Research Systems. Bayard-alpert gauge filaments: Tungsten or thoria? http://www.thinksrs.com/downloads/PDFs/ApplicationNotes, 2012.

[44] Brooks Automation. Granville-phillips series 370 stabil-ion® vacuum measurement controller instruction manual. Internal Publication, 2007.

[45] Brooks Automation. Granville-phillips series 370 stabil-ion® vacuum gauge and controller datasheet. Internal Publication, 2008.

[46] Pfeiffer Vacuum. Prisma plus^{TM} qmg 220 operating instructions. Internal Publication, 2007.

[47] K F Poulter. The calibration of vacuum gauges. *Journal of Physics E: Scientific Instruments*, 10(2):112, 1977.

[48] D. Li, G. Zhao, M. Guo, J. Xu, and Y. Cheng. Static expansion vacuum standard with extended low pressure range. Mapan, **24**, 95-100, 2009.

[49] Detian Li, Meiru Guo, Yongjun Cheng, Yan Feng, and Dixin Zhang. Vacuum-calibration apparatus with pressure down to 10^{-10} pa. *Journal of Vacuum Science & Technology A: Vacuum, Surfaces, and Films*, 28(5):1099–1104, 2010.

[50] B. W. Rossiter and R. C. Baetzold. *Physical Methods of Chemistry, Second Edition, Volume Six: Determination of Thermodynamic Properties*. John Wiley & Sons Inc., 1992.

[51] H. M. Akram, M. Maqsood, and H. Rashid. Techniques used for vacuum standardization. World Applied Sciences Journal 7(1): 76-85, 2009.

[52] Li Detian, Cheng Yongjun, and Feng Yan. Extension of the range of a constant-conductance flowmeter by a flow divider. *Measurement Science and Technology*, 22(12):125405, 2011.

[53] K. E. McCulloh, C. R. Tilford, C. D. Ehrlich, and F. G. Long. Low-range flowmeters for use with vacuum and leak standards. *Journal of Vacuum Science & Technology A: Vacuum, Surfaces, and Films*, 5(3):376–381, 1987.

[54] James A. Fedchak and Dana R. Defibaugh. Accurate conductance measurements of a pinhole orifice using a constant-pressure flowmeter. *Measurement*, 45(10):2449 – 2451, 2012. ¡ce:title¿Special Volume¡/ce:title¿.

[55] Agilent. Sh-100 dry scroll vacuum pump. Manual (Revision A, 2005).

[56] H. Pang I. Moult, W. Wang. Design of a magneto-optical trapping system. APSC 459 final report, 2010.

[57] H. J. Lewandowski, D. M. Harber, D. L. Whitaker, and E. A. Cornell. Simplified system for creating a bose-einstein condensate. Internal Publication, 2003.

[58] D. A. Steck. Rubidium 85 d line data. Internal Publication, 2001.

[59] T. Zickler. Basic design and engineering of normal-conducting, iron-dominated electromagnets. Internal Publication at CERN, 2009.

[60] Magnus Haw, Nathan Evetts, Will Gunton, Janelle Van Dongen, James L. Booth, and Kirk W. Madison. Magneto-optical trap loading rate dependence on trap depth and vapor density. *J. Opt. Soc. Am. B*, 29(3):475–483, Mar 2012.

[61] C. Monroe, W. Swann, H. Robinson, and C. Wieman. Very cold trapped atoms in a vapor cell. *Phys. Rev. Lett.*, 65:1571–1574, Sep 1990.

[62] F. Reif. *Fundamentals of Statistical and Thermal Physics*. McGraw-Hill, New York, 1965.

Appendix A

Loading rate investigation

A.1 Reif model

This appendix describes an investigation of the loading rate of a vapour loaded MOT performed in our lab by Magnus Haw, Nathan Evetts and Dr. James Booth described in [60]. It is included because many of the measurement techniques used in this investigation are described in detail in this thesis. The trap loading rate, R, for a magneto-optical trap loaded from a vapour can be modeled by what we call the 'Reif model' [61, 62]. The Reif model states that any atom entering the trap volume with speed less than the 'capture velocity', v_c, will be cooled and trapped. This model leads to a prediction of loading rate as

$$R = \frac{2Av_c^4 n}{\pi^2 v_{\mathrm{th}}^3} \tag{A.1}$$

where $v_{\mathrm{th}} = \sqrt{\frac{8k_B T}{\pi m}}$ is the mean thermal velocity of the background particles, A is the surface area of the trap region, and n is the background density of the species being trapped. The trapping volume is taken as the region of intersection of the laser beams forming the MOT.

The depth of a trap can be written as $U = \frac{1}{2}mv_e^2$, where v_{e} is the escape velocity. We make the assumption that the capture velocity is proportional to the escape velocity, $v_{\mathrm{c}} = bv_{\mathrm{e}}$. This allows us to write the loading rate, R, as

$$R = \left(\frac{8b^4 A}{\pi^2 m^2 v_{\mathrm{th}}^3}\right) U^2 n. \tag{A.2}$$

This model had never been tested experimentally and has several attractive features such as relating the loading rate to difficult to find parameters such as n, and U. There were four main goals of this work. The first and second were to test that the loading rate, R, is proportional to n and to U^2 as predicted in Eq. A.2. The third goal involves a determination of trap depth for different settings of MOT pump detuning and intensity based on knowledge of the trap depth for one particular pump detuning and intensity

setting. The fourth goal of this work was to estimate the proportionality constant, b, between the escape and capture velocity.

A.2 Experimental observables

As seen previously in section 3.2.1, a portion of the photons being emitted by the atoms in a MOT can be collected onto a photodetector. The voltage output by the photodetector, $V(t)$, will be proportional to the number of atoms in the trap, $N(t)$. Specifically,

$$V(t) = \alpha\gamma_{\mathrm{sc}}N(t). \tag{A.3}$$

γ_{sc} is the rate at which an atom scatters photons and depends on the detuning and the intensity of the light. α is the proportionality constant between the number of photons emitted per second by the trapped atoms and the photodiode voltage produced, and can be expressed as $\alpha = \frac{hc}{\lambda}(\frac{r^2}{4d^2})\epsilon\eta$. The factor η is the optical power to voltage conversion factor of the photodiode. ϵ describes the transmission of the glass and lens which the photons travel through to arrive at the photodetector. r is the radius of the lens that focuses the fluorescent light onto the photodetector. d is the distance from the trapped atoms to the lens. The ratio $(\frac{r^2}{4d^2})$ involving r and d accounts for the solid angle of photons that are collected onto the detector.

The loading rate equation of a MOT is usually modelled as (see Eq. 1.1 in section 1.3)

$$\frac{dN}{dt} = R - \Gamma N - \beta \int n^2(\vec{r}, t)\, d^3\vec{r}. \tag{A.4}$$

This work focuses on the loading rate of the MOT, R. For short times from initial loading the number of atoms trapped is very small so that one can approximate

$$\frac{dN}{dt}|_0 = R. \tag{A.5}$$

In terms of photodetector voltage Eq. A.5 becomes

$$\frac{dV}{dt}|_0 = \dot{V}_0 = \alpha\gamma_{\mathrm{sc}}R \tag{A.6}$$

where $\dot{V}_0$ is the rate of change of V for small times after the initial turn on of the MOT. $\dot{V}_0$ is proportional to R which changes with different MOT settings, such as different pump light detunings and intensities, different geometries (e.g. beam sizes), and background gas density.

To eliminate uncertainties in the quantities α and $\gamma_{\rm sc}$, we define a new experimental parameter

$$M_i = \left(\frac{V_{\rm std}}{V_i}\right)\dot{V}_0^i \tag{A.7}$$

where V_i is the steady state voltage when the MOT is fully loaded with settings i. $V_{\rm std}$ is taken by switching quickly from MOT setting i to some pre-selected 'standard' setting. The voltage immediately after the switch, $V_{\rm std}$, is recorded before the atom number has had time to change. $\dot{V}_0^i$ is the voltage rise after initial turn on for MOT setting i. Using the fact that the atom number is the same for V_i and $V_{\rm std}$, Eq. A.3 gives

$$\frac{V_{\rm std}}{V_i} = \frac{\gamma_{\rm sc}^{\rm std}}{\gamma_{\rm sc}^i}. \tag{A.8}$$

Substitution of Eq. A.8 and Eq. A.6 into Eq. A.7 gives

$$M_i = \left(\frac{V_{\rm std}}{V_i}\right)\dot{V}_0^i = \frac{\gamma_{\rm sc}^{\rm std}}{\gamma_{\rm sc}^i}\left(\alpha\gamma_{\rm sc}^i R_i\right) = \alpha\gamma_{\rm sc}^{\rm std}R_i \tag{A.9}$$

so that $M_i \propto R_i$ with the same proportionality constant for different MOT settings i.

The MOT apparatus used was the same one described in section 3.1. ^{85}Rb was used as the trapped species. The total standard six beam pump power was 18.3 mW and 0.56 mW for the repump. The beams had a $1/e^2$ horizontal (vertical) diameter of 7.4 (8.4) mm. This corresponds to a pump intensity of 37.5 mW cm^{-2}. The MOT was operated with an axial gradient of 27.9(0.3) G cm^{-1}. This maximum pump intensity and a 12 MHz pump detuning was used as the standard MOT setting.

A.3 The dependence of loading rate on MOT trap depth

To determine if the loading rate, R, is proportional to U^2 measurements of M_i were taken for various MOT settings, i. U_i were measured independently for the various MOT settings via the catalysis method described in section 3.3. The results, shown in Fig. A.1, support a linear relationship between $M_i \propto R_i$ and U_i^2. Table A.1 gives the measured values of trap depth for various MOT pump detunings and intensities.

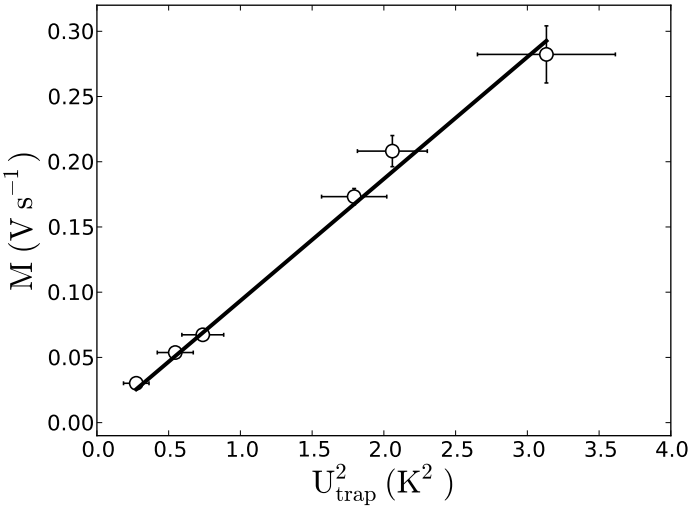

Figure A.1: Evidence that the loading rate of a MOT is proportional to the square of trap depth. The quantity M_i for different MOT settings i is proportional to the loading rate R_i. Plotting M_i versus the trap depth of each MOT setting U_i^2 indicates a linear relationship.

A.4 Trap depth determination using loading rates

It is proposed that the trap depth for different settings of MOT pump detuning and intensity can be determined based on knowledge of the trap depth for one particular pump detuning and intensity setting. The approach for this goal makes several assumptions. The surface area of the trap region is assumed to stay the same for different MOT pump detuning and intensity settings. It is also assumed that the proportionality constant, b, between v_c and v_e stays the same for different settings. Finally it is assumed that the background density, n, also is a constant. With these assumptions the ratio of Eq. A.2 for two different MOT settings gives

$$U_2 = U_1\sqrt{\frac{R_2}{R_1}}. \tag{A.10}$$

To determine the trap depth of MOT setting 2, a measurement of the ratio of loading rates for setting 2 and another setting 1 is needed. The additional

Table A.1: MOT trap depths measured using the 'catalysis method' for various MOT settings

Pump Detuning (MHz)	Pump Intensity (mW cm^{-2})	U (K)
-5	2.9	0.52 (0.12)
-8	2.9	0.74 (0.12)
-10	2.9	0.86 (0.12)
-12	7.5	1.34 (0.12)
-12	10.4	1.44 (0.12)
-12	37.5	1.77 (0.19)

knowledge of the trap depth for setting 1 provides the trap depth, U_2.

Using measurements of M_1 and M_2 for two MOT settings and a catalysis measurement of trap depth for setting 1 we can find the trap depth for MOT setting 2 using

$$U_2 = U_1\sqrt{\frac{R_2}{R_1}} = U_1\sqrt{\frac{M_2}{M_1}}. \tag{A.11}$$

Fig A.2 shows agreement between the predicted trap depth, U_{pred}, determined from Eq. A.11 and the measured trap depth, U_{meas}, from the catalysis method.

Note that one should not extrapolate this trap depth determination for a MOT too far from the known trap depth.

A.5 The dependence of loading rate on rubidium density

To show that R_i is proportional to n_{Rb} we show $M_i \propto n_{\mathrm{Rb}}$. To do this we measure the loss rate constant, Γ_{MT}, due to background collisions between the background gas and the trapped Rb atoms in a magnetic trap. As described previously in chapter 2, Γ_{MT} can be expressed as

$$\Gamma_{\mathrm{MT}} = \sum_j n_j \langle \sigma v_j \rangle_{Rb,j} \tag{A.12}$$

where n_j is the density of background species j. The term $\langle \sigma v_j \rangle_{Rb,j}$ is the velocity averaged loss collision cross section between the trapped Rb and background species j. Isolating the dependence of Γ_{MT} on the background density of Rb, n_{Rb}, we have

$$\Gamma_{\mathrm{MT}} = n_{\mathrm{Rb}} \langle \sigma v_{\mathrm{Rb}} \rangle_{\mathrm{Rb,Rb}} + \Gamma_a \tag{A.13}$$

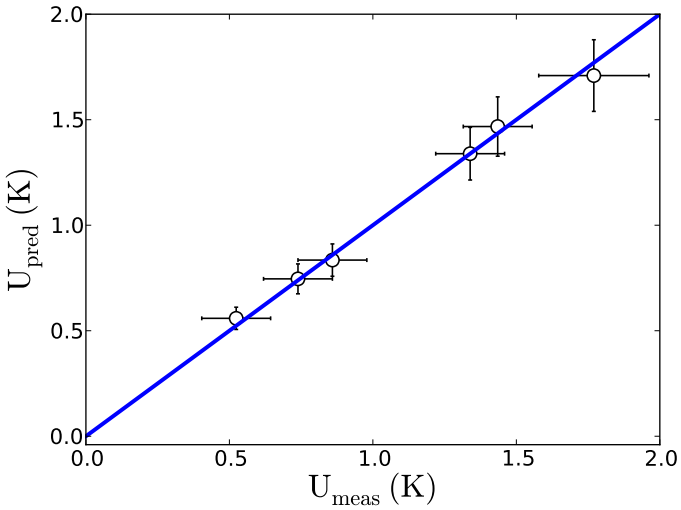

Figure A.2: MOT trap depth is predicted based on the ratio of loading rates and the knowledge of a comparison trap depth. The predicted trap depth for various MOT settings is plotted versus the measured trap depths showing good agreement between the two.

where Γ_a is the contribution to Γ_{MT} due to background species other than Rb.

From Eq. A.2 and Eq. A.9 our model states $M_i = k_i n_{\mathrm{Rb}}$ where k_i is a proportionality constant. Rearranged slightly we have $n_{\mathrm{Rb}} = \frac{M_i}{k_i}$ and inserting this into Eq. A.13 gives

$$\Gamma_{\mathrm{MT}} = \frac{M_i}{k_i}\langle\sigma v_{\mathrm{Rb}}\rangle_{\mathrm{Rb,Rb}} + \Gamma_a. \tag{A.14}$$

Measurements of Γ_{MT} in a magnetic trap and M_i for one particular MOT setting, i, at various Rb densities should give a linear relationship for Γ versus M_i. The MOT setting, i, chosen was the standard setting. The Rb density was varied by filling the MOT region by running current through a Rb dispenser and then letting the density decay over time. Γ_{MT} was measured as described in section 3.2.2. M_{std} for the standard MOT setting was also measured at the same time. Fig. A.3 shows the results and verifies that $M_{\mathrm{std}} \propto n_{\mathrm{Rb}}$ so that $R_{\mathrm{std}} \propto n_{\mathrm{Rb}}$.

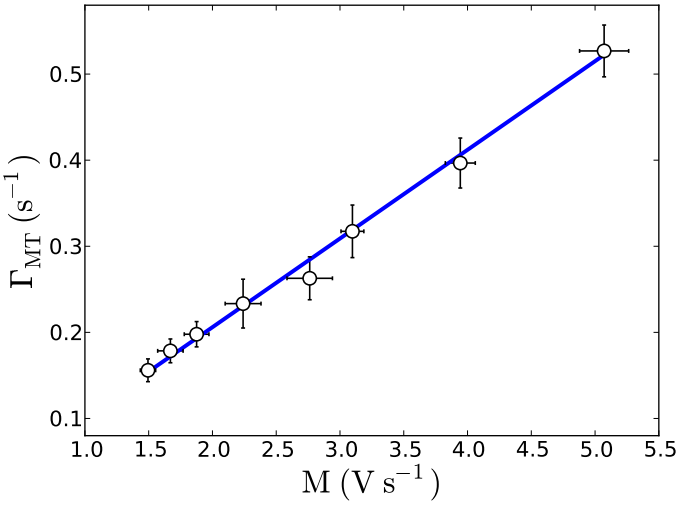

Figure A.3: Evidence that the loading rate of a vapour loaded Rb MOT is proportional to the background density of Rb, n_{Rb}. The loss rate constant of a magnetic trap, Γ_{MT}, varies linearly with Rb background density. If the measure M, which is proportional to the loading rate of a MOT, is also proportional to the Rb background density then Γ_{MT} will vary linearly with M. For this measurement the 'standard' setting of the MOT was used for M.

A.6 Determination of b

The last part of this investigation is to determine the proportionality constant b. Using Eq. A.2 and Eq. A.9 and dividing by the background rubidium density, n_{Rb}, we have

$$\frac{M_i}{n_{\mathrm{Rb}}} = \alpha\gamma_{\mathrm{sc}}^{\mathrm{std}}\frac{R_i}{n_{\mathrm{Rb}}} = \alpha\gamma_{\mathrm{sc}}^{\mathrm{std}}\left(\frac{8b^4A}{\pi^2m^2v_{\mathrm{th}^3}}\right)U_i^2. \tag{A.15}$$

This equation predicts that $\frac{M_i}{n_{\mathrm{Rb}}}$ should be linearly related to U_i^2 with a slope from which b can be extracted.

To obtain $\frac{M_i}{n_{\mathrm{Rb}}}$ for different settings i, M_i was measured as the density of rubidium changed. The MOT region was filled with Rb vapour. As the density of Rb was slowly decreasing from initial filling, Γ_{MT} for a magnetic trap

was measured. $M_{\rm std}$ and M_i was also measured for various MOT settings as the density of Rb changed.

To determine the Rb densities, a plot of $\Gamma_{\rm MT}$ versus $M_{\rm std}$ was used. The slope is $\frac{\langle\sigma v_{\rm Rb}\rangle_{\rm Rb,Rb}}{k_{\rm std}}$ where $M_{\rm std} = k_{\rm std} n_{\rm Rb}$. If $\langle\sigma v_{\rm Rb}\rangle_{\rm Rb,Rb}$ is calculated, as described in chapter 2, then $k_{\rm std}$ can be determined and measurement of $M_{\rm std}$ provides the density of rubidium. $M_{\rm std}$ as a function of time as the Rb density decreased was fit so that $n_{\rm Rb}$ could be determined when each M_i measurement was made.

Fig. A.4 shows a plot of M_i vs $n_{\rm Rb}$. The slopes of these plots are $E_i = \frac{M_i}{n_{\rm Rb}}$ which can be plotted versus U_i^2 as shown in Fig. A.5. The slope of the plot in Fig. A.5 allows b to be estimated from Eq. A.15.

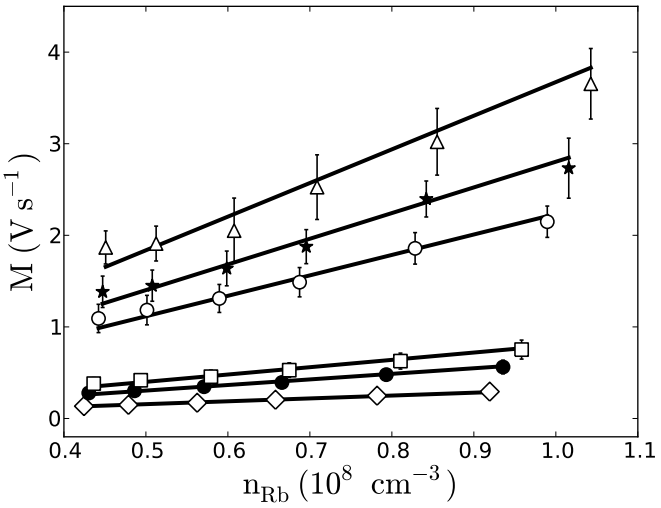

Figure A.4: Measurement of M_i for various MOT settings, i, versus the density of background gas, $n_{\rm Rb}$. The slopes should be linearly related to the trap depth squared for the different MOT settings. The density of Rb was determined by measurement of the loss rate constant of a magnetic trap, measurement of $M_{\rm std}$, and calculation of the velocity averaged loss collision cross section, $\langle\sigma v_{\rm Rb}\rangle_{\rm Rb,Rb}$.

To determine b the values of α and $\gamma_{\rm sc}^{\rm std}$ are determined as described in section 6.2. The value of A was estimated as the surface area of the intersection of three perpendicular cylinders, $A = 3(16 - 8\sqrt{2})r^2$, where r is

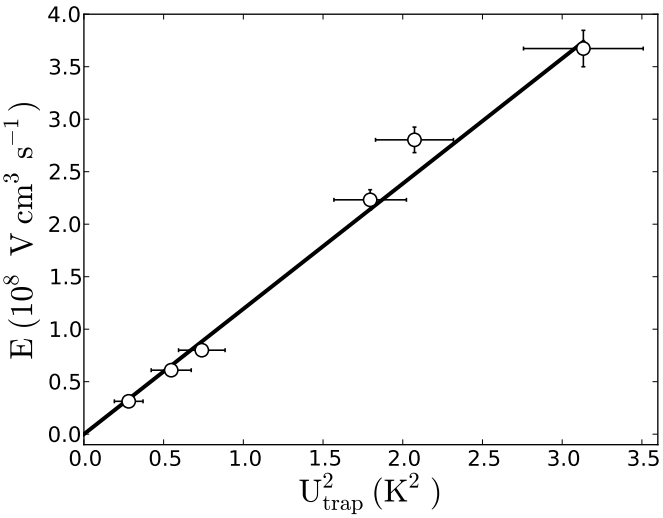

Figure A.5: A plot of $\frac{M_i}{n_{\mathrm{Rb}}}$ versus U_i^2. The proportionality constant, b, between the capture and escape velocity can be extracted from the slope with the estimation of various coefficients.

the laser beam radius averaged across the horizontal and vertical directions. The factor $\frac{8}{\pi^2 m^2 v_{\mathrm{th}}^3}$ was computed for ^{85}Rb vapour of temperature $T = 300$ K. Table A.2 gives the calculated values for all these quantities. From the quantities given in Table A.2 the proportionality constant b was determined. The relationship between the capture velocity, v_c, and the escape velocity, v_e, was found to be

$$v_c = 1.29(0.12)v_e. \tag{A.16}$$

Table A.2: Parameters used in calculation of b, the proportionality constant between the capture velocity v_c and the escape velocity v_e.

Parameter	Value	Uncertainty
A	2.08 cm^2	10 %
$\alpha = \frac{(r_{\mathrm{lens}})^2}{4(d_{\mathrm{MOT}})^2}\eta\frac{hc}{\lambda}\epsilon$	7.84 $\times 10^{-15}$ V s	20 %
$\gamma_{\mathrm{sc}}^{\mathrm{std}} = \frac{\Gamma}{2}\left(\frac{s}{1+2+(\frac{2\delta}{\Gamma})^2}\right)$	$6.8 \times 10^6 \mathrm{s}^{-1}$	20 %
$\frac{8}{\pi^2 m^2 v_{\mathrm{th}}^3}$	$3.85 \times 10^{-2} \frac{\mathrm{cm}}{\mathrm{K}^2\mathrm{s}}$	5 %